Doctoral thesis

Doctoral theses at NTNU, 2023:435

Chandrahaasan Kattuputhur Soundararajan

Hydrogen-induced degradation behavior of nickel alloy 625, studied using multiscale in-situ experiments

NTNU
Norwegian University of Science and Technology
Thesis for the Degree of
Philosophiae Doctor
Faculty of Engineering
Department of Mechanical and Industrial
Engineering

NTNU
Norwegian University of
Science and Technology

Chandrahaasan Kattuputhur Soundararajan

Hydrogen-induced degradation behavior of nickel alloy 625, studied using multiscale in-situ experiments

Thesis for the Degree of Philosophiae Doctor

Trondheim, December 2023

Norwegian University of Science and Technology
Faculty of Engineering
Department of Mechanical and Industrial Engineering

NTNU
Norwegian University of
Science and Technology

NTNU
Norwegian University of Science and Technology

Thesis for the Degree of Philosophiae Doctor

Faculty of Engineering
Department of Mechanical and Industrial Engineering

© Chandrahaasan Kattuputhur Soundararajan

ISBN 978-82-326-7572-2 (printed ver.)
ISBN 978-82-326-7571-5 (electronic ver.)
ISSN 1503-8181 (printed ver.)
ISSN 2703-8084 (online ver.)

Doctoral theses at NTNU, 2023:435

Printed by NTNU Grafisk senter

Preface

This doctoral work is submitted to the Norwegian University of Science and Technology (NTNU) for partial fulfillment of requirements for the Doctor of Philosophy degree (PhD). The work was done between January 2020 to April 2023 under the supervision of Professor Alexei Vinogradov. The main experimental work was carried out in the Nanomechanical lab, Metallography lab and Corrosion lab at the Department of Mechanical and Industrial Engineering, and at NTNU XRD-lab.

The doctoral work was financially sponsored through the project "M-HEAT - Multi-scale hydrogen embrittlement assessment tool for components at subsea (294689)", a joint research project between NTNU, the Research Council Norway and several industrial partners.

Chandrahaasan Kattuputhur Soundararajan
Trondheim, August 2023

Acknowledgment

Firstly, I would like to express my gratitude to Prof. Alexey Vinogradov for accepting me to work in his group and for providing valuable ideas, suggestions, and support throughout. Thank you!

Secondly, I extend my thanks to Prof. Roy Johnson for his valuable support at the inception and end stages of this PhD journey. I would also like to express my appreciation to the colleagues of the M-HEAT project for their insightful discussions and comments during our project meetings.

I appreciate the help of Dr. Christian Rodriguez for teaching me all the techniques in the lab. My thanks go to Iman Taji and Shabnam Karimi for their assistance at the start of my PhD. I also wish to acknowledge the "Hydrogen couple", Dr. Xu Lu and Dr. Dong Wang, for their genuine interest in my research, their valuable insights, and consistent feedback. I would also like to acknowledge the contribution of Alexander Sendrowicz and Alexander Myhre in conducting the Acoustic Emission experiments, as well as their patience in addressing my inquiries.

A special note of gratitude goes to Erik H Koren for his persistent reminder of "STAFETT ER STAFETT," and for consistently offering assistance both on and off the job whenever needed. Thanks to all those enlightening yet irrelevant conversations, that kept me going until the end. I also extend my thanks to Christopher Fjeldstad, who has not only been a great office mate but also a wonderful friend.

To my friends and family back home, I am grateful for your encouragement. In particular, I want to express my sincere appreciation to Dr. Mama and Usha Attha for supporting my early education. In a similar vein, I value the support of Balu Mama and Poongodi Chithi. To my parents, Revathi & Soundararajan and my sister, thank you for being supportive of my decisions and serving as huge inspirations on my journey. Finally, to my wife, thanks for being patient and understanding. Let us raise a toast to new beginnings!

Abstract

Nickel-based alloys are widely used in the oil and gas industries as safety critical components owing to its high strength and corrosion resistance properties. However, they are susceptible to hydrogen embrittlement (HE), a phenomenon that weakens metallic materials, leading to unexpected and catastrophic failures. The interaction between hydrogen and material defects plays a crucial role in this degradation process. This study investigates the effect of hydrogen on the plastic behavior of nickel-based alloy, Alloy 625, at different length scales to gain insights into this interactions. The study utilized in-situ Acoustic emission (AE) monitoring during tensile tests to observe hydrogen influence on macroscale deformation and fracture behavior in real-time. In-situ electrochemical nanoindentation (ECNI) was used to probe local mechanical properties at the nanoscale.

The tensile test revealed progressive reduction in fracture elongation and increased strength response with increase in hydrogen concentration. The AE signals from tensile tests were characterized using spectral analysis based non-supervised clustering procedure to separate the contribution of dislocation slip and microcracks into the deformation and fracture processes. The results reveal that the relative mobile dislocation density increases with increasing hydrogen concentration, as hydrogen reduces the critical stress for Frank Reed source activation and loop expansion. Additionally, hydrogen-charged samples show a reduction in average dislocation velocity, indicating hydrogen solute pinning the dislocations results in hardening behavior. The study also unveils the conditions and details of the kinetics of the hydrogen-assisted crack nucleation and propagation process in hydrogen-charged samples. Postmortem characterization of crack propagation path reveals a transition from the transgranular to the intergranular type, which is attributed to the hydrogen concentration profile depending on the loading conditions.

To understand the hydrogen effect on the nanomechanical response of the annealed nickel alloy, nanoindentation tests with in-situ charging and in-situ scanning probe microscopy (SPM) imaging was carried out. The results show reduced pop-in load, indicative of hydrogen-enhanced dislocation nucleation, resulting from reduction in dislocation line energy or stacking fault energy. The study estimated the hydrogen contribution to the lattice frictional stress using the Nix-Gao model and found that the hydrogen-induced frictional stress had a linear dependence with solute concentration, implying the solute drag effect. The study also reveal hydrogen-induced surface slip line formation during severe charging; the hardness measured after subsequent desorption exhibit softening behavior, which is attributed to non-equilibrium vacancies generated during charging and the subsequent stabilization by hydrogen.

Finally, the study examines the effect of hydrogen on pre-strained nickel alloy using

ECNI technique. The results show hydrogen-induced hardening during charging and softening behavior during desorption. The hardening is due to the collective influence of pre-existing defects and hydrogen solutes impeding the dislocation motion. Moreover, the enhanced hydrogen uptake reduces the SFE locally at the surface and promotes mechanical twinning, resulting in increased hardness. On the other hand, the pre-strained samples exhibit softening behavior during desorption, which is attributed to irreversible microstructural changes caused by hydrogen-enhanced vacancies. This study highlights the permanent modification of the microstructure by hydrogen solute, which could lead to autocatalytic defect generation and ultimately failure.

Contents

Preface **iii**

Acknowledgment **v**

Abstract **vii**

List of Figures **xi**

List of Tables **xiii**

List of Abbreviations **xv**

Part I **1**

1 Introduction **3**

2 An overview on hydrogen embrittlement **7**
- 2.1 Hydrogen source, diffusion and trapping . . . 7
- 2.2 Damage mechanisms . . . 9
- 2.3 HE investigations in Ni-based alloys . . . 10

3 Methods and material **13**
- 3.1 Material and sample preparation . . . 13
- 3.2 Acoustic emission . . . 14
  - 3.2.1 Fundamentals . . . 14
  - 3.2.2 Relevance to material science . . . 14
  - 3.2.3 AE signal processing . . . 16
- 3.3 Nanoindentation . . . 19
  - 3.3.1 Contact mechanics . . . 19
  - 3.3.2 Nanomechanical properties . . . 21
  - 3.3.3 In-situ electrochemical indentation . . . 22

4 Summary and further work **25**
- 4.1 Summary of papers . . . 25
- 4.2 Conclusion . . . 28
- 4.3 Further Work . . . 29

Bibliography **31**

Part II 37

Article I 39

Article II 59

Article III 71

List of Figures

2.1 Hydrogen-induced intergranular cracking in Inconel 718 (taken from [48]). 11
2.2 Hydrogen assisted slip band formation in 316L austenitic stainless steel (taken from [57]). 12

3.1 Sample geometry used in this work (all dimensions shown are in mm). (a) for tensile test. (b) for Nanoindentation test. 13
3.2 Parameters for AE signal processing. 17
3.3 (a) Typical load-displacement data during nanoindentation. (b) indent in contact with the sample. (c) projected contact area of the Berkovich tip. (taken from [82]). 19
3.4 (a) Schematics of Nanoindentation setup. (b) Load function used in this work. 23

4.1 Graphical abstract for Article I. (a) The kinetics of individual source evolution represented by the cumulative AE power synchronized with the true stress-strain data. The inset in (a) shows the IPF map of H-charged sample from interrupted tensile test marked as EBSD. (b) Estimation of mobile dislocation density from the slope of AE power and reduced strain hardening rate plot for differently H-charged samples. 26
4.2 Graphical abstract for Article II. Hydrogen concentration-dependent nanomechanical properties of nickel alloy 625. Note that a linear relationship for glide resistance stress and frictional stress with hydrogen concentration (highlighted by dashed lines) suggests H-induced hardening. The homogenous dislocation nucleation (HDN) stress reduces with hydrogen content implying H-facilitated dislocation nucleation. . 27
4.3 Graphical abstract for Article III. (a) Hardness data for differently pre-strained samples subjected to similar H-charging desorption cycle. The inset in (a) shows the TEM micrograph of indent performed in hydrogen. The red dashed lines highlight the deformation twins. (b) Summary of results from elastoplastic modelling. 28

List of Tables

3.1 The nominal composition of Alloy 625 as provided by the supplier. . . 13

List of Abbreviations

AE	Acoustic emission
AIDE	Adsorption-induced dislocation emission
ASKC	Adaptive Sequential K-means Clustering
BCC	Body-centered cubic
DFT	Discrete Fourier Transform
EBSD	Electron backscatter diffraction
ECCI	Electron channeling contrast imaging
ECNI	Electrochemical nanoindentation
FCC	Face-centered cubic
FFT	Fast Fourier Transform
FT	Fourier Transform
GBs	Grain boundaries
HAGB	High-angle grain boundary
HE	Hydrogen embrittlement
HEDE	Hydrogen-enhanced decohesion
HELP	Hydrogen-enhanced localized plasticity
HESIV	Hydrogen-enhanced strain-induced vacancy formation
IG	Intergranular
KL	Kulback-Leibler
LAGB	Low-angle grain boundary
LD	Load-displacement curves
NDT	Non-destructive testing
Ni	Nickel
NI	Nanoindentation
PLC	Portevin–Le Chatelier
PSD	Power Spectral Density
SEM	Scanning electron microscopy
SFE	Stacking fault energy
SPM	Scanning probe microscopy
SSRT	Slow strain rate tensile test
TB	Twin boundary
TDS	Thermal desorption spectroscopy
TEM	Transmission electron microscopy
TG	Transgranular
XRD	X-ray diffraction

Part I

Chapter 1

Introduction

Background and motivation

Materials used in subsea application have to with stand harsh environment; where nickel-based alloys are commonly used because of their excellent corrosion resistance and mechanical properties. Subsea components are usually protected from aqueous corrosion by cathodic polarization technique [1], which inadvertently generates hydrogen on the surface. The continuous absorption of hydrogen atoms can lead to a change in the fracture mode of these materials, from ductile transgranular to brittle intergranular. This phenomenon is known as hydrogen embrittlement (HE) and can significantly reduce the lifetime of the component. Although the fracture mechanism of ductile materials is well understood, the mechanisms behind the hydrogen-induced ductile-to-brittle transition are still widely debated. Several theories have been proposed to explain this transition [2–6], yet no consensus has been reached.

The HE is a multifaceted problem, and it is heavily influenced by the microstructure, environmental, and mechanical aspects. For instance, the microstructure plays a critical role. Unique attention has been given to chemistry, microstructure and heat treatment while selecting appropriate materials for subsea. Despite meeting the stringent requirement set by standards, several service failures have been reported [1, 7]. For example, the failure of alloy 725 seal used in subsea equipment has been attributed to the formation of a brittle phase in grain boundaries [8]. Similar failure are reported in Alloy 718, 716 and 625 [9, 10].

The current industrial approach for assessing a material's susceptibility to hydrogen involves conducting macroscale tensile testing on electrochemically pre-charged samples. However, this method only provides binary results - pass or fail - without fully revealing the underlying damage mechanisms. While this methodology accelerates the material screening process, it falls short in revealing the intricate interactions between the hydrogen solute and different microstructural constituents. Additionally, the loss of hydrogen between charging and testing makes it challenging to establish a precise correlation between hydrogen content and the embrittlement phenomena, which is crucial for determining the hydrogen degradation threshold.

To enhance the understanding of hydrogen-induced damage, a more comprehensive approach is needed. Therefore, a new method that can discern hydrogen interactions with defects individually and collectively under controlled conditions is required. By utilizing advanced techniques such as nanoindentation, scanning electron microscopy (SEM), transmission electron microscopy (TEM), in-situ observations during small-scale tensile test, the intricate behavior of hydrogen with the microstructure of the material can be captured on different scales and the underlying damage mechanisms can be better understood.

Objectives

The main objective of this thesis is to gain a comprehensive understanding of the mechanisms related to hydrogen-assisted degradation in nickel-based alloy, Alloy 625. To realize this, experiments were performed at different length scales. The hydrogen effect on dislocation kinetics and fracture behavior at the bulk scale was investigated using tensile test instrumented with the Acoustic emission (AE) technique. The in-situ electrochemcial nanoindentation (ECNI) technique was used to reveal the interaction between hydrogen and the microstructure at the nanoscale. Additionally, advanced postmortem characterization techniques such as electron backscattered diffraction (EBSD), electron channeling contrast imaging (ECCI), and transmission kikuchi diffraction (TKD) were utilized during this PhD study to unveil the HE behavior. The following objectives are pursued:

- Achieve a comprehensive understanding of macroscale mechanical degradation of Alloy 625. Investigate the kinetics of damage evolution and analyze the possible mechanisms for intergranular and transgranular cracking. In addition, access the hydrogen effect on the collective dislocation behavior during tensile test.
- Evaluate the hydrogen effect on nanomechanical properties of Alloy 625 using nanoindentation technique, focusing primarily on dislocation nucleation, plastic deformation and microstructure integrity.
- Investigate the hydrogen-induced softening and hardening behavior of pre-strained nickel alloy using in-situ ECNI.
- Correlate the results obtained from different length scales and compare it to existing mechanism and contribute to HE studies.

Outline

The thesis consist of an introductory part and a collections of three paper, two of which are published and one is submitted for peer-review. **Part I** consist of four chapters. **Chapter 1** gives background and objectives of this thesis. **Chapter 2** focuses on the literature review on hydrogen embrittlement in nickel alloys. **Chapter 3** discusses the material and methodology utilized in this work and their theory. **Chapter 4** summarizes the results of the three peer-reviewed articles, provides a concluding remark and a future direction for further research. **Part II** comprises the research articles that are published or in the process of being published in scientific journals.

List of papers and contributions

Three research papers that are either published or under peer-review are included in this thesis. The details of the papers and other contributions are listed below.

Peer-reviewed journal papers:

[1] **CK Soundararajan**, A Myhre, A Sendrowicz, X Lu, A Vinogradov, Hydrogen-induced degradation behavior of nickel alloy studied using acoustic emission technique, Materials Science and Engineering: A, 865, 144635 - Year: 2023.

[2] **CK Soundararajan**, D Wang, A Vinogradov, Effect of hydrogen on nanomechanical properties of Inconel 625 studied using in-situ electrochemical nanoindentation technique, Journal of Alloys and Compounds, 169742 - Year: 2023.

[3] **CK Soundararajan**, X Lu, D Wang, A Vinogradov, Distinct evidence of hydrogen-enhanced defects formation on pre-strained nickel alloy 625 during in-situ electrochemical nanoindentation test - Submitted for peer review.

Statement of author contributions:

Chandrahaasan K. Soundararajan planned and conducted the experimental work, analyzed the data, and prepared the full manuscripts. Aleksander Myhre and Aleksander Sendrowicz helped with the acoustic emission experiments. Xu Lu helped with the electron backscattered diffraction analysis. Dong Wang helped with the in-situ electrochemical nanoindentaion experiments. Alexey Vinogradov contributed with discussion on data analysis and supervision. All the authors contributed to revising of the manuscripts.

Oral presentations in international conferences:

[1] **CK Soundararajan**, A Vinogradov, Hydrogen degradation behavior of Inconel 625 studied using multiscale in-situ experiments, International symposium on hydrogen embrittlement in nickel alloys, Trondheim, Norway, December 5^{th}, 2022.

[2] **CK Soundararajan**, A Myhre, A Sendrowicz, A Vinogradov, Hydrogen degradation behavior of Inconel 625 studied using in situ acoustic emission technique, HydroGhent symposium, Ghent, Belgium, October 10^{th}, 2022.

[3] **CK Soundararajan**, D Wang, A Vinogradov, Effect of hydrogen on nanomechanical properties of Inconel 625 studied using in-situ electrochemical nanoindentation technique, European Conference on Fracture 23, Madeira, Portugal, June 28^{th}, 2022.

Poster in international conference:

[1] **CK Soundararajan**, A Myhre, A Sendrowicz, A Vinogradov, Hydrogen degradation behavior of Inconel 625 investigated by monotonic tensile test equipped with acoustic emission technique, SteelyHydrogen conference 2022, Ghent, Belgium, October 11-13, 2022.

Chapter 2

An overview on hydrogen embrittlement

Hydrogen embrittlement (HE) is a result of complex interplay between material, microstructure, and environment [2, 11–15]. Hydrogen being the smallest atom in the universe makes it hard to detect its presence inside the material, hence, the structure-properties relationship established so far is of phenomenological basis only. The current chapter provides a brief overview of HE phenomena and its relevance to the nickel alloys.

2.1 Hydrogen source, diffusion and trapping

There are several potential sources where hydrogen can enter the metal and trigger embrittlement [15]. For instance during manufacturing process such as welding, casting and heat treatment, hydrogen can be produced from the moisture present. Surface treatment processes such as pickling and electroplating can results in generation of hydrogen at the surface.

In addition to the above suggested sources, hydrogen can enter the material during service. It has been documented that the bearing housing of wind turbine absorb approx. 3 wt.ppm of hydrogen over its life span, where lubricant contaminated with water serves as hydrogen source [16]. Similarly, hydrogen produced during cathodic protection or from a corrosion process, can also be absorbed in to the metals and result in embrittlement, a critical issue in oil and gas industries [1, 7, 8, 10]. The following relations explain the hydrogen uptake as a result of corrosion reaction [17]. During corrosion, oxidation of metal takes place (Eq. 2.1), in parallel either oxygen (Eq. 2.2) or hydrogen (Eq. 2.3) reduction are the main reduction reactions:

$$M \rightarrow M^{n+} + ne^- \tag{2.1}$$

$$\frac{n}{2}O_2 + nH_2O + 2ne^- \rightarrow 2nOH^- \tag{2.2}$$

$$nH^+ + ne^- \rightarrow \frac{n}{2}H_2 \tag{2.3}$$

Cathodic protection is generally employed to prevent the oxidation reaction, thereby the corrosion process. This is done by connecting the metal either to less noble metal (sacrificial anode) or by using impressed current system. The overall objective is to apply the external current such that the entire system is kept lower than the corrosion potential [17]. While this is effective in controlling the corrosion, it inadvertently introduces hydrogen (due to the dominant hydrogen reduction reaction) into the metals as shown in Eq. 2.4.

$$H^+ + M + e^- \rightarrow MH_{ads} \tag{2.4}$$

When hydrogen is adsorbed on the surface, it can either be absorbed into the material or recombine with other hydrogen atom and produce $H_2(g)$ (Eq. 2.3).

The diffusion flux density is defined as number of particles passing though an unit area per unit time. According to Fick's law, the diffusion flux j is expressed as [18]:

$$j = -D\frac{dC}{dx} \tag{2.5}$$

Here, D is diffusion coefficient having unit of m^2s^{-1}, C and x are concentration and distance respectively. The negative sign implies that the flux direction is opposite to the concentration gradient, i.e. from higher to lower concentration. Further, D is expressed as:

$$D = D_0 \exp -\frac{Q}{kT} \tag{2.6}$$

where D_0 is a pre-exponential factor, Q is the activation energy, k is the Boltzmann constant, and T is the temperature. The activation energy Q indicates the elementary process of atomic motion depending on different elements and crystal structures.

The diffusion rate of hydrogen in metals is larger than other interstitials and substitutional elements [19]. Hydrogen tend to reside or move through the material via the vacant sites in the metal lattice. For face-centered cubic metals (FCC), octahedral voids are preferred interstitial site, whereas for body-centered cubic metals (BCC) metals tetrahedral sites are favorable spot [19, 20]. In general sense, the diffusivity of hydrogen tend to be slower in FCC metals when compared to BCC, while the hydrogen intake/solubility is larger for FCC metals.

Traps influence the diffusion behavior. Some examples of trap sites include vacancies, dislocations, precipitates, interfaces between matrix and precipitates, phase boundaries, grain boundaries, voids, microcracks, etc., [19, 21, 22]. Besides, depending on activation energy, these traps can be categorized into reversible (ability of hydrogen atom to jump out/move freely out of the potential valley and become mobile) and irreversible trap (deep potential valley thus hydrogen atom cannot move out of this spot) sites. It has to be emphasized here that there is no cut-off value to distinguish the reversible and irreversible traps as they are intricately connected to microstructure and environmental conditions [19]. The traps effectively lowers the mobility of hydrogen atoms and they enhance the hydrogen uptake, as a result these trapping sites have higher probability of crack initiation during straining. Several advanced models have been developed accounting for trap density, binding energy, etc., starting from seminal work of McNabb and Foster [23]. Oriani further developed this by assuming equilibrium between lattice and trap sites [24]. While considerable progress have been made in hydrogen diffusion modelling field, the role of traps in influencing the HE susceptibility still remains unclear. For example, dislocations are considered reversible trapping sites, which can reduce effective diffusivity. However, during plastic deformation, these dislocation are mobile, act as transport medium for hydrogen. Several experimental studies have shown that dislocations themselves have varied influence under hydrogen atmosphere, i.e, formation of hydrogen cottrell cloud hindering their motion, on the other hand hydrogen is shown to enhance mobility and pack the dislocations closer. This clearly highlights inherent complexity in HE research, thus it is necessary to combine the actual microstructural constituents with hydrogen trapping and diffusion information to thoroughly study the HE mechanisms.

2.2 Damage mechanisms

To design a hydrogen-damage-tolerant material, it is pertinent to understand the underlying degradation mechanisms. Over the years several mechanisms were proposed based on various experimental observations and theoretical findings. The widely accepted ones are discussed briefly in the following section.

Hydrogen enhanced decohesion (HEDE)

The mechanism built on the premise that hydrogen-caused weakening of interatomic forces at the tip of an already existing crack as proposed by Pfeil [25]. HEDE was later expanded by Troiano in 1960 [3], states that the weakening of interatomic bond by hydrogen is due to the electron transfer from 1s orbital of hydrogen to unfilled d-orbitals. The metallic bond strength is reduced during this process and during tensile loading, decohesion (separation of atoms) is preferred over the slip. This theory was subsequently quantitatively developed by Oriani in 1970 [26], McMahon [27], and Gerberich [28]. The HEDE mechanism is generally used to explain the brittle intergranular fracture in metals [24, 27, 28]. Though the density functional theory results for nickel and iron systems support this mechanism [29], no experimental evidence is available until now, due to limitations associated with characterizing the microstructural features at the atomic scale.

Hydrogen enhanced localized plasticity (HELP)

The HELP mechanism was first proposed by Beachem and coworkers to explain the reduced ductility and plasticity-altered fracture modes at crack tips in embrittled steels [30]. Soon Robertson and coworkers performed the in-situ Transmission Electron Microscopy (TEM) experiments, wherein, a thin aluminum foil was deformed inside the TEM in the hydrogen atmosphere. They observed that under the hydrogen environment, the dislocation multiplication is enhanced and the distance between the dislocations in the pile-up is reduced [2, 30]. Based on this observation they proposed that hydrogen can facilitate the dislocation activity by shielding stress fields of dislocation from interacting with the elastic obstacles [2, 31, 32]. In addition, hydrogen tends to segregate to the high hydrostatic stress field of dislocations, thereby enhance the plasticity. The segregation is limited to the localized region and the fracture tends to propagate in a specific set of planes [33].

Adsorption induced dislocation emission (AIDE)

AIDE states that the dislocation nucleation and subsequent emission from the crack tip are responsible for embrittlement. The nucleation stage is critical, since the adsorbed hydrogen facilitates instantaneous dislocation core formation and surface steps by breaking atomic bonds locally, with further application of stress, the dislocation starts moving away from the crack tip (emission) [12, 34, 35]. During this process, microvoids are reported to nucleate ahead of the crack tip which keeps the crack tip sharp, therefore the fracture surface appears brittle.

Hydrogen enhanced strain induced vacancy formation (HESIV)

The mechanism states that hydrogen enhances the vacancy creation and clustering during plastic deformation, subsequently promotes void nucleation and crack propagation [4, 14]. The HESIV model shifts the focus of HE from hydrogen itself to the hydrogen-related failure mechanism. Several density functional theory simulations in Ni-based superalloys have reported that hydrogen reduces the activation energy for vacancy formation and migration, furthermore, it tend to segregate to the vacancies, and prevent them from collapsing, experimental results also support this observation [36–39].

Defactant concept

The theory proposed that the segregation of defectants, in this case hydrogen to the defects, such as vacancies, dislocations, and stacking faults, can reduce the defect formation energy and increase their respective concentration [6, 15]. This mechanism is further supported by the in-situ nanoindentation experiments which shows the reduced formation energy of dislocation loops in the presence of hydrogen [11].

2.3 HE investigations in Ni-based alloys

Nickel is a ferromagnetic material with a FCC crystal structure and widely used material in engineering applications. They are used in a wide operating temperature range from -50 ℃ (e.g. arctic environment) to 800 ℃ (e.g. Jet engine turbine blades), making them one of the most versatile engineering materials. The term "superalloys" usually refers to the heat resistant metallic material, which offers good toughness and resistance to oxidation and corrosion. Owing to this characteristic behavior, nickel-based super alloys are preferred material of choice in oil and gas industries [1], as the material is expected to withstand aggressive environment.

Ni-based superalloys are commonly classified into solid solution strengthened (e.g. Inconel 625, 690) and precipitation-hardenable alloys (e.g. Inconel 718, 725) [40]. Various alloying elements with different concentrations are added to the Ni-alloys to improve the material performance, yet these materials are susceptible to the HE.

The first experimental investigation of HE in Ni-based superalloys was reported in 1970 [41], ever since significant research related to the topic has been carried out due to their importance in oil and gas fields.

The mechanisms of embrittlement are shown to be related to hydrogen-dislocation interaction irrespective of changes in chemical composition. For example, the decisive role of the strain rate in HE in Alloy 718 was shown by Fournier et al. [42] and for Alloy 600 by Lecoester et al. [43]. They showed that hydrogen transport by moving dislocations controls the brittleness of both alloys. It is highest at strain rates allowing hydrogen atoms to follow the dislocations during tensile tests and disappears if the strain rate is sufficient for breaking away from hydrogen atmosphere. The dependence of strain rate is consistent with the HELP phenomena. The occurrence of the hydrogen-dislocation interactions is supported by TEM observations of planar slip bands along the (111) atomic planes, in addition, the evidence of nanoscale voids nucleated at slip bands, particularly at the intersection of non-parallel slip bands, and crack propagation along slip bands [44, 45]. In nickel alloys both intergranular and transgranular cracks are reported and following sections provides a brief overview.

Intergranular failure

Hydrogen prefers to segregate to the grain boundaries (GBs) as they are energetically favorable sites and offer faster diffusive path [46, 47]. Segregated hydrogen solute weakens the cohesive bond strength between grains and promote crack initiation and propagation along GBs. An example of IG cracking in age hardened Inconel 718 is shown in Fig. 2.1.

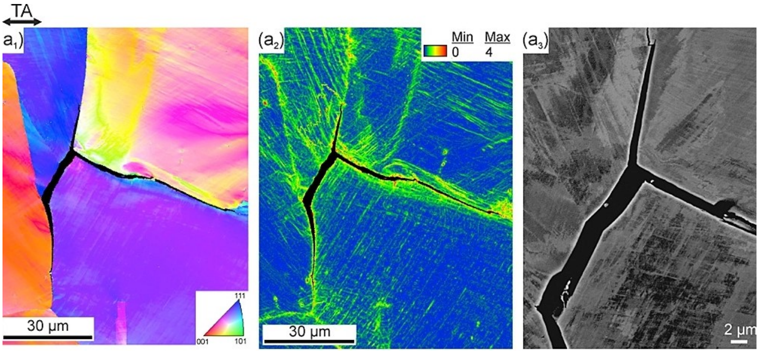

Figure 2.1: Hydrogen-induced intergranular cracking in Inconel 718 (taken from [48]).

Though the HEDE mechanism seems to fit with the observed results, several studies have pointed out the role of critical grain boundary hydrogen concentration (H_c^{GB}) in determining the fracture behavior [21, 49]. The work of Martin et al. on pure Ni have shown that even though the fracture surface of the hydrogen charged material exhibit intergranular behavior, extensive plastic deformation was observed just beneath the IG facets, suggesting hydrogen transport by dislocations to grain boundaries (HELP mechanism) a dominant factor [50]. In contrast, Harris et al. have reported that the intergranular fracture is observed even at 77K, where the interaction between hydrogen and dislocations is basically precluded [51]. These two contrasting studies indicate the knowledge gap in understanding the mechanism and a need for more robust testing methods.

Impurity segregation such as Sulfur and Phosphorus to grain boundaries is also shown to increases the hydrogen uptake thereby promoting decohesion [52]. The role of grain boundary misorientation has also been studied extensively, Low angle GBs ($5° - 15°$) and special GBs ($\Sigma 3 - \Sigma 29$) are reported to show high resistance to GB crack initiation, whereas high angle GBs ($15° - 50°$) are most favorable sites for crack nucleation in Ni alloys [44, 45]. Microstructural heterogeneities at grain boundaries such as δ-phase, carbides are also shown to promote intergranular cracking, but the underlying mechanism remains unclear [48, 50, 53, 54].

Transgranular type

The transgranular fracture in Ni-based superalloys is seldom reported, although not uncommon. The presence of precipitate in Ni-based superalloys promote planar slip or slip localization in a close-packed planes, $\{111\}$, and hydrogen was reported to increase the slip planarity even further due to the solute drag effect [45, 55]. Besides, hydrogen tends to reduce the stacking fault energy thereby decreasing the probability of cross-slip which results in slip bands formation (Fig. 2.2). Preferential segregation of hydrogen at the stress concentrated areas like the crack tip, dislocation slip bands, and at deformation twin boundaries [49, 56], increases the local stress, enhances the vacancy formation thereby increasing microvoids which further develops into transgranular fracture [4, 38].

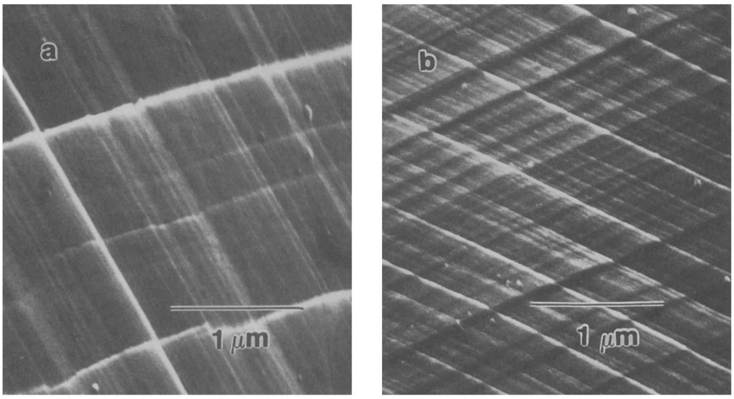

Figure 2.2: Hydrogen assisted slip band formation in 316L austenitic stainless steel (taken from [57]).

Chapter 3

Methods and material

One of the objectives of this doctoral work is to relate the experimental observation at different length scales to explain the embrittlement behavior. Several advanced characterization tools has been utilized, and this chapter discusses the theory behind each of these techniques.

3.1 Material and sample preparation

The material used in this work, Alloy 625, was supplied by Voestalpine GmbH (Austria). The nominal chemical composition as provided by the supplier is shown in Table. 3.1. The alloy was initially hot rolled subsequently annealed at 885 °C for an hour followed by water quenching.

Table 3.1: The nominal composition of Alloy 625 as provided by the supplier.

Element	C	Si	Mn	P	S	Cr	Mo	Ni
wt. %	0.018	0.08	0.07	<0.005	<0.0003	21.31	8.3	62.8
Element	Cu	Co	Ti	Al	Nb	Fe	Ta	
wt. %	0.02	0.18	0.05	0.22	3.25	3.7	<0.02	

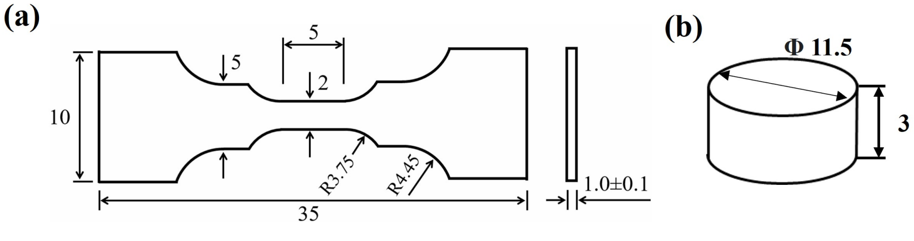

Figure 3.1: Sample geometry used in this work (all dimensions shown are in mm). (a) for tensile test. (b) for Nanoindentation test.

The geometry of the double dog bone shaped tensile sample for slow strain rate tensile tests (SSRT) and the cylindrical sample for nanoindentation experiments are shown in Figure. 3.1. All the samples were ground sequentially from 220 to 4000 grit silicon carbide papers followed by mechanical polishing up to 1 µm diamond paste. Final polishing was done using 200 nm colloidal silica suspension to get deformation-free surface. Details regarding the experimental procedures employed for the individual techniques are discussed comprehensively in the respective articles.

3.2 Acoustic emission

3.2.1 Fundamentals

The acoustic emission (AE) technique belongs to the family of non-destructive testing techniques (NDT), used to monitor the health of structures, has been in practice since 1960s [58]. Unlike other NDT techniques which make use of the "active" source and detection methodology, the AE operates in the "passive" way, i.e, the signals that are identified and characterized are generated by defect evolution under certain load condition [59]. The AE is a naturally occurring phenomena, where transient elastic waves are generated by rapid release of energy during irreversible change in material's structure [60].

The elastic waves propagate through the material in four principal wave modes: longitudinal waves (compression), transversal (shear), surface (Rayleigh waves), and plate waves (Lamb waves) and each of these propagate at different velocities [61]. During acoustic emission testing the wavefront undergoes multiple reflections, interference and mode conversions before reaching the surface and cause surface displacement [62, 63]. The piezoelectric sensor at the surface converts the mechanical displacement into an electrical signal. Once the elastic wave leaves the source and reaches the surface, it has to pass through another medium. Since, air have poor transmitting properties, by using "wave-transparent" coupling medium like either vacuum grease or machine oil the signal transfer can be improved. The strength of the received signals are usually weak, therefore they are usually pre-amplified and processed later.

The AE senors are divided based on their frequency response. The broad-brand sensors has a flat response and can capture all frequencies, ideal for applications where signal source or its evolution is of concern, as it provides more significant information. The resonant type sensors usually operate at narrow range of frequencies, used typically in system with noise is predominant and specific frequency of interest is known. The sensitivity of resonant type senors are superior to their counterpart. However, in the field of material science, broad-band type sensors are widely used, since each source have different characteristic frequency range.

3.2.2 Relevance to material science

To predict the fracture using AE technique, it is pertinent to recognize the essential features of an incoming signal which corresponds to the critical state preceding imminent failure [59]. Thus, a laboratory testing is required to correlate the AE characteristics with the microstructural evolution during loading, to define what the critical state is. The use of acoustic emission for research purpose in the material science have grown over the years and this section presents an overview of only those specific to plasticity and fracture.

It has been well established that the plastic deformation is spatially heterogeneous and temporally intermittent in nature [64]. This is due to discrete character of dislocations, which usually accompanies with local fluctuation in stress-strain. This fluctuation, however, is not reflected upon conventional tensile test, due to the lower resolution of the measuring setup, unless they manifest themselves as a macroscale instabilities such as Lüders bands propagation, Portevin–Le Chatelier (PLC) effect or fracture. The stress-strain data from tensile test is a result of averaged dislocation reactions happening throughout the deforming volume. The AE, however, is capable discriminating the load drop as individual burst of signal. The temporal resolution of AE technique is in microseconds, ideal to study the plastic deformation. The source of AE during plastic deformation include dislocation motion [65–68], twinning [69, 70], phase transformation [71], annihilation, breaking of inclusions, particles and microcrack nucleation and propagation [58, 60, 62, 67, 72].

The collective movement of dislocations (eg. slip, twinning) are considered as the major source, since the passing of dislocation relaxes the surrounding stress field, which releases AE. Heiple and Carpenter have shown from their experiment that it is not possible to discern the motion of single dislocation, even by the transducer with highest resolution ($10^{-14}\ m$) [60]. During tensile test only 1% of energy is released as AE, rest as heat. Thus it is necessary to have thousands of dislocations moving to get a reasonable signal. Another factor to be considered is the strain rate employed during the test; the amplitude of the AE signal is proportional to the dislocation velocity, which further related to applied strain rate using Orowan law:

$$\bar{v} = \frac{\dot{\epsilon}}{\rho_m b} \tag{3.1}$$

where $\bar{v}$ is the average velocity of dislocations, $\dot{\epsilon}$ is the applied strain rate, ρ_m is the mobile dislocation density, b is the burger vector of dislocations. During SSRT, AE is generally very weak and are associated with the continuous signal due to the overlapping events. However, in polycrystalline material, there are grain boundaries, inclusion, point defects, etc. The repeated pinning and de-pinning could release energy in the form of AE as suggest by James and Carpenter [73].

Deformation twinning is another powerful source of AE [74]. The twinning process consists of three stages: nucleation of the twin embryo followed by rapid growth of the embryo, and thickening of the twin in the direction normal to the initial growth direction. While the nucleation and growth of the twin embryo proceed at the velocity of sound in the material, the thickening process is orders of magnitude slower, even under impact conditions. Thus, AE can capture twin nucleation process and not the lateral twin thickening [60].

The AE information related to crack initiation and propagation have been investigated extensively for decades; A common consensus is that the amplitude of the signal is shown to depend on the specific mechanisms [72]. For instance brittle fracture mechanism (intergranular fracture and cleavage/quasi-cleavage fracture) produces higher amplitude signals than ductile ones (micro void coalescence, tearing and shearing). Pollock et. al attempted to explain this behavior by grouping the released energy into three parts: plastic deformation, surface energy and event energy (AE wave) [75]. The plastic deformation term captures the energy expended in creating the plastic zone through dislocation movement and slip; the surface energy refers to the disbonding of atoms to create the new surfaces. For ductile fracture, due to a larger plastic zone and increased surface energy due to a rougher crack surface, less fraction of the elastic energy is released when compared to a brittle fracture of the same magnitude.

3.2.3 AE signal processing

Traditional AE research on material science involves characterizing the burst type signal, wherein preset threshold controls the incoming signal for further processing. The burst type AE signal are widely in use because of its simple equipment setup and post processing methodology. This, however, limits some of the signal associated with dislocation slip as it usually have low energy/amplitude similar to that of the laboratory noise. With the development of advanced acquisition tools and computing resources, continuous signal processing can be realized.

In this work the AE signal processing is done using adaptive sequential K-means clustering (ASKC) algorithm as proposed by Pomponi and Vinogradov [76]. The software employed here returns two critical parameters, median frequency and AE energy, as an output, both representing different properties of spectra [77, 78]. Detailed signal processing procedure employed in the present work has been included in Article I. The following sections, however, provides brief background regarding the tools for the AE signal processing.

For the analysis of AE process in the frequency domain, Fourier Transformation (FT) is employed, more specifically Discrete Fourier Transform (DFT). The FT is well suited for the characterization of periodic or pseudoperiodic signals and is simple to interpret. It is a one-dimensional transformation, and no time information will be available since it assumes stationarity. The digital AE data acquisition results in discrete AE records that are evenly spaced in time. Thus, the AE time series collected depending on the sampling rate results in sampling time interval Δt_s, which defines the maximum resolvable frequency - Nyquist frequency f_N (or cut-off frequency):

$$f_N = \frac{1}{2\Delta t_s} \tag{3.2}$$

An algorithm for efficient calculation of DFT is Fast Fourier Transform (FFT). However, due to the discrete nature of the AE records, so-called leakage effect has to be taken into account in energy (power) calculations.

Welch's method is one way of estimating power spectra (Power Spectral Density - PSD), which was used in this work [79]. While this method is quite reliable over non-stationary noise when compared to full DFT, there is drawback with reduced spectral precision. Welch's method divides the time segment into smaller sub-segments, which might overlap, depending on the particular approach. Tapering is done intentionally to make the window overlapping, to reduce the data loss at the edges of the segment (leakage effect). After that, the periodograms are calculated using FFT, and averaged; this way, non-stationary noise is filtered out of the PSD. The PSD function calculated by Welch's method was further used to calculate AE properties - AE power and median frequency. The PSD of the individual realization $G_k(f)$ has to be noise corrected. The power spectrum of electrical noise $G^{noise}(f)$ has to be determined by recording laboratory/background noise prior to test:

$$G^{noise}(f) = \frac{1}{N} \sum_{i=N}^{N} \sum G_i^{noise}(f) \tag{3.3}$$

Here N denotes the number of realization, at least 30 to 50 noise records have to be calculated and averaged over all of N. This averaged noise spectrum is subtracted from each $G_k(f)$ to get noise corrected estimate of AE data:

$$G(f) = G_k(f) - G^{noise}(f) \tag{3.4}$$

From the noise corrected AE power spectrum, the parameters such as AE energy, E (area under the PSD) and median frequency, f_m can be determined. The normalized PSD is calculated as follows:

$$g(f) = \frac{G(f)}{E} \tag{3.5}$$

It is important to note that each source has distinct power spectra, and this specific property has been made use to distinguish different sources [80].

Parameters during AE signal processing

Figure. 3.2 shows the parameters used to process the AE signals. The significance of each of these parameters on signal processing are discussed below.

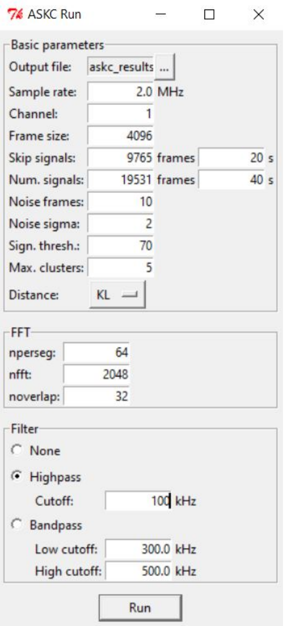

Basic parameters
Output file: askc_results ...
Sample rate: 2.0 MHz
Channel: 1
Frame size: 4096
Skip signals: 9765 frames 20 s
Num. signals: 19531 frames 40 s
Noise frames: 10
Noise sigma: 2
Sign. thresh.: 70
Max. clusters: 5
Distance: KL

FFT
nperseg: 64
nfft: 2048
noverlap: 32

Filter
○ None
● Highpass
Cutoff: 100 kHz
○ Bandpass
Low cutoff: 300.0 kHz
High cutoff: 500.0 kHz

Figure 3.2: Parameters for AE signal processing.

Sample rate - the hardware (analogue-to-digital converter) sample rate set in the data acquisition software should be used in ASKC settings.

Frame size - the AE stream is divided into a set of segments of equal length; Frame size is the number of points per data segment (also commonly termed realization); it is usually set as a power of 2. The frame size can be set either by taking into account of duration of the transient signal, in that case, the PSD calculation is dominated by the properties of particular feature. Another approach is to select a relatively large frame size, so that it represents an average of all the features in the signal. This is particularly useful in continuous signals, where larger frames result in less scatter.

Skip signal - The number of frames to be skipped for signal processing.

Num. signals - Specifies the number of frames to be processed. The frames after this specified number will be automatically skipped by the software.

Noise frames - Before the start of the tensile test, the stationary signal/ laboratory noise is recorded. The number of frames specified here is used to define the noise. The basic assumption is that the noise does not change during the test. If there is noise generated due to test machine, this assumption is not valid and it has to be rectified during cluster analysis. The proposed algorithm [76] is capable of distinguishing such deviations from the regular background noise and the AE events during tensile test.

Noise sigma - a statistical variable to characterize the compactness of the noise cluster and is typically set as 1, 2 or 3. This parameter is mathematically equal to the multiplier to the standard deviation of background noise; the resultant product is then used to define the distance, which serves as an initial measure of similarity/dis-similarity between the clusters [76].

Sign. thresh. - The numerical integer specified here serves as "seed" to define a cluster. In other words, a minimum number of data points required to define a cluster as significant, and further merging of the cluster with other cluster is prohibited. Once the set threshold is reached, this cluster can only evolve by merging the nearest new event.

Max. clusters - While the ASKC does not require this number to be specified, as it automatically determines the number of clusters, it is convenient to set this number by 1 or 2 larger than the the expected number of possible source mechanisms.

Distance - refers to the type of statistical measure of similarity/dis-similarity between the normalized to unity AE PSD functions. In the present study, Kulback-Leibler (KL) divergence in its symmetrical variant is used.

npserseg - This determines the size of the segment used for Welch's method. Large segment size may yield better frequency resolution but compromises on noise filtering.

nfft - The number of points used by the FFT algorithm and should be at least as big as the number of data points.

noverlap - The amount of points by which segments in Welch's method overlap. This setting is dependent on the type of tapering function used, for the present study, a 50% overlap is reasonable.

3.3 Nanoindentation

Nanoindentation (NI) is a powerful tool to probe the properties of the material in extremely small volume (typically in hundreds of nanometers). Initially it was used as hardness measurement tool especially for thin film material. The "instrumented indentation" records the load-displacement quite reliably enabling the estimation of various properties pertaining to the region of interest, which otherwise are difficult to obtain. The force resolution is in the order of µN and for displacement, it is in nm. The scanning probe microscopy (SPM) tool enables studying the material's surface. A sharp probe, which is connected to the sensitive spring system, scans back and forth over the sample surface with a force on the order of µN. Based on the feedback from the tip, a two-dimensional map of the surface is generated. The SPM tool is quite useful in HE studies, since the first-hand information like charging-induced dislocation slip is obtained readily. It also serves as surface quality check tool prior to indentation.

3.3.1 Contact mechanics

The indentation technique is built on the premises of contact mechanics, which describes the force acting on bodies in contact [81]. In Figure. 3.3a, a typical load-displacement (LD) plot is presented. It shows a loading part until maximum load (P_{max}) followed by unloading part. Figure. 3.3b&c shows the contact between the material and the indenter. The displacement corresponds to maximum load is h_{max}, the contact depth h_c and the final displacement is h_r.

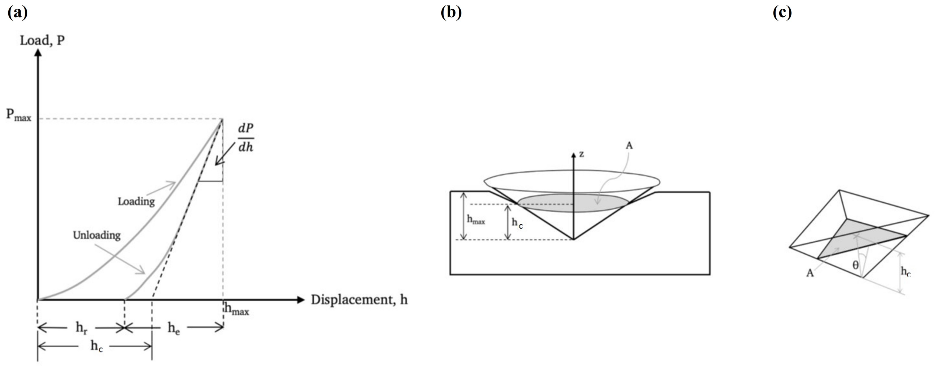

Figure 3.3: (a) Typical load-displacement data during nanoindentation. (b) indent in contact with the sample. (c) projected contact area of the Berkovich tip. (taken from [82]).

The Hertz theory of elasticity can be applied to the initial portion of a point contact loading [83]. He demonstrated that the radius of contact, a, is related to the radius of the indenter R, the load applied P, and the materials' elastic properties E_r in the following manner [81]:

$$a^3 = \frac{3PR}{4E_r} \tag{3.6}$$

The term E_r is the reduced modulus of the material, which relates the modulus of tip E_1 and sample E_2 along with their respective Poisson ratios ν:

$$\frac{1}{E_r} = \frac{1-\nu_1^2}{E_1} + \frac{1-\nu_2^2}{E_2} \tag{3.7}$$

The indenters are generally made of diamond, which has an elastic modulus of $E_1 = 1140$ GPa and a Poisson's ratio of $\nu_1 = 0.07$. According to the Hertz theory, the indentation depth is given by:

$$h = \left(\frac{3}{4E_r}\right)^2 \frac{P^2}{R} \tag{3.8}$$

The applied load can be described as a function of indentation depth as:

$$P = \frac{4}{3} R_r \sqrt{Rh^3} \tag{3.9}$$

Therefore, if the radius of indenter tip is known, the E_r value of the sample can be obtained by fitting the elastic part of the load-displacement curve using Eq. 3.9.

Another methodology to estimate the reduced modulus is proposed by Sneddon. Their model describes the indentation by a rigid conical indenter with an angle of 2θ on an isotropic elastic half-space as a function of the applied force and indentation depth [84]:

$$P = \frac{\pi a_c}{2} E_r a_c \cot\theta \tag{3.10}$$

$$h = \frac{\pi}{2} a_c \cot\theta \tag{3.11}$$

Here a_c is the contact radius defined in Eq. 3.6. By combining Eq. 3.10 & Eq. 3.11, and eliminating a_c, the applied load can be rewritten as a function of depth as:

$$P = \frac{\pi a_c}{2} E_r h^2 \tan\theta \tag{3.12}$$

The contact stiffness S can be calculated as the slope at the beginning of unloading:

$$S = \frac{dP}{dh} = 2E_r \sqrt{\frac{A_c}{\pi}} \tag{3.13}$$

where A_c is the projected contact ares defined as πa_c^2. The reduced modulus can be rewritten as:

$$E_r = \frac{S}{2} \sqrt{\frac{\pi}{A_c}} \tag{3.14}$$

While, the Sneddon model can estimate the reduced modulus from the stiffness, it is only suitable for an indenter with perfect rigid cone shape. Oliver and Pharr, further improved this model to be suited for different shaped indenters [85]. They fitted the upper portion of unloading part of LD curve with a power-law equation. The reduced modules E_r is defined according to the Oliver and Pharr model as:

$$E_r = \frac{S}{2\beta}\sqrt{\frac{\pi}{A_c}} \tag{3.15}$$

Here β is the geometric correction factor, which was proposed as 1.034 for Berkovich indenter.

The projected contact area (A_c) relates the indenter contact depth (h_c) with the indenter area function. The contact depth indicates the vertical distance along the contact. According to Oliver and Pharr [85]:

$$h_c = h_{max} - \epsilon\frac{P_{max}}{S} \tag{3.16}$$

where h_{max} and P_{max} are the maximum indentation depth and maximum applied load respectively. The ϵ is a constant depend on the indenter geometry, for Berkovich indenter it is 0.75. The area function relationship between the contact area A_c and contact depth h_c can be described by sixth-order polynomial equation as:

$$A(h_c) = C_0 h_c^2 + C_1 h_c + C_2 h_c^{1/2} + C_3 h_c^{1/4} + C_4 h_c^{1/8} + C_5 h_c^{1/16} \tag{3.17}$$

where C_0 is 24.5 for Berkovich indenters. C_1 to C_5 are determined by performing a series of indentation with various contact depth on fused quartz, whose reduced modulus and hardness are known. These indentation curves are fitted against Eq. 3.17 to estimate the coefficient values. Finally, with a qualified area function, the reduced modulus can be calculated precisely by using the Oliver-Pharr method as shown in Eq. 3.15.

3.3.2 Nanomechanical properties

Hardness

The hardness is defined as the material's resistance to indentation. The nanohardness is computed by dividing the maximum load P_{max} with the contact area $A(h_c)$:

$$H = \frac{P_{max}}{A_c} \tag{3.18}$$

The value of P_{max} can be obtained from the load-displacement graph (see example Figure. 3.3) and the contact area $A(h_c)$ can be obtained by following the relation in Eq. 3.17.

Pop-in

For a well-annealed ductile materials, pop-in indicates the onset of plasticity. It signifies the transition from elastic to elasto-plastic stage. Since the nucleation event happens in defect-free area, it is often called as "homogeneous dislocation nucleation" event. From isotropic continuum mechanics (Independent of crystal orientation), the maximum shear stress τ_{max} and its corresponding position $Z_{\tau(max)}$ during nano indentation can be expressed as [11]:

$$\tau_{max} = 0.31 \left(\frac{6E_r^2 P}{\pi^3 R^2} \right)^{1/3} \tag{3.19}$$

$$Z_{\tau(max)} = 0.48 \left(\frac{3PR}{4E_r} \right)^{1/3} \tag{3.20}$$

3.3.3 In-situ electrochemical indentation

The macro-scale mechanical test provides information about hydrogen influence on global properties. Typically a microstructure constitutes various features such as dislocations, vacancies, phase boundaries, precipitates, grain boundaries, and hydrogen interacts with each these constituents in varied manner. Understanding these interactions is essential to get mechanistic insights into HE phenomena. Further it can also aid modelling and development of failure prediction tools for industrial applications. One approach to study hydrogen interaction with different microstructural features in detail is to perform micro or nanoscale mechanical tests in hydrogen environment. Hydrogen being the smallest atom, poses several challenges in the HE study. Because of its inherent fast diffusing nature, constant hydrogen source is required for precise quantification of mechanical properties. The in-situ electrochemical nanoindentation tool (ECNI) serves this purpose quite reliably [86]. With the high resolution recording of LD data, it is possible to evaluate the nanomechanical properties such as elastic modulus, hardness, and discrete events such dislocation nucleation event, and phase transformation in hydrogen environment. This can aid faster screening of H-susceptible zones in the microstructure.

The nanoindentation test was carried out by using the Hysitron Triboindenter TI 950 equipped with a long-shaft Berkovich tip, which was used for both indenting and SPM imaging. The schematics of the setup is shown in Figure. 3.4a. Here the sample is cathode, platinum foil is used as counter electrode and Hg/Hg_2SO_4 as reference electrode. The electrolyte used in this work is Glycerol & Borax (sodium tetraborate decahydrate) mixture (2:1 ratio). The samples were charged electrochemically prior to indentation in hydrogen environment. The load function used in this work is shown in Figure. 3.4b. The loading and unloading rate was set as 8000 µN/s, with a maximum load of 2000 µN. Additionally, 0.25 s of holding time was added to unloading part at 10% of peak load for thermal drift correction. Post indentation, the SPM images were scanned to capture the changes in surface topography. The scan force was set as 2 µN at the rate of 1.5 Hz. The open source Gwyddion software was employed for post-processing of scanned images [87]. All the indents were executed at the room temperature.

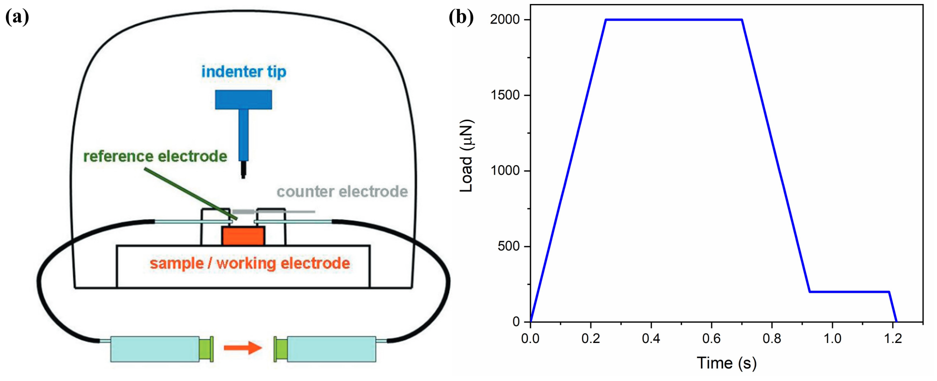
(a)
indenter tip
reference electrode
counter electrode
sample / working electrode
(b)
2000
1500
1000
500
0
Load (μN)
0.0
0.2
0.4
0.6
0.8
1.0
1.2
Time (s)

Figure 3.4: (a) Schematics of Nanoindentation setup. (b) Load function used in this work.

Chapter 4

Summary and further work

4.1 Summary of papers

The hydrogen degradation behavior of Alloy 625 is studied using multiscale in-situ experiments. The objectives defined in Chapter 1 are pursued in this doctoral work, and the main findings are published in three peer-reviewed articles, which are summarized below. **Article 1** addresses the effect of hydrogen on macroscale plastic deformation and mechanical degradation. **Article 2** investigates the hydrogen-induced variation in the nanomechanical response of Alloy 625. **Article 3** explores the hydrogen-induced softening and hardening behavior of pre-strained nickel alloy.

Article 1: Hydrogen-induced degradation behavior of nickel alloy studied using acoustic emission technique

The objective of this work is to investigate the effect of hydrogen on macroscale plasticity and mechanical degradation. To realize that a slow strain rate tensile test was performed on pre-charged samples, additionally in-situ acoustic emission (AE) monitoring technique was used to investigate the deformation process.

By using spectral analysis based clustering procedure during post-processing of AE signal, the information related to hydrogen-assisted cracks and deformation slip are separated and obtained over larger time scale (Figure. 4.1a). From the slip related information, the hydrogen effect on macroscale dislocation kinetics was studied. A phenomenological relation between AE power and slip behavior was used to estimate the relative mobile dislocation density, which was found to increase with the hydrogen concentration (Figure. 4.1b). In addition, a reduction in average dislocation velocity was observed for hydrogen-charged samples. This was attributed to hydrogen solute pinning the mobile dislocation thereby exhibiting enhanced hardening behavior. From the information related to the crack, three different stages of crack propagation in the present alloy are observed, and the duration of each stage varies with the severity of the charging. Additionally, advanced characterization tools were used to investigate the root cause of hydrogen-assisted cracks. The study reveals the crack transition from transgranular at the surface to intergranular in the interior of the sample. This apparent conflict is explained by linking the hydrogen diffusion profile with loading conditions. The graphical abstract which summarize the main findings of Article 1 is shown in Figure. 4.1.

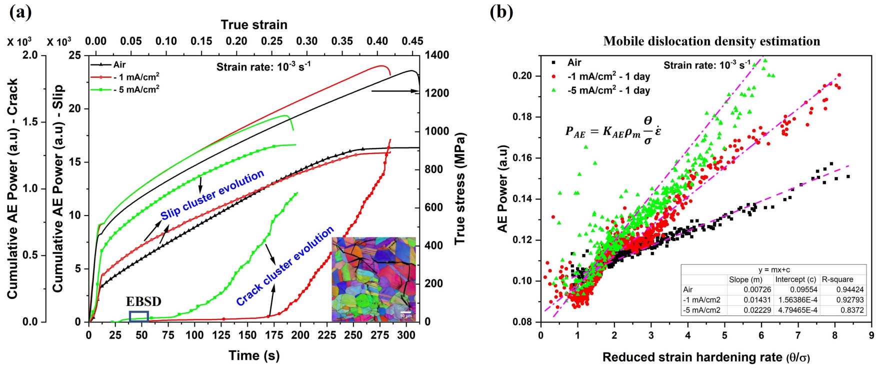

Figure 4.1: Graphical abstract for Article I. (a) The kinetics of individual source evolution represented by the cumulative AE power synchronized with the true stress-strain data. The inset in (a) shows the IPF map of H-charged sample from interrupted tensile test marked as EBSD. (b) Estimation of mobile dislocation density from the slope of AE power and reduced strain hardening rate plot for differently H-charged samples.

Article 2: Effect of hydrogen on nanomechanical properties of Inconel 625 studied using in-situ electrochemical nanoindentation technique

The study aimed to investigate how hydrogen affects the nanomechanical properties of Inconel 625 using the in-situ ECNI technique. The study presents hydrogen concentration-dependent changes in nanomechanical properties through the analysis of various stages of load-displacement curves.

The study reveals that the pop-in load is reduced by hydrogen in harmony with the "Defactant" mechanism. The reduction in dislocation line energy and stacking fault energy by hydrogen facilitates homogeneous dislocation nucleation. Additionally, the study also found that the duration of the secondary elastic post pop-in stage, which can be interpreted as the force required to activate the secondary source is reduced with the increase in hydrogen concentration. The hydrogen-induced frictional stress, estimated using the Nix-Gao model based on Tabor's relation, is found to be linearly dependent on the solute concentration, indicating that the dislocation motion is impeded by hydrogen atoms due to the solute drag effect. The result also shows that high cathodic charging can result in the slip line formation. This is due to sluggish diffusion and supersaturation of hydrogen at the surface, which generates internal stress exceeding the yield strength, triggering defect generation such as dislocations, vacancies, etc. The graphical abstract that summarizes the main findings of Article 2 is shown in Figure. 4.2.

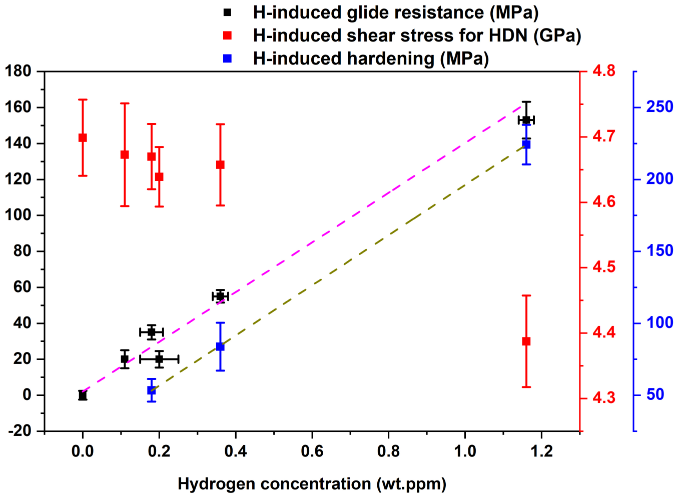

Figure 4.2: Graphical abstract for Article II. Hydrogen concentration-dependent nanomechanical properties of nickel alloy 625. Note that a linear relationship for glide resistance stress and frictional stress with hydrogen concentration (highlighted by dashed lines) suggests H-induced hardening. The homogenous dislocation nucleation (HDN) stress reduces with hydrogen content implying H-facilitated dislocation nucleation.

Article 3: Distinct evidence of hydrogen-enhanced defects formation on pre-strained nickel alloy 625 during in-situ electrochemical nanoindentation test

This work explores the effect of hydrogen on pre-strained Alloy 625 using in-situ electrochemical nanoindentation. The material was pre-strained to two different strain levels and subjected to similar hydrogen charging-discharging sequence. The graphical abstract that summarizes the main findings of Article 3 is shown in Figure. 4.3.

The findings indicate that after hydrogen charging, the hardness of the alloy increases with the pre-strain value. The hydrogen solute accumulation at the pre-existing lattice defect sites acts as an obstacle to mobile dislocations, i.e., it acts as a constraint to dislocation loop expansion, resulting in hydrogen-induced hardening. Additionally, increased hydrogen uptake reduces the stacking fault energy (SFE) locally, promoting mechanical twinning (Red dashed lines in TEM image in Fig. 4.3), which results in enhanced hardness in pre-strained material. The pre-strained sample exhibits the softening behavior during desorption. This is because the interaction of the hydrogen solute with pre-existing defects results in irreversible microstructural changes, such as hydrogen-enhanced vacancies. Our study suggests that during electrochemical charging, hydrogen solute interacts with pre-existing defects and modifies the microstructure permanently, leading to the creation of new crystal defects. This can promote hydrogen uptake and defect generation in an auto-catalytic manner, ultimately leading to failure.

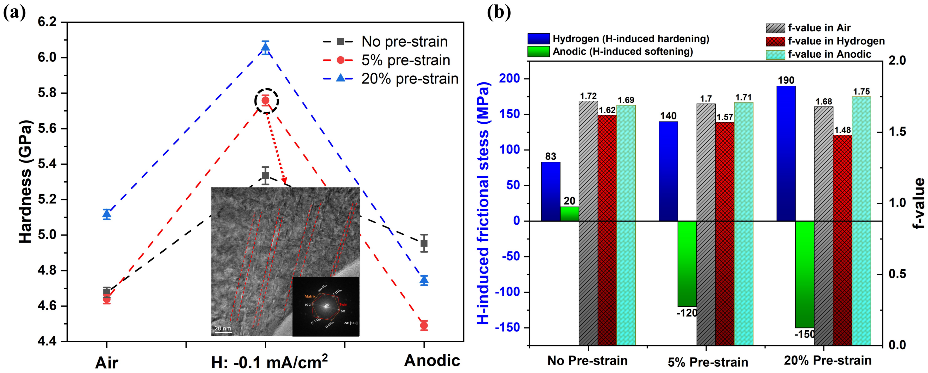

Figure 4.3: Graphical abstract for Article III. (a) Hardness data for differently pre-strained samples subjected to similar H-charging desorption cycle. The inset in (a) shows the TEM micrograph of indent performed in hydrogen. The red dashed lines highlight the deformation twins. (b) Summary of results from elastoplastic modelling.

4.2 Conclusion

The effect of hydrogen on the mechanical degradation of Alloy 625 was thoroughly investigated using various techniques, including slow strain rate tensile testing equipped with AE setup, in-situ electrochemical nanoindentation, and advanced characterization tools. The study unveiled the interaction between hydrogen and plasticity on the macroscale and nanoscale. The results obtained from different length scales are compared, and the major conclusion can be summarized as follows:

- The study revealed that electrochemical charging alone can result in surface deformation, including slip line formation and hydrogen-enhanced vacancy formation. This phenomenon results from high internal stress generated at the surface layers due to the combined effects of sluggish diffusion and hydrogen supersaturation. Additionally, the study emphasized that pre-existing defects in the material can accelerate this process. These pre-damages serve as preferential sites for crack initiation during mechanical loading, leading to premature failure. Therefore, it is crucial to take this effect into consideration in future HE studies.
- The AE-aided tensile test provided valuable insights into the hydrogen effect on macroscale plastic deformation. By employing a phenomenological relation between AE power and slip behavior, we estimated the relative mobile dislocation density, which was found to increase with the hydrogen concentration. At the bulk scale, the presence of atomic hydrogen in the Nickel lattice resulted in an increased population of mobile dislocations due to the reduction in critical stress required for Frank-Read source activation and loop expansion. These results are consistent with the findings of the in-situ ECNI study, which demonstrated that hydrogen facilitates dislocation nucleation and enhances slip activity by lowering the activation barrier for general plastic deformation to commence.

- The AE-aided tensile test also revealed a reduction in the average dislocation velocity for hydrogen-charged samples, suggesting the pinning of dislocations by hydrogen as the dominant mechanism for hydrogen-related hardening. Similarly, during the ECNI test, the hydrogen contribution to the lattice frictional stress was estimated using the Nix-Gao model based on Tabor's relation. The analysis indicated a linear dependence of the hydrogen-induced frictional stress on solute concentration, implying that dislocation motion is hindered by hydrogen atoms through the solute drag effect. Moreover, this effect becomes more pronounced with an increase in the pre-existing defect density in the material.
- The AE spectral-based cluster analysis reliably identifies the hydrogen-assisted crack nucleation and propagation process. In the hydrogen-charged samples, three stages of the damage evolution process are observed before macroscopic strain localization sets in: incubation, "slow" accumulation of surface cracks, and accelerated crack growth. The kinetic details of each stage have been unveiled, and it has been shown that the duration of each stage varies with the severity of charging.
- Postmortem characterization of crack propagation path reveals a transition from the transgranular to the intergranular type. Near the surface, pre-damage induced during charging and hydrogen accumulation at slip band intersections enable easy transgranular cracking along dislocation slip bands. In the bulk of the sample without any prior deformation, additional energy is needed to generate a dislocation and promote hydrogen transport to the intersections. With grain boundaries acting as strong trap sites for hydrogen, nucleating a crack along grain boundaries by decohesion becomes easier than generating a transgranular crack. Thus, the competition between hydrogen availability and transport determines the crack mode in this alloy.

Understanding the role of hydrogen in modifying the mechanical properties of nickel alloys under different conditions is crucial for developing reliable and durable materials for various engineering applications.

4.3 Further Work

Due to time limitations, some work could not be performed in the presented PhD study. Following are some of the avenues which can be looked further in the HE study:

- The current work manages to discriminate the hydrogen-assisted crack related information from slip-related information. More effort is required to connect these two stages to explain the embrittlement behavior. More systematic laboratory tests are required to correlate the AE characteristics with the microstructural evolution during loading to define the critical state preceding the failure.
- The study highlighted the AE's ability to resolve a small change in material's structure, hence it can serve as a useful tool for understanding the mechanism related to hydrogen-charging induced slip line formation in nickel alloys.
- The critical hydrogen concentration that trigger intergranular cracking of high

angle grain boundaries should be explored further by using small-scale testing methodologies.

- Hydrogen-influenced nanomechanical properties of annealed ductile material is well documented; further research must focus on the pre-strained/ strain hardened material. The role of inhomogenous defect distribution, strain-induced vacancies, dislocation density, etc, in influencing the HE behavior must be studied comprehensively.
- While this study managed to correlate the hydrogen-influenced dislocation behavior across different length scales, further studies should focus on establishing the relationship between nanomechanical data with the macroscale fracture behavior.

Bibliography

[1] Mariano Iannuzzi, Afrooz Barnoush, and Roy Johnsen. “Materials and corrosion trends in offshore and subsea oil and gas production”. In: *npj Materials Degradation* 1.1 (Dec. 2017), pp. 1–11.

[2] Ian M. Robertson et al. “Hydrogen Embrittlement Understood”. In: *Metallurgical and Materials Transactions B* 46.3 (June 2015), pp. 1085–1103.

[3] Alexander R. Troiano. “The Role of Hydrogen and Other Interstitials in the Mechanical Behavior of Metals (1959 Edward De Mille Campbell Memorial Lecture)”. In: *Metallography, Microstructure, and Analysis* 5.6 (Dec. 2016), pp. 557–569.

[4] K. Takai et al. “Lattice defects dominating hydrogen-related failure of metals”. In: *Acta Materialia* 56.18 (Oct. 2008), pp. 5158–5167.

[5] Y. Fukai, Y. Shizuku, and Y. Kurokawa. “Superabundant vacancy formation in Ni–H alloys”. In: *Journal of Alloys and Compounds* 329.1-2 (Nov. 2001), pp. 195–201.

[6] R. Kirchheim. “Reducing grain boundary, dislocation line and vacancy formation energies by solute segregationII. Experimental evidence and consequences”. In: *Acta Materialia* 55.15 (Sept. 2007), pp. 5139–5148.

[7] Helmuth Sarmiento Klapper, Jutta Klöwer, and Olesya Gosheva. “Hydrogen embrittlement: The game changing factor in the applicability of nickel alloys in oilfield technology”. In: *Philosophical Transactions of the Royal Society A: Mathematical, Physical and Engineering Sciences* 375.2098 (July 2017).

[8] Steven S. Shademan, John W. Martin, and Al P. Davis. *Uns N07725 Nickel Alloy Connection Failure.* Mar. 2012.

[9] William M Bailey et al. *Hydrogen Embrittlement Failure of a Precipitation Hardened Nickel Alloy Subsurface Safety Valve Component Installed in a North Sea Seawater Injection Well.* Mar. 2014.

[10] B. Saleem et al. “Alloy 718 Subsea Bolt in Relation to Surface Cracking: A Microstructural Perspective”. In: *Materials Sciences and Applications* 11.12 (Dec. 2020), pp. 787–816.

[11] Afrooz Barnoush and Horst Vehoff. “Recent developments in the study of hydrogen embrittlement: Hydrogen effect on dislocation nucleation”. In: *Acta Materialia* 58.16 (Sept. 2010), pp. 5274–5285.

[12] S.P. Lynch. “Hydrogen embrittlement (HE) phenomena and mechanisms”. In: *Stress Corrosion Cracking.* Elsevier, Jan. 2011, pp. 90–130.

[13] R. A. Oriani. “Whitney Award Lecture—1987: Hydrogen—The Versatile Embrittler”. In: *CORROSION* 43.7 (July 1987), pp. 390–397.

[14] M. Nagumo. “Hydrogen related failure of steels – a new aspect”. In: *Materials Science and Technology* 20.8 (Aug. 2004), pp. 940–950.

[15] R. Kirchheim and A. Pundt. *Hydrogen in Metals*. Fifth Edit. Vol. 1. Elsevier, 2014, pp. 2597–2705.

[16] O. Barrera et al. *Understanding and mitigating hydrogen embrittlement of steels: a review of experimental, modelling and design progress from atomistic to continuum*. May 2018.

[17] Keith B. Oldham, Jan C. Myland, and Alan M. Bond. *Electrochemical Science and Technology*. Chichester, UK: John Wiley & Sons, Ltd, Nov. 2011.

[18] J Crank. “The mathematics of diffusion. 2nd Edn.” In: (1979).

[19] A. Turnbull. “Hydrogen diffusion and trapping in metals”. In: *Gaseous Hydrogen Embrittlement of Materials in Energy Technologies*. Elsevier, 2012, pp. 89–128.

[20] A. Tehranchi, B. Yin, and W. A. Curtin. “Softening and hardening of yield stress by hydrogen–solute interactions”. In: *Philosophical Magazine* 97.6 (Feb. 2017), pp. 400–418.

[21] B. G. Pound. “Hydrogen trapping in work-hardened alloys”. In: *Acta Metallurgica Et Materialia* 39.9 (Sept. 1991), pp. 2099–2105.

[22] Motomichi Koyama et al. “Recent progress in microstructural hydrogen mapping in steels: quantification, kinetic analysis, and multi-scale characterisation”. In: *Materials Science and Technology (United Kingdom)* 33.13 (Sept. 2017), pp. 1481–1496.

[23] A. McNabb and P K Foster. “A New Analysis of the Diffusion of Hydrogen in Iron and Ferritic Steels”. In: *Transactions of the Metallurgical Society of AIME* 227.June (1963), p. 618.

[24] R.A. Oriani and P.H. Josephic. “Equilibrium aspects of hydrogen-induced cracking of steels”. In: *Acta Metallurgica* 22.9 (Sept. 1974), pp. 1065–1074.

[25] “The effect of occluded hydrogen on the tensile strength of iron”. In: *Proceedings of the Royal Society of London. Series A, Containing Papers of a Mathematical and Physical Character* 112.760 (Aug. 1926), pp. 182–195.

[26] R. A. Oriani. “The diffusion and trapping of hydrogen in steel”. In: *Acta Metallurgica* 18.1 (Jan. 1970), pp. 147–157.

[27] C.J. McMahon. “Hydrogen-induced intergranular fracture of steels”. In: *Engineering Fracture Mechanics* 68.6 (Apr. 2001), pp. 773–788.

[28] W. W. Gerberich, P. G. Marsh, and J. W. Hoehn. “Hydrogen induced cracking mechanisms - are there critical experiments?” In: *Hydrogen Effects in Materials*. Minerals, Metals & Materials Soc (TMS), Jan. 1996, pp. 539–551.

[29] Yaojun A. Du et al. “First-principles study on the interaction of H interstitials with grain boundaries in α- and γ-Fe”. In: *Physical Review B - Condensed Matter and Materials Physics* 84.14 (Oct. 2011), p. 144121.

[30] C D Beachem. “A new model for hydrogen-assisted cracking (hydrogen “embrittlement”)”. In: *Metallurgical and Materials Transactions B* 3.2 (Feb. 1972), pp. 441–455.

[31] I. M. Robertson, H. K. Birnbaum, and P Sofronis. *Chapter 91-Hydrogen Effects on Plasticity.* Vol. 15. 09. 2009, pp. 249–293.

[32] H.K. Birnbaum and P. Sofronis. “Hydrogen-enhanced localized plasticity—a mechanism for hydrogen-related fracture”. In: *Materials Science and Engineering: A* 176.1-2 (Mar. 1994), pp. 191–202.

[33] Shuai Wang et al. “Hydrogen-induced intergranular failure of iron”. In: *Acta Materialia* 69 (May 2014), pp. 275–282.

[34] S. P. Lynch. “A fractographic study of hydrogen-assisted cracking and liquid-metal embrittlement in nickel”. In: *Journal of Materials Science 1986 21:2* 21.2 (Feb. 1986), pp. 692–704.

[35] S. P. Lynch. “Environmentally assisted cracking: Overview of evidence for an adsorption-induced localised-slip process”. In: *Acta Metallurgica* 36.10 (Oct. 1988), pp. 2639–2661.

[36] Arnaud Metsue et al. “Contribution of the entropy on the thermodynamic equilibrium of vacancies in nickel”. In: *Journal of Chemical Physics* 140.10 (Mar. 2014).

[37] G. Hachet et al. “The influence of hydrogen on cyclic plasticity of <001> oriented nickel single crystal. Part II: Stability of edge dislocation dipoles”. In: *International Journal of Plasticity* 129 (June 2020), p. 102667.

[38] Yu Ding et al. “Hydrogen-enhanced grain boundary vacancy stockpiling causes transgranular to intergranular fracture transition”. In: *Acta Materialia* 239 (Oct. 2022), p. 118279.

[39] S. K. Lawrence, B. P. Somerday, and R. A. Karnesky. “Elastic Property Dependence on Mobile and Trapped Hydrogen in Ni-201”. In: *JOM* 69.1 (Jan. 2017), pp. 45–50.

[40] Joseph R Davis. *Nickel, Cobalt, and Their Alloys.* 2000.

[41] R. J. Walter, R. P. Jewett, and W. T. Chandler. “On the mechanism of hydrogen-environment embrittlement of iron- and nickel-base alloys”. In: *Materials Science and Engineering* 5.2 (Jan. 1970), pp. 99–110.

[42] L Fournier, D Delafosse, and T Magnin. “Cathodic hydrogen embrittlement in alloy 718”. In: *Materials Science and Engineering: A* 269.1-2 (Aug. 1999), pp. 111–119.

[43] F. Lecoester, J. Chêne, and D. Noel. “Hydrogen embrittlement of the Ni-base Alloy 600 correlated with hydrogen transport by dislocations”. In: *Materials Science and Engineering: A* 262.1-2 (Apr. 1999), pp. 173–183.

[44] Zhenbo Zhang et al. “Hydrogen assisted crack initiation and propagation in a nickel-based superalloy”. In: *Acta Materialia* 113 (July 2016), pp. 272–283.

[45] X. Lu et al. “Effect of electrochemical charging on the hydrogen embrittlement susceptibility of alloy 718”. In: *Acta Materialia* 179 (Oct. 2019), pp. 36–48.

[46] J. E. Angelo, N. R. Moody, and M. I. Baskes. “Trapping of hydrogen to lattice defects in nickel”. In: *Modelling and Simulation in Materials Science and Engineering* 3.3 (1995), pp. 289–307.

[47] Xu Lu et al. “The effect of plastic deformation on hydrogen diffusion in nickel Alloy 625”. In: *Scripta Materialia* 226 (Mar. 2023), p. 115210.

[48] Z. Tarzimoghadam et al. “Hydrogen-assisted failure in Ni-based superalloy 718 studied under in situ hydrogen charging: The role of localized deformation in crack propagation”. In: *Acta Materialia* 128 (Apr. 2017), pp. 365–374.

[49] D. H. Lassila and H. K. Birnbaum. “The effect of diffusive segregation on the fracture of hydrogen charged nickel”. In: *Acta Metallurgica* 36.10 (Oct. 1988), pp. 2821–2825.

[50] M.L. Martin et al. “Hydrogen-induced intergranular failure in nickel revisited”. In: *Acta Materialia* 60.6-7 (Apr. 2012), pp. 2739–2745.

[51] Zachary D. Harris et al. “Elucidating the contribution of mobile hydrogen-deformation interactions to hydrogen-induced intergranular cracking in polycrystalline nickel”. In: *Acta Materialia* 158 (Oct. 2018), pp. 180–192.

[52] Tarlan Hajilou et al. “Hydrogen-enhanced intergranular failure of sulfur-doped nickel grain boundary: In situ electrochemical micro-cantilever bending vs. DFT”. In: *Materials Science and Engineering A* 794 (Sept. 2020), p. 139967.

[53] Xu Lu et al. “In situ nanomechanical characterization of hydrogen effects on nickel-based alloy 725 under different metallurgical conditions”. In: *Journal of Materials Science & Technology* (Aug. 2022).

[54] Z. Tarzimoghadam et al. “Multi-scale and spatially resolved hydrogen mapping in a Ni-Nb model alloy reveals the role of the δ phase in hydrogen embrittlement of alloy 718”. In: *Acta Materialia* 109 (May 2016), pp. 69–81.

[55] Reiner Kirchheim. “Solid solution softening and hardening by mobile solute atoms with special focus on hydrogen”. In: *Scripta Materialia* 67.9 (Nov. 2012), pp. 767–770.

[56] M. Wen, S. Fukuyama, and K. Yokogawa. “Atomistic simulations of effect of hydrogen on kink-pair energetics of screw dislocations in bcc iron”. In: *Acta Materialia* 51.6 (Apr. 2003), pp. 1767–1773.

[57] Daniel P. Abraham and Carl J. Altstetter. “Hydrogen-enhanced localization of plasticity in an austenitic stainless steel”. In: *Metallurgical and Materials Transactions A* 26.11 (Nov. 1995), pp. 2859–2871.

[58] H. L. Dunegan, D. O. Harris, and C. A. Tatro. “Fracture analysis by use of acoustic emission”. In: *Engineering Fracture Mechanics* 1.1 (1968).

[59] John P. McCrory et al. “Acoustic Emission Monitoring of Metals”. In: *Springer Tracts in Civil Engineering*. Springer Science and Business Media Deutschland GmbH, 2022, pp. 529–565.

[60] C R Heiple and S H Carpenter. “Acoustic Emission Produced by Deformation of Metals and Alloys”. In: *J. Acoust. Em.* 6 (1987), p. 177.

[61] B. A. Auld and Robert E. Green. “ Acoustic Fields and Waves in Solids: Two Volumes ”. In: *Physics Today* 27.10 (1974).

[62] C B Scruby, H N G Wadley, and J J Hill. “Dynamic elastic displacements at the surface of an elastic half-space due to defect sources”. In: *Journal of Physics D: Applied Physics* 16.6 (June 1983), pp. 1069–1083.

[63] J Nondestruct Eval et al. “Acoustic Emission Sensor Calibration for Absolute Source Measurements”. In: ().

[64] A. Vinogradov, I. S. Yasnikov, and Y. Estrin. “Stochastic dislocation kinetics and fractal structures in deforming metals probed by acoustic emission and surface topography measurements”. In: *Journal of Applied Physics* 115.23 (June 2014), p. 233506.

[65] N. Kiesewetter and P. Schiller. “The acoustic emission from moving dislocations in aluminium”. In: *physica status solidi (a)* 38.2 (Dec. 1976), pp. 569–576.

[66] N. Kiesewetter. “Acoustic emission from moving dislocations”. In: *Scripta Metallurgica* 8.3 (Mar. 1974), pp. 249–252.

[67] Y. Bergström. “A dislocation model for the stress-strain behaviour of polycrystalline α-Fe with special emphasis on the variation of the densities of mobile and immobile dislocations”. In: *Materials Science and Engineering* 5.4 (Mar. 1970), pp. 193–200.

[68] A. Yu Vinogradov and D. L. Merson. “The nature of acoustic emission during deformation processes in metallic materials”. In: *Low Temperature Physics* 44.9 (Sept. 2018), pp. 930–937.

[69] S. Martin et al. “Deformation behaviour of TWIP steels: Constitutive modelling informed by local and integral experimental methods used in concert”. In: *Materials Characterization* 184 (Feb. 2022), p. 111667.

[70] A. Vinogradov et al. “Kinetics of deformation processes in high-alloyed cast transformation-induced plasticity/twinning-induced plasticity steels determined by acoustic emission and scanning electron microscopy: Influence of austenite stability on deformation mechanisms”. In: *Acta Materialia* 61.7 (Apr. 2013), pp. 2434–2449.

[71] M. Linderov et al. “Deformation mechanisms in austenitic TRIP/TWIP steels at room and elevated temperature investigated by acoustic emission and scanning electron microscopy”. In: *Materials Science and Engineering: A* 597 (Mar. 2014), pp. 183–193.

[72] K. Ono. *Current understanding of mechanisms of acoustic emission.* 2005.

[73] Darrell R. James and Steve H. Carpenter. “Relationship between acoustic emission and dislocation kinetics in crystalline solids”. In: *Journal of Applied Physics* 42.12 (Nov. 1971), pp. 4685–4697.

[74] Alexei Vinogradov et al. “Effect of grain size on the mechanisms of plastic deformation in wrought Mg-Zn-Zr alloy revealed by acoustic emission measurements”. In: *Acta Materialia* 61.6 (Apr. 2013), pp. 2044–2056.

[75] Adrian A. Pollock. “Material brittleness and the energetics of acoustic emission”. In: *Conference Proceedings of the Society for Experimental Mechanics Series.* Vol. 5. 2011.

[76] Eraldo Pomponi and Alexei Vinogradov. “A real-time approach to acoustic emission clustering”. In: *Mechanical Systems and Signal Processing* 40.2 (Nov. 2013), pp. 791–804.

[77] A. Vinogradov et al. “Correlation between Spectral Parameters of Acoustic Emission during Plastic Deformation of Cu and Cu-Al Single and Polycrystals”. In: *Materials Transactions, JIM* 36.3 (1995), pp. 426–431.

[78] Alexel Yu Vinogradov. “Principles of statistical and spectral analysis of acoustic emission and their application to plastic deformation of metallic glasses”. In: *Journal of acoustic emission* 16 (1998), S158–S169.

[79] P. Welch. “The use of fast Fourier transform for the estimation of power spectra: A method based on time averaging over short, modified periodograms”. In: *IEEE Transactions on Audio and Electroacoustics* 15.2 (June 1967), pp. 70–73.

[80] A. Vinogradov, V. Patlan, and S. Hashimoto. “Spectral analysis of acoustic emission during cyclic deformation of copper single crystals”. In: *Philosophical Magazine A* 81.6 (June 2001), pp. 1427–1446.

[81] KL Johnson. *Contact mechanics.* 1987.

[82] Cripps Anthony C. Fischer. *Nanoindentation, 3rd Edition.* Vol. 99. C. 2011.

[83] Heinrich Hertz. “Ueber die Berührung fester elastischer Körper.” In: *crll* 1882.92 (1882), pp. 156–171.

[84] Ian N. Sneddon. “The relation between load and penetration in the axisymmetric boussinesq problem for a punch of arbitrary profile”. In: *International Journal of Engineering Science* 3.1 (May 1965), pp. 47–57.

[85] GM Pharr WC Oliver. “An improved technique for determining hardness and elastic modulus using load and displacement sensing indentation experiments”. In: *J. Mater. Res.* 7 (1992), pp. 1564–1583.

[86] Afrooz Barnoush and Horst Vehoff. “Electrochemical nanoindentation: A new approach to probe hydrogen/deformation interaction”. In: *Scripta Materialia* 55.2 (July 2006), pp. 195–198.

[87] D. Nečas and P. Klapetek. “Gwyddion – Free SPM (AFM, SNOM/NSOM, STM, MFM, . . .) data analysis software”. In: *Central European Journal of Physics* 10 (2012).

Part II

Article I

Hydrogen-induced degradation behavior of nickel alloy studied using acoustic emission technique

CK Soundararajan, A Myhre, A Sendrowicz, X Lu, A Vinogradov

Materials Science and Engineering: A, 865 (2023), 144635.

Materials Science & Engineering A 865 (2023) 144635

Contents lists available at ScienceDirect

Materials Science & Engineering A

journal homepage: www.elsevier.com/locate/msea

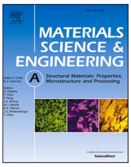

Hydrogen-induced degradation behavior of nickel alloy studied using acoustic emission technique

Chandrahaasan K. Soundararajan [a,*], Aleksander Myhre [a,1], Aleksander Sendrowicz [a,2], Xu Lu [a], Alexey Vinogradov [a,b,**,3]

[a] *Department of Mechanical and Industrial Engineering, Norwegian University of Science and Technology, No-7491, Trondheim, Norway*
[b] *Magnesium Research Center (MRC), Kumamoto University, 2-39-1 Kurokami, Chuo-ku, Kumamoto, 860-8555, Japan*

ARTICLE INFO

Keywords:
Hydrogen embrittlement
Acoustic emission
Dislocation kinetics
Microcracks
Nickel alloy

ABSTRACT

Hydrogen embrittlement susceptibility of nickel alloy (Inconel 625) is examined by a conventional strain rate tensile test (10^{-3} s^{-1}) equipped with an acoustic emission (AE) setup. From the spectral analysis of AE signals coupled with the clustering procedure followed by the electron microscopic characterization, we have demonstrated the capability of the AE technique in identifying the hydrogen-dislocation interactions, crack initiation and propagation in various hydrogen-charged samples. The enhanced hardening behavior of hydrogen-charged samples is investigated from the viewpoint on the elementary dislocation theory, using a phenomenological relationship between the acoustic emission power and the experimentally measurable strain hardening parameters derived from the monotonic tensile test. In this way, we have shown that the mobile dislocation density increases with hydrogen content. In addition, the average velocity of dislocations is assessed from the AE data, and it is found to be reduced with the hydrogen concentration. The statistical crack analysis reveals the crack transition from the transgranular to intergranular mode in the samples failed under the hydrogen environment. The competition between these two fracture modes is explained by relating the hydrogen concentration profile with loading conditions.

1. Introduction

Hydrogen embrittlement (HE) results from a complex interplay between the material, environment and the stress state, which makes it an intricate problem, particularly in structural materials, as it may cause drastic failure at service. The HE behavior in engineering materials is often explained by the following mechanisms acting either individually or in various combinations [1]: hydrogen-enhanced localized plasticity (HELP) [2–5], hydrogen-enhanced decohesion (HEDE) [6,7], hydrogen adsorption induced dislocation emission (AIDE) [8–10], hydrogen enhanced strain induced vacancy formation (HESIV) [11–15], hydrogen as a “Defactant” [16–18], and the brittle hydride formation [19,20].

It has been well established that HE in engineering materials is intrinsically associated with dislocation behavior, which is spatially inhomogeneous and temporarily intermittent by nature. Over the years, extensive research efforts have been dedicated to understanding the underlying mechanisms through the development of various state-of-the-art instruments, advanced characterization tools and computing resources. For instance, in-situ electrochemical nanoindentation experiments [16,21,22] provided direct experimental evidence for the hydrogen-induced reduction of the activation energy for homogenous dislocation nucleation in line with expectations from the ‘Defactant’ model [18]. Using in situ transmission electron microscopy, Ferreira et al. have shown that the mobility of dislocation increases in a hydrogen environment [23], underpinning the HELP mechanism [2]. In-situ mechanical testing in the scanning electron microscope (SEM) enabled direct observation of the hydrogen-assisted crack path and the related plastic behavior [4,24,25]. The thermal activation analysis using the strain rate jump and stress relaxation testing at constant temperature helped to assess the hydrogen-influenced activation volume and

---

[*] Corresponding author.
[**] Corresponding author. Department of Mechanical and Industrial Engineering, Norwegian University of Science and Technology, No-7491, Trondheim, Norway.
E-mail addresses: chandrahaasan.k.soundararajan@ntnu.no (C.K. Soundararajan), alexei.vinogardov@ntnu.no, vinogradov@kumamoto-u.ac.jp (A. Vinogradov).
[1] Currently at DNV AS, Høvik 1363, Norway.
[2] Currently at Kilter AS, Viken 1405, Norway.
[3] Currently at Kumamoto University, Kumamoto 860–8555, Japan.

https://doi.org/10.1016/j.msea.2023.144635
Received 28 October 2022; Received in revised form 6 January 2023; Accepted 11 January 2023
Available online 13 January 2023
0921-5093/© 2023 The Authors. Published by Elsevier B.V. This is an open access article under the CC BY license (http://creativecommons.org/licenses/by/4.0/).

dislocation mobility [5]. In the case of Ni and Ni–C alloys, hydrogen was shown to increase the dislocation velocity by reducing the activation barrier [26]. Although these experimental tools provide detailed insight into the hydrogen-dislocation interactions, the observed effects might not represent the behavior of the entire volume being probed. The local site-specific observations can not help to interrelate the dislocation kinetics and the hydrogen effects over the bulk scale, since the influence of the solute atoms on the collective movement and storage of dislocations at the macroscale is a complex problem. The use of the complementary acoustic emission (AE) technique, which is extremely sensitive to local stress relaxations occurring in solids under mechanical or/and chemical stimulus, can address these issues, as the AE information aggregated from multiple local sources is averaged over the entire volume.

Nickel alloys are used in many safety-critical components in oil and gas industries owing to their outstanding combination of high strength and corrosion resistance; however, HE is a pertinent, crucial issue in the mentioned industries [27–29]. Hydrogen-assisted intergranular and transgranular cracking have been reported in Nickel alloys [3,4,30,31]. Hydrogen accumulation at the dislocation slip band intersections promotes void nucleation and crack propagation along the slip bands, and this process is considered to be primarily responsible for the transgranular fracture. Intergranular cracks tend to initiate at the grain boundaries containing deleterious precipitates, such as the delta phase [3], sigma phase, and/or embrittling elements, such as Sulphur [32]. For a pure polycrystalline material with a simple microstructure, the combined effect of the applied stress and hydrogen transport by mobile dislocations to grain boundaries weakens the boundary region, thereby initiating and promoting intergranular cracks [33,34]. Nevertheless, both intergranular and transgranular cracks in Nickel alloys are reported to be a plasticity-mediated event as is evident from the strain localization around the cracks and through the characterization of the fracture surface [34–36]. Although the hydrogen-assisted crack formation mechanisms are well accepted, the engineering community needs to identify the safe load/stress conditions for the crack initiation in structural materials under the hydrogen-containing environment and service temperature. Although modern in-situ microscopy tools enable precise crack identification, these methods are only capable of observing the surface cracks and their temporal resolution for the crack detection is limited. Addressing both these issues, the in-situ AE technique can be a valuable companion to microscopic studies.

Acoustic emission is a transient elastic wave generated by rapid energy release during plastic deformation. The most common sources of AE waves during plastic deformation and fracture of metals include the dislocation motion, mechanical twinning, breaking of inclusions, precipitates or second phase particles, and microcrack nucleation and growth [37]. The microsecond temporal resolution of the AE technique offers a distinct advantage in studying the kinetics of damage evolution in the solids under load. Moreover, the information obtained is pertinent to the entire deforming volume. The use of the AE technique for understanding the HE mechanisms is sparse but not new [38–44]. Most of the early AE research was centered around characterizing the burst-type signals to identify the hydrogen-induced (or affected) cracks. Often, the information regarding the low-emission mechanisms, such as the dislocation slip generating continuous low-amplitude waveforms, is lost due to either the high pre-set threshold limit or the low sensitivity of the transducer. The contemporary threshold-less acquisition mode is advantageous because it enables the streaming data to be recorded continuously throughout the test. Besides, the modern post-processing technique involving the multiparametric statistical analysis, and spectral shape categorization of the AE waveforms combined with the microscopic structural characterization, permits to identify the source mechanism and relate to the loading conditions quite reliably. Plastic deformation and hydrogen-assisted crack propagation often occur concomitantly throughout the test, and the AE technique aims at discriminating the underlying sources and following their evolution individually.

In this work, we have employed the AE technique to study the deformation and cracking behavior during the uniaxial monotonic tensile testing of the hydrogen-precharged Inconel 625 alloy. Using a spectral shape classifier in the post-processing signal analysis, the time-resolved information is obtained regarding the evolution of the dislocation slip and the microcracks. The crack initiation and propagation in the hydrogen-charged samples are characterized using SEM after the interrupted tensile tests. The hydrogen-assisted slip behavior is compared for different hydrogen concentrations. Using a phenomenological relationship between the acoustic emission and dislocation kinetics, the mobility of dislocations is assessed, and the fine details of the embrittlement mechanism are unveiled and discussed.

2. Experimental

2.1. Sample preparation and electrochemical charging

The Inconel 625 alloy was hot rolled and homogenized at 885 °C for 1 h. The chemical composition of the alloy is reported in Table 1. The double dog-bone shaped tensile samples (see inset in Fig. 3a) were fabricated using the electric discharge machine. Prior to electrochemical charging, the samples were grounded and polished until 200 nm colloidal silica suspension with the objective to examine the hydrogen effects on the surface modifications directly and minimize any external influence by the mechanical grinding. The samples were precharged using a three-electrode electrochemical cell where a Platinum mesh was used as a counter electrode (anode), the test specimen was a cathode, and a saturated Ag/AgCl (3 M KCl) served as a reference electrode. Glycerol and phosphoric acid mixture (2:1) was used as an electrolyte, the temperature of which was set at 75 °C with the aim of promoting hydrogen uptake. The samples were precharged at three different current densities (−1 mA/cm^2, -5 mA/cm^2, and -10 mA/cm^2) for 24 h to study the influence of hydrogen concentration on the mechanical properties.

2.2. Tensile test with acoustic emission and DIC setup

Prior to testing the precharged samples, the stochastic speckle pattern for DIC measurement was created using black and white paint. The wideband Pico (MISTRAS, USA) acoustic sensor was attached to the shoulder of the sample (see inset in Fig. 3a) with Molykote 33 silicone-based grease serving as a coupling medium. The AE streams were recorded in the thresholdless mode triggered a few seconds before the loading started. The AE signals were amplified by 60 dB by a low noise 2/4/6 pre-amplifier in the frequency range of 100–1000 kHz before they were continuously recorded by the 16-bit PCI-2 board (MISTRAS, USA) at a sampling rate of 2 Msamples/s. The dwell time from removing the sample from the electrochemical cell and assembling it in a tensile setup was controlled within 10 min; thus, the hydrogen desorption during this time was negligible. Tensile tests were performed using a rigid screw-driven Kammrath & Weiss tensile/compression module at a constant displacement rate of 10 μm/s (equivalent nominal strain rate of 10^{-3} s^{-1}).

2.3. Microstructure characterization and hydrogen measurement

Electron microscopic characterization using electron backscattered diffraction (EBSD), back-scattered imaging (BSE), and fracture analysis

Table 1
Chemical composition of Inconel 625.

Element	Ni	Cr	Mo	Fe	Nb	Al	P
wt. %	62.8	21.3	8.3	3.7	3.25	0.22	<0.005
Element	C	Ti	Mn	Si	Cu	Co	S
wt. %	0.018	0.05	0.07	0.08	0.02	0.18	0.0003

in secondary electron contrast were carried out using the Quanta 650 FEG microscope (Thermo Fisher Inc.). The EBSD patterns were acquired by a NORDIF camera, and the subsequent indexing and analysis were conducted using the TSL OIM software. The total hydrogen content (Table 2) was estimated by the hot extraction method using the Bruker G4 Phoenix DH hydrogen analyzer. The X-ray diffraction (XRD) analysis was carried out using the D8 Focus operated at 40 keV at the fixed slit width of 0.2 mm using Cu radiation with the diffraction vector aligned parallel to the tensile direction. The scan was performed from 40° to 100° at a step size of 0.013°. Nano hardness measurements were carried out using the TI950 Triboindenter, the maximum load was set as 8000 μN, and the loading and unloading rate was 1000 μN/s.

2.4. *Acoustic emission signal processing*

Acoustic emission is a transient elastic wave generated during deformation. The surface displacement caused by rapid energy release is recorded by the transducer. The following steps of signal processing were implemented using the adaptive sequential *k*-means (ASK) algorithm [45].

- The continuous stream of data was sectioned into a set of individual realizations with a frame size of 4096 samples with 50% overlap to reduce the spectral leakage and the Fast Fourier transform algorithm was applied.
- For each realization, the power spectral density (PSD), *G(f)*, function is estimated using the Welch method. The PSD of the laboratory-background noise, which had been recorded prior to the test, was computed and subtracted from each realization.
- From the noise-corrected power spectrum, a set of AE parameters was obtained, of which the median frequency and acoustic emission power were used as a couple of primary descriptive variables; these variables were chosen on the basis of the statistical factor analysis [46] and the physical arguments presented in Refs. [47–49]. The average power per realization (referred to 1 Ohm nominal impedance) is calculated as

$$P_{AE} = \int_{f_{min}}^{f_{max}} G(f)df \tag{1}$$

- The median frequency, f_m, is defined using the implicit relation

$$\int_{f_{min}}^{f_m} G(f)df = \int_{f_m}^{f_{max}} G(f)df \tag{2}$$

where f_{min} and f_{max} refer to the minimum and maximum frequency detectable by the transducer, respectively. Since PSDs are the “fingerprints” of the source mechanisms, the spectral shape categorization is employed for grouping similar (and ungrouping dissimilar) data. The adaptive sequential *k*-means clustering algorithm (ASK), which is a non-supervised process with the a priori undefined number of clusters, uses normalized to unity PSD as an input for pairwise comparison. The mathematical details of the classifier can be found in Ref. [45]. Detailed interpretation of AE signals in both the hydrogen-free and hydrogen-charged conditions is provided in Section 3.3.

Table 2
Hydrogen content measurement.

Charging condition	Total Hydrogen concentration (wt. ppm)
-1 mA/cm^2 – 24 h	14.6 ± 1.37
-5 mA/cm^2 – 24 h	64 ± 4.6
-10 mA/cm^2 – 24 h	183 ± 8.7

3. Results

3.1. *Microstructure of H-free and H-charged samples*

The initial microstructure of Inconel 625 is shown in Fig. 1. This figure reveals the homogenous distribution of grains with an average grain size of 10 μm. The fraction of the special $\sum 3$ CSL boundaries (or annealing twins) represented by white lines in the inverse pole figure (IPF) map reaches 45%. The BSE map, Fig. 1b, highlights (in white) the grain boundaries decorated with discontinuous carbides (<1% area fraction) enriched by Nb and Mo, as is evidenced by the energy dispersive X-ray spectrum in Fig. 1c. Detailed characterization of the material has been reported in the earlier work focused on electrochemical permeation [50,51].

Electrochemical hydrogen charging-induced surface deformation was observed on the samples charged at -5 mA/cm^2 and -10 mA/cm^2 (Fig. 2a). The XRD is a powerful technique for the determination of volume change, phase transformation and strain gradients produced by the diffused hydrogen. The information provided by the XRD technique is statistically relevant as the depth being probed is ~10 μm. Fig. 2 shows the XRD patterns measured before hydrogen charging, right after charging (-10 mA/cm^2) and 24 h after charging. The uncharged sample exhibits characteristic FCC peaks with angular positions corresponding to the lattice parameter of 0.35871 nm.

The pattern measured immediately after charging shows an asymmetric peak shape, and the peak intensity reduces drastically when compared to the uncharged state (Fig. 2b). In general, peak broadening occurs when the crystal lattice is distorted and divided into smaller incoherently diffracting domains due to randomly stored dislocations or their ordered arrays (such as low-angle grain boundaries or pileups); stacking faults, twins and/or other imperfections contribute to the peak broadening too [52]. Hydrogen atoms occupy the octahedral sites in the Nickel lattice, thus, causing lattice dilatation. The peak broadening in the present case was most likely the result of the formation of a non-uniform solid solution of hydrogen in the FCC Nickel lattice; in other words, the hydrogen concentration gradient results in the observed asymmetric peak shape. The retention of the peak position and the intensity of the pattern measured after one day of charging suggest a hydrogen-induced elastic mismatch. The lattice parameter measured right after charging is 0.35901 nm. The XRD pattern for -1 mA/cm^2 samples shows no evidence of the peak shape change, displacement, or broadening; in addition, the SE image shows that the microstructure of these samples remains intact after charging (see Supplementary Material Fig. 1).

3.2. *Tensile test and fracture*

The flow stress-strain data for the hydrogen-free and hydrogen-charged samples along with their mechanical properties, are shown in Fig. 3. The flow curves of hydrogen-charged samples demonstrate a hardening behavior. The increase in the conventional yield stress (0.2% offset) with respect to the uncharged condition is observed for all the hydrogen-charged samples (12% for -1 mA/cm^2, 14% for -5 mA/cm^2 and 7.7% for -10 mA/cm^2, respectively). In addition, the drastic reduction in the fracture elongation with the applied potential in the samples failed under hydrogen occlusion is observed (2.5% for -1 mA/cm^2, 36.8% for -5 mAcm^2 and 54.6% for -10 mA/cm^2, respectively).

Fractographic images of the samples tested in air and hydrogen-charged conditions are shown in Fig. 4. The uncharged sample shows a typical dimpled surface characteristic of ductile fracture due to microvoids coalescence. In the hydrogen-charged samples, the typical embrittlement features are observed in the following order as they appear from the sample’s edge: the brittle zone followed by the mixed fracture zone and the ductile zone. The progressive increase in the brittle and mixed fracture zone size is observed with the applied current density. Both intergranular and transgranular (extensive slip steps) features

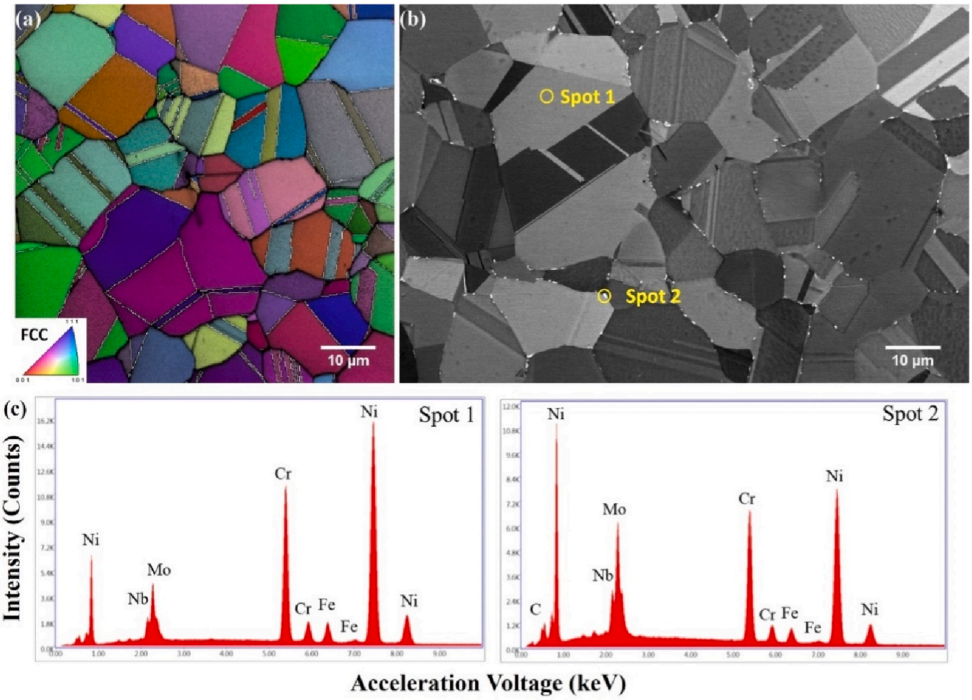
(a)
FCC
111
001
101
10 µm
(b)
Spot 1
Spot 2
10 µm
(c)
Spot 1
Ni
Nb
Mo
Cr
Cr
Fe
Fe
Ni
Ni
Spot 2
C
Ni
Nb
Mo
Cr
Cr
Fe
Fe
Ni
Ni
Intensity (Counts)
Acceleration Voltage (keV)

Fig. 1. Microstructure of the Inconel 625. (a) Inverse pole figure (IPF) map overlayed with image quality map. (b) BSE image depicts the precipitation at grain boundaries. (c) Energy dispersive X-ray spectrum data for two spots marked on the BSE image.

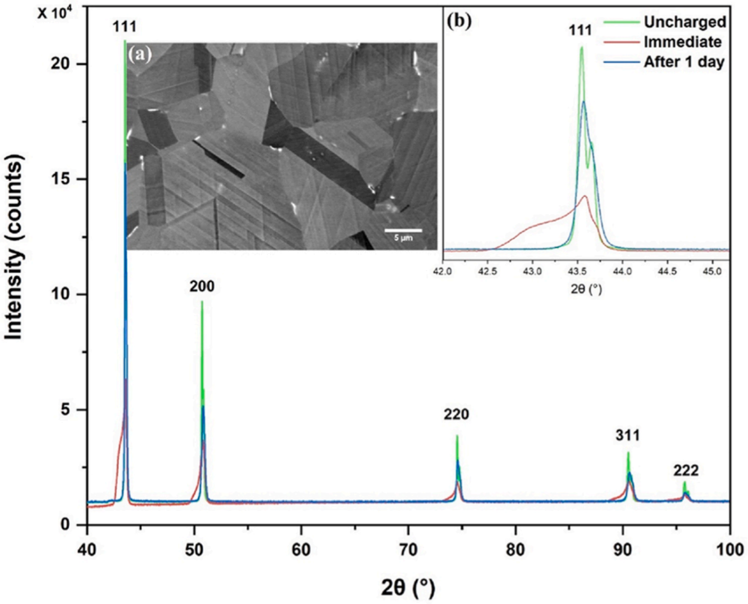

Fig. 2. The XRD pattern for the hydrogen charged sample (-10 mA/cm^2). The patterns recorded before charging (Green), right after charging (Red) and after a day (Blue) are overlayed for comparison. The inset (a) shows the charging induced deformation microstructure. (b) The enlarged region corresponds to the (111) peak. (For interpretation of the references to colour in this figure legend, the reader is referred to the Web version of this article.)

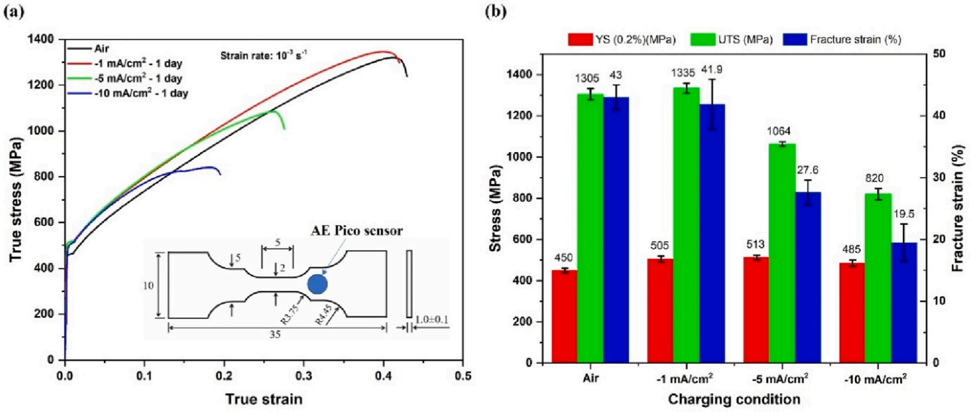

Fig. 3. (a) Flow stress vs. logarithmic strain plot for different hydrogen charged samples. Inset shows the dimension (in mm) of the tensile specimen used in this work along with the position of the AE sensor. (b) The corresponding mechanical properties data.

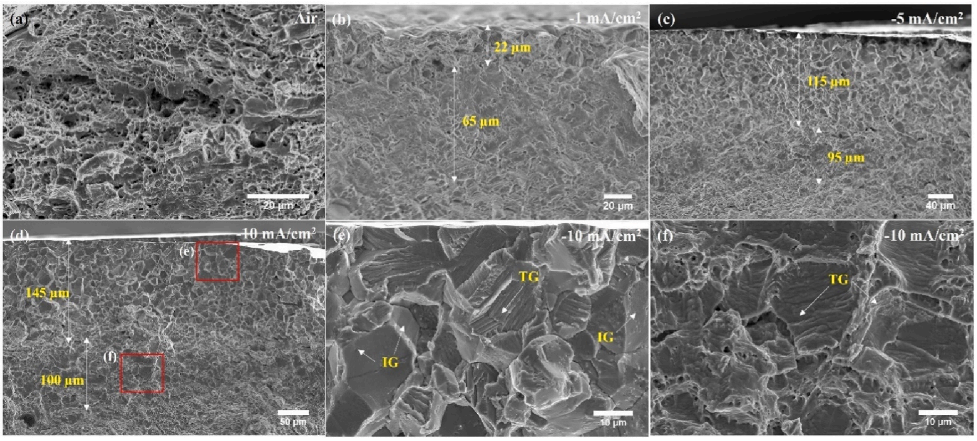

Fig. 4. Fracture surfaces of different hydrogen charged samples along with the information about brittle fracture depth. (a) Air. (b) −1 mA/cm^2 (c) −5 mA/cm^2 (d) −10 mA/cm^2 (e, f) Fracture surfaces at the higher magnification for the regions highlighted in (d). (IG: Intergranular features; TG: Transgranular features).

are observed at the brittle zone (see Fig. 4e and f and Supplymentary material – Fig. 2).

3.3. Acoustic emission results

AE results for the hydrogen-free and hydrogen-charged samples are compared in this section. The detailed characterization of the AE signals is structured into individual sub-sections in the following order:

- The raw AE signals results are presented in section 3.3.1
- The mathematical background for the signal processing and linking the AE parameters to the strain hardening process is briefly presented in section 3.3.2
- The significance of AE power and median frequency for characterization of the work hardening behavior at different charging conditions is explained in section 3.3.3
- The methodology to identify different AE sources operating during plastic deformation is discussed in section 3.3.4
- The kinetics of the evolution of individual sources with plastic strain is presented in section 3.3.5

3.3.1. AE time history during tensile test

Representative raw acoustic emission streams acquired continuously during tensile test for air and hydrogen-charged (−5 mA/cm^2) samples together with the load-elongation data are shown in Fig. 5. The laboratory noise recorded prior to the test is characterized by the low-amplitude stationary signal, which is visible on the lefthand side of the diagrams prior to the beginning of loading. The sharp peak of the acoustic emission activity is observed at the onset of plastic yielding, which is typically observed in FCC metals and alloys, where plastic deformation and strain hardening is governed by dislocation motion and interactions, respectively. For both air and hydrogen-charged samples, the profuse AE activity was observed in the form of random overlapping burst signals, which is particularly pronounced close to the yield point followed by the propagation of the Lüders front. Similar behavior has been reported earlier for many materials exhibiting the yield point phenomenon, *e.g.*, for BCC α-Iron [53] and recently for Cu–Zn alloys [54]. The average magnitude of AE events reduces gradually with strain in the hydrogen-free sample, whereas relatively steady AE fluctuations are observed during uniform elongation prior to fracture in the hydrogen-charged sample.

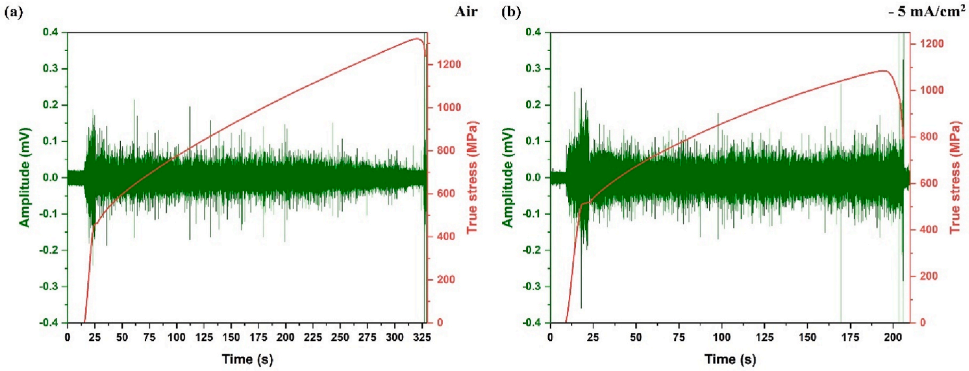

Fig. 5. AE streams collected during the tensile tests: (a) air (hydrogen-free), (b) hydrogen-charged −5 mA/cm^2.

3.3.2. AE parameters and slip-related information

The local stress relaxation processes related to the dislocation motion, pinning and unpinning from obstacles, and annihilation are considered to be primary sources of AE. Dislocation interactions with arbitrarily distributed obstacles of varying strength result in fluctuating local stress drops, giving rise to the random AE time series $U(t)$. As has been conceptually proposed in Refs. [47,48], the random AE process can be expressed by the first-order auto-regressive relaxation process of the Ornstein-Uhlenbeck type, which obeys the following stochastic equation

$$\frac{dU}{dt} = -U\Big/\tau_r + \tilde{\varepsilon} \qquad (3)$$

and which is entirely characterized by a single parameter – the characteristic relaxation time τ_r; $\tilde{\varepsilon}$ in the righthand side of Eq. (3) denotes the Gaussian noise acting as a stimulus. As a measure of temporal correlation between individual events in the time series, the relaxation time τ_r uniquely defines the autocorrelation function and, consequently, the power spectral density of the process (these quantities are interconnected by the Fourier transform according to the Wiener-Khintchine theorem). For the random process $U(t)$ governed by Eq. (3), the PSD takes a familiar Lorentz form

$$G(f) = 4\sigma_{UU}^2 \frac{f_0}{f_0^2 + 4\pi^2 f^2} \qquad (4)$$

where σ_{UU}^2 denotes the square variance of the random process, which serves as a measure of the power of $U(t)$, and the characteristic frequency $f_0 = 1/\tau_r$ is inversely related to the relaxation time in the system. Using Eq. (2), one can easily show that f_0 is simply related to the AE median frequency as $f_0 = 2\pi f_m$. Thus, the increase in the median frequency signifies the decrease in the correlation time in a set of AE events and vice versa – the decrease in f_m indicates the increase in the influence of past events on the present and future. AE power and median frequency are, in principle, mutually independent features characterizing the properties of power spectra [48,49].

In a simplistic way, the characteristic relaxation time in the ensemble of AE sources can be linked to the dislocation kinetics through the following relation [47]

$$\tau_r = <\mathrm{L}> / <\mathrm{v}> \qquad (5)$$

where $<\mathrm{L}>$ is the dislocation mean free path and $<\mathrm{v}>$ is the mean dislocation velocity. For virtually all conceivable dislocation configurations emerging in the course of plastic deformation, the mean distance that the dislocation segment travels before being anchored due to interactions with other stored dislocations can be inversely related to the total dislocation density ρ as [55,56]

$$<L> = 1\Big/\sqrt{\rho} \qquad (6)$$

Using Orowan's expression for the mean dislocation velocity

$$<\mathrm{v}> = \mathrm{M}\dot{\varepsilon}/\mathrm{b}\rho_m \qquad (7)$$

where M is the texture-dependent Taylor factor, $\dot{\varepsilon}$ is the plastic strain rate, b is the magnitude of the Burger's vector of a dislocation, and ρ_m is the density of mobile dislocations, the median frequency is expressed as

$$f_m \sim <v>\sqrt{\rho} = \frac{M\dot{\varepsilon}}{b\rho_m}\sqrt{\rho} = \frac{\sigma}{\rho_m}\dot{\varepsilon} \qquad (8)$$

Thus, the model predicts that as long as plastic deformation is macroscopically homogeneous, the linear relation between the AE median frequency and the true flow stress holds. The assumption on the uniformity of deformation resides in two terms - $\dot{\varepsilon}$ and ρ_m. As soon as strain localization of practically any kind occurs, local strain rate fluctuates and deviates from the mean value (in principle, $\dot{\varepsilon}$ cannot be scalar anymore and a tensorial notation should be used instead, see Ref. [57] for details on how this is implemented in the AE data processing). This is immediately reflected by the corresponding fluctuating behavior of the AE median frequency as has been convincing demonstrated in Ref. [54]. Similarly, the local mobile dislocation density can vary significantly as strain localization occurs.

3.3.3. AE activity during tensile test

Fig. 6 shows the AE spectral evolution (represented in terms of the AE power and median frequency) synchronized with the true stress-strain (logarithmic) data $\sigma(\varepsilon)$ and work hardening rate $\theta(\varepsilon)$ for hydrogen-free (air) and hydrogen-charged samples. From Fig. 6 it is evident that deformation commences almost immediately after the onset of loading for all samples. The occurrence of AE activity below the yield point, *i.e.*, in the micro-strain region, has been long recognized in many materials. Typically, in a polycrystalline material, the coarse grains with the favorable orientation tend to deform locally first before the entire volume becomes involved in the plastic flow, resulting in the acoustic emission signal at lower stresses.

3.3.3.1. AE time-history for hydrogen-free samples. For the hydrogen-free sample (Fig. 6a), the AE power peaks at the yield point and decays gradually with strain as deformation proceeds. The reduction in the AE power with strain is generally attributed to the shortening of the dislocation mean free path with the increasing dislocation density. The AE power then rises sharply again at fracture. Overall, this behavior is consistent with the results reported in abundant literature so far on a wide range on polycrystalline materials [48,58–61]. As has been shown

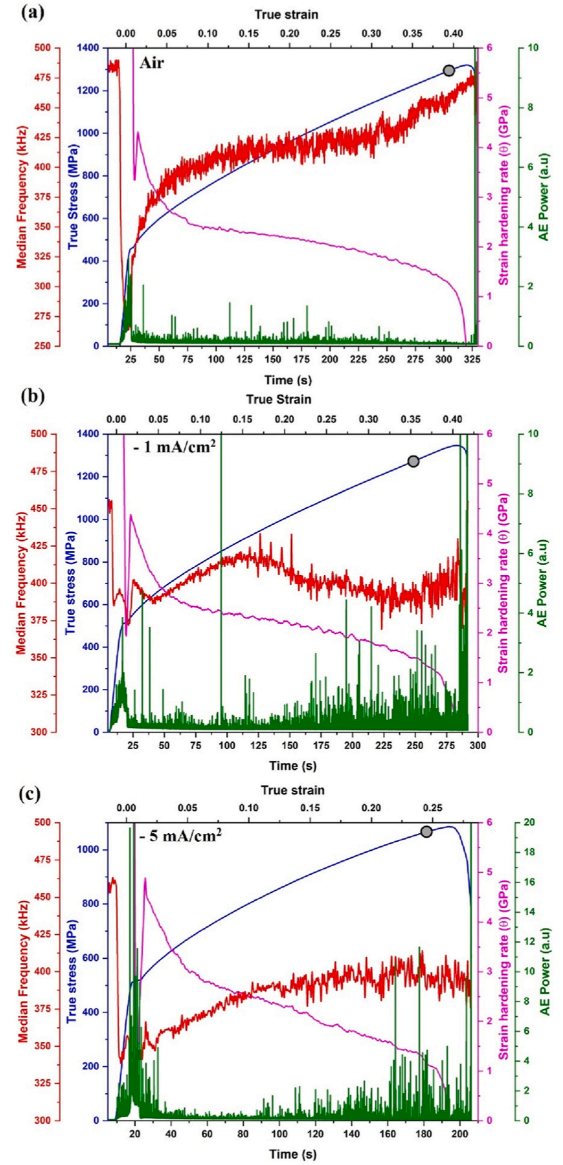

Fig. 6. AE time-history file. (a) Air. (b) -1 mA/cm^2 (c) -5 mA/cm^2 (the grey circle indicates the necking point according to the Considère criterion $\theta = \sigma$).

above, the Inconel 625 alloy exhibits a yield point phenomenon characteristic of the evolution of Lüders bands, where the collective movement of spatially grouped and temporarily correlated dislocations gives rise to the steep increase in the AE power and the concomitant fall in the AE median frequency [53].

The drop in the median frequency at the beginning of plastic deformation (Fig. 6a) is commonly observed in a wide range of FCC metals and alloys (see Ref. [54] for example) due to rapid generation and multiplication of mobile dislocations in conformity with the predictions following from Eq. (8). Beyond the yield point, *i.e.*, in the uniform elongation regime, the median frequency increases with strain. As has been discussed in the previous section, for material deforming predominantly by slip, the median frequency is inversely related to the dislocation mean free path. With increasing strain, the mean free path reduces since the density of forest dislocation increases, and thus, f_m can be directly related to the strain hardening behavior. The shift of the median frequency to the lower frequency domain can be indicative of plastic instability at necking due to the increasing temporal correlation [48] in the collective behavior of dislocations in the necked region. The local increase in the flow stress facilitates dislocation activity. This, in turn, stimulates dislocation storage and strain hardening escalating further the strain localization followed, finally, by the initiation of microcracks.

3.3.3.2. AE time-history for hydrogen-charged samples. For hydrogen-charged samples (Fig. 6b and c), one can notice that at the macroscopic yield point, the AE energy increases with hydrogen concentration. Unlike the uncharged sample, the profuse AE activity is observed in the uniform elongation regime of the hydrogen-charged samples, suggesting the additional AE source activation associated with the hydrogen influence. This result appears to be in fair agreement with several direct observations of enhanced dislocation mobility due to hydrogen in BCC (Iron) [62] and FCC (Nickel) [63] metals that is typically associated with signatures of the HELP mechanism.

In hydrogen-charged samples close to the yield point (Fig. 6b and c), the appreciable variation in the median frequency response is observed. Solute hydrogen acts as an obstacle to mobile dislocations at this stage, as is evident from the local increase in the median frequency in the pseudo-elastic regime. Moreover, at the mature uniform hardening stage, the median frequency for the hydrogen-charged samples exhibits significant fluctuations again, occurring concurrently with the intensive and highly fluctuative acoustic emission activity reflected in the AE power. Furthermore, an inflection point is seen in the overall f_m behavior at approximately the same deformation (~20% strain for -1 mA/cm^2 and ~12% for -5 mA/cm^2), where the median frequency starts to decrease with strain. Furthermore, such a behavior suggests that the additional source comes into stage, which is highly likely indicative of a crack. Besides, the shift in the median frequency to the lower range suggests that these cracks are of a ductile type, i.e., their nucleation and growth are mediated by cooperative dislocation-related plasticity.

3.3.4. *AE source identification and discrimination*

To identify and differentiate the AE sources during plastic deformation, the signal classification with respect to the shape of the PSD is performed using the hierarchical ASK algorithm proposed and described in detail in Ref. [45]. PSD is a “fingerprint” of the random AE source, and each mechanism differs by the dynamics of the local stress relaxation, which in turn generates distinct elastic waveforms with the correspondingly distinct PSD shape and amplitude at the sensor location, as has been fundamentally shown by Scruby et al. in the elasto-dynamic source modelling approach [64] (see also [60] for a practical example the ASK implementation of AE source discrimination). Fig. 7a and b shows the average power spectra (cluster centroid) for each specific AE source for hydrogen-free and hydrogen-charged sample (-1 mA/cm^2), respectively.

For both cases, the ASK algorithm discriminates between the three sources (excluding noise; note that the number of clusters/sources to be derived is not set a priory and is data-driven) featured by the statistically different shape of the normalized to unity PSD function $G(f)$.

AE power vs median frequency distributions for the hydrogen-free (air) and hydrogen-charged samples are shown in Fig. 7c and d, respectively. For the hydrogen-free sample, Fig. 7c illustrates two distinct sources mechanisms different from the background electronic noise according to the data distribution in the $P_{AE} - f_m$ space. We should reiterate that the AE sources have been identified by the statistical pairwise PSD comparison and Fig. 7c and d is used for illustrative

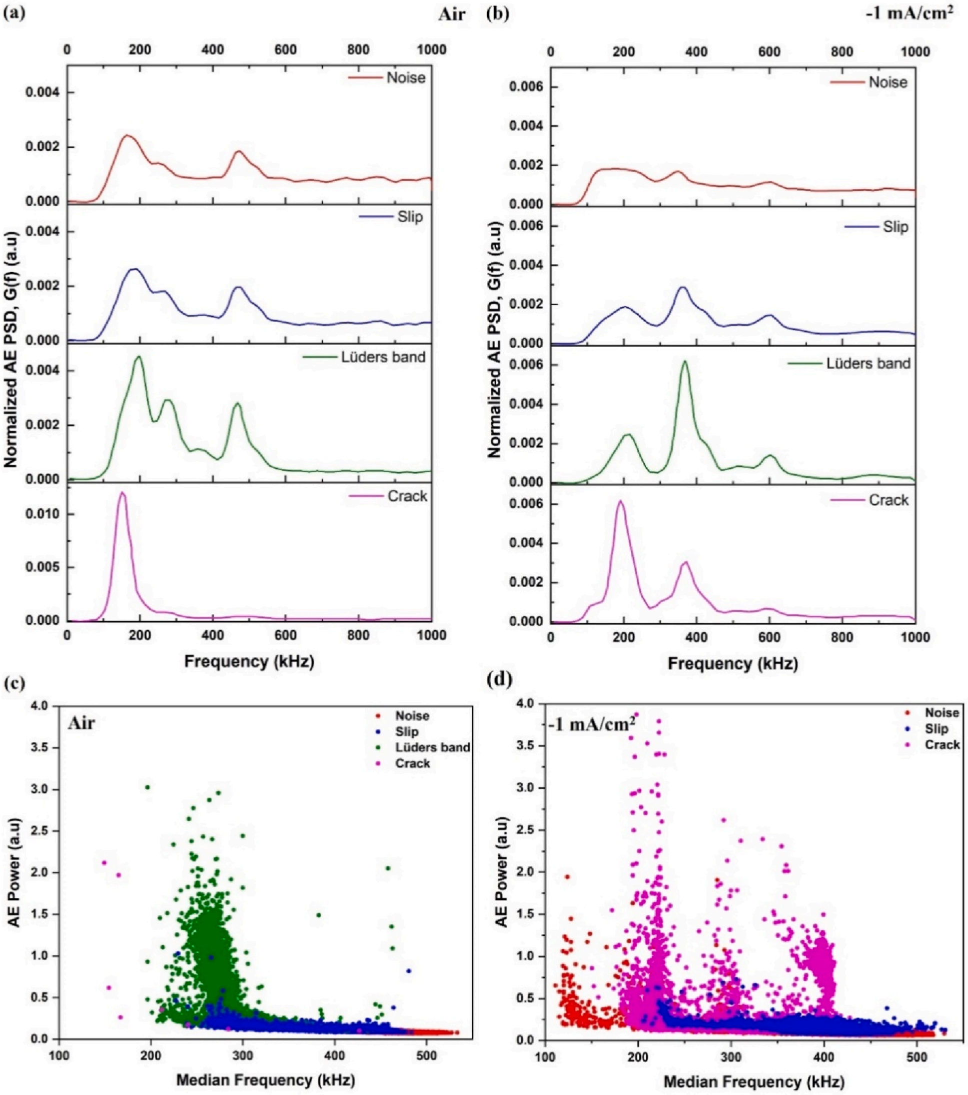

Fig. 7. Normalized PSD: (a) hydrogen-free (air) and (b) hydrogen-charged at −1 mA/cm^2. Scatterplot of AE power vs median frequency: (c) hydrogen-free (air) and (d) hydrogen-charged at −1 mA/cm^2.

purposes only.

The laboratory noise is characterized by the low energy and stationary wideband frequency distribution with a large fraction of high-frequency components (marked in red). The dislocation slip clusters evolve from the lower-frequency – higher-energy (power) domain at the onset of yielding to the higher-frequency – lower energy (power) domain as the strain hardening proceeds. Therefore, the dislocation slip-related clusters commonly have a 'banana-shape' that is seen for the cluster marked in blue. The collective dislocation behavior within a Lüders band generates high-energy components in the narrow low-frequency range at the lower end of the frequency spectrum (marked in green). Evidently, the energy associated with the localized Lüders band is higher than that for the uniform dislocation slip.

Fig. 7d shows a similar bivariant plot for the hydrogen-charged sample (−1 mA/cm^2). The additional source could be identified and associated with the cracks resulting from HE. These cracks are characterized by relatively high AE power and are dominant at the lower frequency domain. One can notice that the essential AE features attributed to the crack resemble those observed at the Lüders stage: the energy signatures of these two clusters are similar or overlapping with each other.

3.3.5. *Kinetics of source evolution*

For each AE realization of 1 ms duration, a deformation source is assigned based on the shape of the PSD, from which the behavior of individual sources can be traced on a greater time scale. Fig. 8 displays the kinetics of individual source mechanisms represented by the cumulative AE power evolution synchronized with the true stress-

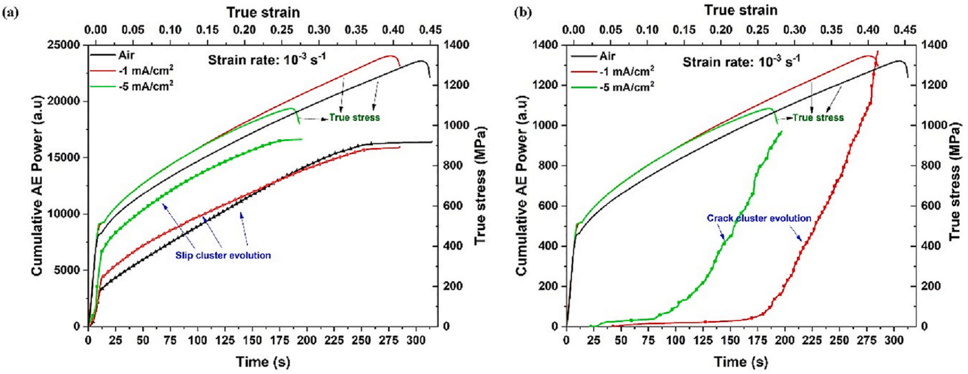

Fig. 8. Evolution of AE clusters for different samples: (a) dislocation slip and (b) microcracking due to HE.

logarithmic strain diagram. In the present study, two dominant sources – dislocation slip, and crack are compared. Let us notice that the AE signal clusterization algorithm ASK [45] used in the present work has been proven capable of distinguishing the twinning and dislocation slip modes coexisting during plastic deformation of steels with low SFE steels [59,60,65], Mg-based alloys [66,67], and near-γ Ti–Al super-alloys [68]. However, in the present work, there is no evidence in the AE streams to suggest an appreciable contribution from deformation twinning in either uncharged or H-charged samples. The reason for this behavior is that the SFE of the Nickel alloy is relatively large and hydrogen charging conditions employed in the current study might not be enough to trigger twinning. Fig. 8a displays the evolution of the slip cluster for both hydrogen-free and hydrogen-charged samples. Note that the slip cluster here encompasses the data points from both initial Lüders bands and dislocation slip. As follows from Eq. (4) and will be shown explicitly in what follows, the AE power serves as a direct measure of the dislocation activity during plastic deformation and strain hardening. Fig. 8a unveils that the accumulation of the AE power (or energy) occurs in parallel with the flow stress. Besides, the same figure demonstrates the progressive increase in the cumulative AE power of slip clusters with hydrogen concentration, which is again in harmony with the above-cited observations by Birnbaum et al. [62,63]. This hydrogen-influenced slip behavior is further discussed in section 4.2.

The microcrack evolution during the tensile test for the hydrogen-charged sample is visualized in Fig. 8b. Note that no significant crack-related AE activity has been observed in hydrogen-free specimens. For the sample charged at -1 mA/cm^2 current density, the evidence of crack initiation could be observed as early as at 5.4% true strain, and for -5 mA/cm^2, it is 3.2%, thus indicating that the threshold, if exists, for H-affected first crack nucleation is quite low. The kinetics of crack accumulation revealed by the AE signal is substantially different from dislocation slip, c. f. Fig. 8a and b. The evolution of the crack-related AE cluster in hydrogen-charged samples exhibits three distinct stages: (i) the incubation period characterized by the strain/stress required to initiate the first crack, (ii) the nucleation stage is featured by the linear (on time or strain) accumulation of small "non-propagating" cracks along the gauge surface, (iii) the crack propagation stage is highlighted by the rapid exponential-like growth of the cumulative crack length reflected in the cumulative AE power. The occurrence of similar stages of damage evolution was plausibly proposed earlier for the hydrogen-charged dual phase steel [35] and Nickel alloy [31], where the crack area was measured as a function of plastic strain. However, no quantitative description of the damage propagation and the conditions for the transitions between different stages of damage evolution have been reported so far to the best of our knowledge. In this regard, the AE technique demonstrates high potential to promote the further in-depth development of the topic as only a limited number of in situ techniques can be used to this end. The AE clearly shows that the duration of each stage varies with the applied charging potential. For instance, as it could be reasonably expected, incubation stage (i) associated with the strain required for crack initiation reduces with the increase in charging severity. At stage (ii), the total AE power increase is sluggish and linear in strain. It extends up to $\varepsilon = 23\%$ at -1 mA/cm^2 and 12.5% at -5 mA/cm^2 charging current density, approximately, as can be derived from Fig. 8b by the intersection of interpolated branches of the cumulative AE power plots. The duration of stage (ii) is longer for -1 mA/cm^2 when compared to -5 mA/cm^2. The crack growth on stage (iii) occurs at approximately the same rate for both charging conditions (the cumulative P_{AE} plots are parallel to each other in Fig. 8b).

3.4. Characterization of hydrogen-assisted cracks

The tensile test interrupted at an engineering strain of 7% was performed to examine the early stage of crack initiation in the hydrogen-charged sample (-5 mA/cm^2). The microstructure at the side surface is shown in Fig. 9. At the surface, most cracks are of the transgranular type (Fig. 9a). From the BSE images shown in Fig. 9d, these cracks were found to be initiated and propagating along the slip band intersections, and the crack path follows the {111} plane trace (red dash line in the slip traces in Fig. 9a). A small fraction of annealing twin boundaries participates in the cracking process; more evidence is observed in Fig. 9a for crack deflections [69]. The slip line intersections act as stress risers, which attract hydrogen, thereby facilitating the nanovoids formation. Furthermore, the reduction in SFE due to the presence of hydrogen promotes slip planarity and enhances the stress concentration at the intersections of {111} slip planes, resulting in hydrogen-induced cracking along the dislocation slip bands [30].

The cross-sectional microstructure (Fig. 10) reveals the average crack penetration depth of 130 μm with approximately equal fractions of intergranular and transgranular cracks. To quantify the crack type as a function of depth, the misorientation profile across the grain adjacent to the crack was obtained for 10 typical cracks (The IPF map of few such cracks are included in the Supplymentary material Fig. 4), and the bar chart in Fig. 10c represents the crack type (transgranular or intergranular) as a function of depth. At the shallow depth of 60 μm from the surface, both intergranular and transgranular crack types are observed. However, the number fraction of transgranular cracks prevails in this region. Deeper inside, the cracks are predominately intergranular and propagate along the general high-angle grain boundaries. This observation suggests that there is a transition from the transgranular crack mode to the intergranular type. In the present study, there is no sufficient evidence to suggest that the discrete grain boundary carbide

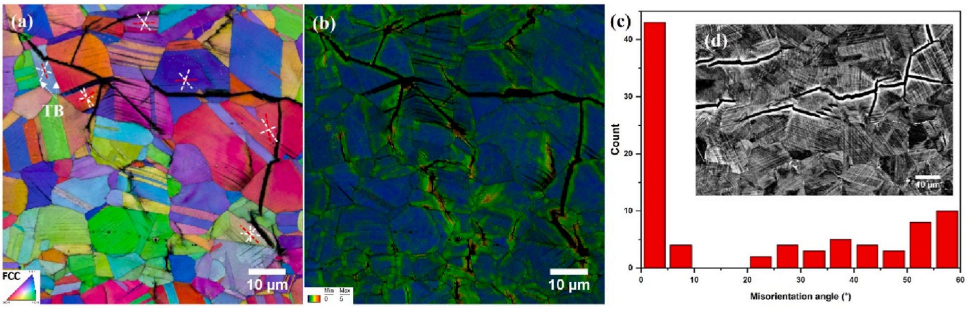

Fig. 9. Surface secondary crack microstructure of the deformed sample from the interrupted tensile test (7% strain, −5 mA/cm2 charging): (a) IPF map. (b) Kernel average misorientation (KAM) map. (c) Misorientation information of surface cracks. (d) BSE image. (TB: Twin boundary).

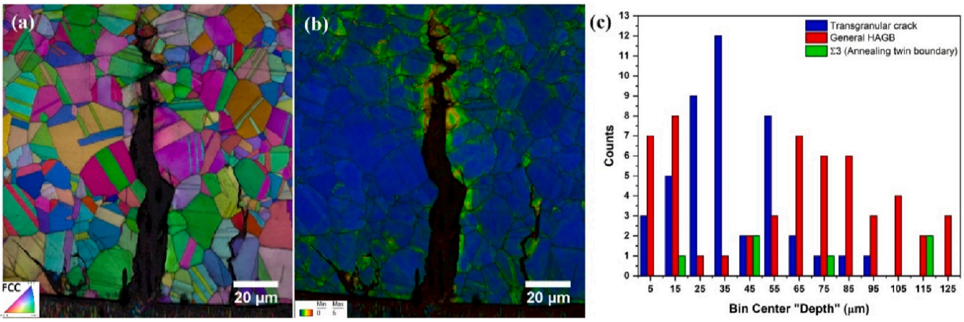

Fig. 10. Cross-sectional microstructure of the deformed sample from the interrupted tensile test (7% strain, −5 mA/cm^2 charging): (a) IPF map, (b) KAM map and (c) crack type as a function of depth.

precipitates play a significant role in HE. The kernel average misorientation (KAM) map at the surface and the cross-section shows high strain gradients along the crack path, indicating strain localization and dislocation activity close to the crack. This strongly suggests that these cracks are of a ductile type, i.e., they have been formed via a plasticity-mediated mechanism.

4. Discussion

4.1. Hydrogen charging-induced deformation

In the present work, hydrogen charging-induced deformation was observed (Fig. 2a). The slip line formation during charging has been reported for different FCC alloys, *e.g.*, for the CoCrFeMnNi high-entropy alloy and Ni-based alloy 718 and 625 [4,16,21]. The inherent slow diffusivity and high hydrogen solubility suggest that there is a steep concentration gradient prevailing in the sample. The hydrogen distribution profile $C_{(x,t)}$ for the present work is estimated using a thick plate diffusion model [70]

$$\frac{C_{(x,t)}}{C_s} = 1 - erf\left(\frac{x}{\sqrt{4Dt}}\right) \quad 0 < x < l \tag{9}$$

$$\mathrm{erf}(u) = \frac{2}{\pi}\int_0^u \exp\left(-u^2\right)du \tag{10}$$

where C_s is the surface hydrogen concentration, D is the diffusion coefficient (5.56×10^{-15} m^2/s [50]), and t is the duration of charging (24 h). Fig. 12a shows that the hydrogen concentration profile decreases exponentially with depth; so do the hydrogen-induced defects. The non-uniform defect distribution necessitates a technique like XRD, which could characterize the near-surface damages. The asymmetric shape of the XRD peak measured immediately after charging and the recovery of the peak intensity after a day confirm the existence of high elastic strains generated during charging (Fig. 2). The internal stress (σ) generated during charging was estimated using the following relation

$$\sigma = B\,\frac{\Delta V}{V_0} = B \times 3 \times \frac{\Delta a}{a_0} = 460\ MPa \tag{11}$$

where B is the bulk modulus of the material ($B = 180$ GPa) [4], $\frac{\Delta a}{a_0}$ is the relative lattice parameter change due to the dissolved hydrogen solute. The volume expansion due to the lattice parameter change during charging generates the internal stress which is larger than the yield strength of the material (450 MPa), resulting in the slip line formation after charging at zero external loads.

Hydrogen in the interstitial solid solution in Nickel produces a hydrostatic lattice distortion [71]. Once the stress level reaches the critical resolved shear stress value (147 MPa, deduced from the polycrystalline yield stress of the uncharged sample and accounting for the Taylor orientation factor), the dislocations are generated to accommodate the strain. Furthermore, within the Defactant model framework, the presence of hydrogen could accelerate the generation process by reducing the dislocation line energy [18]. Increased hydrogen uptake (Table 2) at high current density is due to the deformation microstructure promoting more hydrogen ingress.

Hydrogen charging results in the peak shift and broadening of the XRD spectra (Fig. 2). Similar behavior has been reported for austenitic stainless steel and Nickel alloys. Charging at high hydrogen fugacity results in the stress-induced phase transformation to martensite in austenitic stainless steel [72,73], whereas in Nickel alloys, hydrides are reported to form [15,19,20]. Hydrogen atoms occupy the octahedral sites in Nickel, which assumes the FCC β-hydride (NiH_x), when hydrogen concentration is high ($x > 0.6$). In this work, the ratio of hydrogen atom to metal atom for high current density sample (- 10 mA/cm^2) is 0.07, in addition, no distinct hydride XRD peaks were observed right after charging, thus the hydride role on embrittlement behavior can be disregarded. The broadening of peak after room temperature aging (24 h) is due to hydrogen charging-induced defects such as dislocations and abundant vacancies [15].

4.2. Hydrogen-enhanced hardening

In the current study, the overall hydrogen-enhanced hardening response was observed. The hydrogen-induced hardening effect is shown to dominate at high strain rate testing of pure Nickel and its alloy variants [5,12,71]. The plastic flow behavior of FCC materials is governed by the collective movement of dislocations and their interactions, with the total dislocation density serving as a chief internal variable used to explain the strain hardening behavior [56,74]. These dislocations can be subdivided into two populations: mobile dislocations, which transmit plastic strains by moving across the crystal, and statistically stored dislocations, which are immobile and act as obstacles to moving dislocations (note that this subdivision is conventional since the mobile dislocation can be blocked and get immobilized by many obstacles such as point defects, other dislocations and grain boundaries, whereas immobile dislocations, in turn, can be unpinned from their anchors and take part in plastic deformation). In this section, the hydrogen effect on both of these variables is discussed in detail.

During the uniform hardening stage, it is assumed that the mobile dislocation density remains constant if the deformation is uniform (during the constant strain rate test). From the elementary dislocation theory assuming that the AE energy is dissipated as a result of the dislocation motion under the action of Peach-Köhler force, Vinogradov et al. [58] have proposed a phenomenological model for the AE power P_{AE} in relation to the strain hardening parameters as

$$P_{AE} = K_{AE}\rho_m \frac{\dot{\sigma}}{\sigma} = K_{AE}\rho_m \frac{\Theta}{\sigma}\dot{\varepsilon} \tag{12}$$

where K_{AE} is the phenomenological factor incorporating the AE transfer function coefficient, Θ is the strain hardening rate. This expression predicts that a linear relationship exists between the AE power and the $\frac{\dot{\sigma}}{\sigma}$ or $\frac{\Theta}{\sigma}$ ratio, which has been verified for Cu in Ref. [58] and recently for Cu–Zn alloys with a wide range of stacking fault energies [54]. The slope of the plot P_{AE} *vs* $\frac{\Theta}{\sigma}$ is simply proportional to the mobile dislocation density ρ_m for a given constant strain rate. The plot in Fig. 11a clearly indicates that the mobile dislocation density increases with the hydrogen concentration (larger slope with higher hydrogen concentration). The result is consistent with the in-situ nanoindentation study of the same alloy [16], where the activation energy for dislocation nucleation is reduced in the hydrogen environment. In the bulk scale, the presence of atomic hydrogen in the Nickel lattice would increase the population of mobile dislocations by reducing the critical stress for the Frank-Read source activation and loop expansion [5,12,75].

The average velocity of dislocations can be estimated from Orowan's expression (Eq. (7)). The ratio of the average velocity in hydrogen to that in air for two different charging conditions is evaluated as $v_{H(-1\ mA/cm^2)}/v_{air} = 0.5$ and $v_{H(-5\ mA/cm^2)}/v_{air} = 0.3$, respectively. Thus, with the increase in the hydrogen concentration, the average velocity of dislocations (it should not be confused with the instantaneous velocity) tends to reduce. This observation supports the hypothesis that hydrogen causing solute pinning of dislocations and increasing the friction stress is the dominant mechanism, resulting in the enhanced hardening [76–78]; break away from solute pinning is reflected in the enhanced AE power response (Figs. 6 and 8a).

The stored dislocation density can be regarded as a key indicator of the dislocation/microstructure evolution over the course of plastic deformation [74,79]. Fig. 11b shows the Kocks-Mecking plot for hydrogen-free and hydrogen-charged Inconel 625. One can notice that for a given stress, the stored dislocation density is increased with hydrogen content; besides, there is a noticeable difference in the different stages of the work hardening behavior in differently charged samples. The hydrogen-affected plastic flow behavior has been reported for many alloy systems, wherein the density of dislocation was shown to increase in the deformed microstructure [5,35,36]. Similarly, the TEM observation of the deformed Ni single crystal unveiled the equiaxed dislocation cells, whereas the hydrogenated Ni sample at the same strain displayed a distinct planar microstructure [5]. This was explained primarily due to the effect of hydrogen increasing the work for partial recombination and limiting the probability of cross-slip. Furthermore, nanoindentation results on the same alloy exhibited an increased strain hardening response during in-situ hydrogen charging [16].

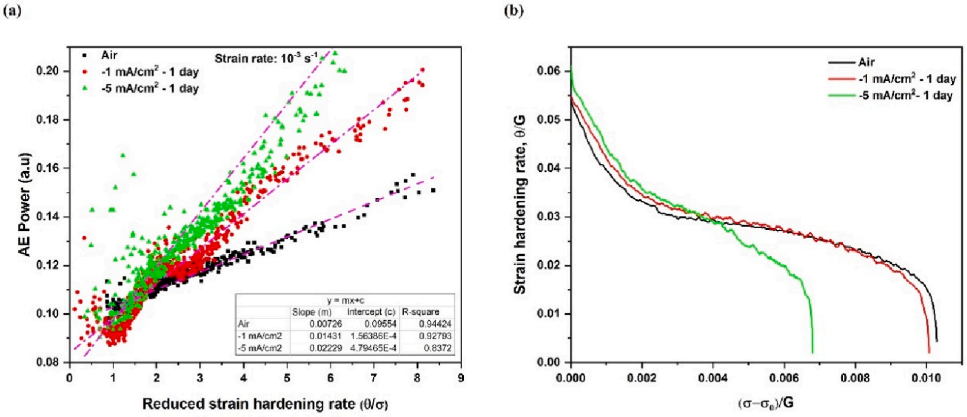

y = mx+c

	Slope (m)	Intercept (c)	R-square
Air	0.00726	0.09554	0.94424
-1 mA/cm2	0.01431	1.56386E-4	0.92793
-5 mA/cm2	0.02229	4.79465E-4	0.8372

Fig. 11. (a) AE Power in relation to the reduced strain hardening rate $\frac{\Theta}{\sigma}$; note the good linear approximation of the data during the entire uniform elongation stage (Linear regression fitting shown by pink line to highlight the linearity). (b) Kocks-Mecking plot showing normalized strain hardening rate vs normalized true stress. (For interpretation of the references to colour in this figure legend, the reader is referred to the Web version of this article.)

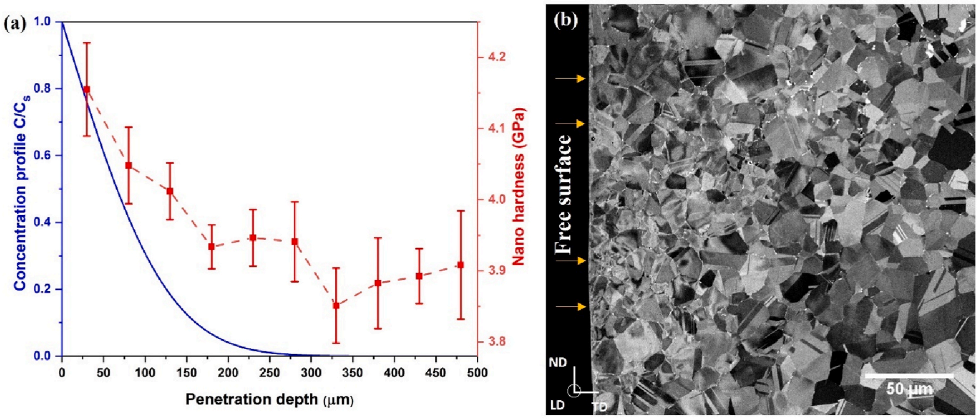

Fig. 12. (a) Hydrogen diffusion profile and nano hardness data. (b) Cross-section of hydrogen charged sample (-5 mA/cm^2) without any mechanical loading (arrows point to a free surface corresponding to hydrogen charging front).

4.3. Hydrogen-assisted cracks

The stacking fault energy of Inconel 625 is approximately 60 mJ/m^2, and the material deforms predominantly by wavy slip [80]. During tensile testing of the uncharged sample, the AE energy rises and the median frequency drops at the onset of yielding due to the dislocation multiplication process. During the uniform strain hardening stage, the mean free path for dislocations reduces, which is accompanied by the increased median frequency response and the gradual decay in the AE power (energy) with strain.

Thus, during tensile testing of hydrogen-charged samples, in addition to the growing average dislocation density governing the strain hardening, another process takes place, which facilitates local structural rearrangements reflected in the AE signal. According to the interpretation of the AE suggested above, the median frequency is fundamentally linked to the correlation (relaxation) time between the successive events in the random time series: while the increase in the f_m value corresponds to the shortening of the dislocation mean free path with increasing ρ, the decrease in f_m implies that there is an alternative process of structural relaxation featured by the increasing correlation time [47,48]. In other words, the longer relaxation time reflected in the AE - f_m behavior assumes that a process of structural rearrangements occurring on a larger scale comes into play, and it is plausible to associate this process with hydrogen-assisted microcracks observed in the present work.

Though the crack initiation strain is about 5.4% for -1 mA/cm^2 and 3.2% for -5 mA/cm^2 charging conditions, the intense AE activity or change in the median frequency response from the "ideal" model-predicted behavior $f_m \sim \sigma$, Eq. (8), could only be observed after the true strain of 23% for -1 mA/cm^2 and 12.5% for -5 mA/cm^2, respectively (Fig. 6b and c). As has been noticed in Section 3.3.5, the crack cluster evolution for hydrogen-charged samples exhibits three stages, and during the second stage (ii), the cracks randomly nucleate throughout the gauge part. Correspondingly, the cumulative AE power for this cluster shows a steady (nearly linear) yet only sluggish increase at this stage. Once the crack is nucleated, it will dominate a stress distribution so that AE will predominantly be produced by the crack-related processes, including the emission of dislocations from the crack tip, crack growth, *etc*. Detailed microstructural characterization at different stages of crack evolution will be published elsewhere. The AE method is not capable of differentiating between intergranular and transgranular cracks in the present settings because both type of cracks are generated in a ductile manner through the dislocation-mediated processes, as is evident from the KAM maps (Figs. 9b and 10b).

To investigate the depth-dependent crack transition from the transgranular to intergranular type (Fig. 10), the cross-section microstructure of the sample charged at -5 mA/cm^2 is examined without any mechanical loading (Fig. 12). The BSE image unveils extensive plastic deformation in the surface layer of down to 80 μm from the free surface. Furthermore, the nanohardness measured through the thickness of the material shows the increased hardness response at the surface, suggesting that charging has induced irrecoverable plastic strains with a strong gradient in the surface region. The depth-dependent crack transition can be attributed to the hydrogen concentration profile and prior deformation. At a shallow depth of 60 μm from the surface, where the extensive prior deformation had been induced during charging, the transgranular cracks prevail over the intergranular ones. The charging-induced deformation promotes preferential hydrogen segregation at the highly stressed regions, for instance, at the slip band intersections. During loading, the nanovoid nucleation along these bands generates a micro-crack [3].

Intergranular cracks are dominant at the interior part of the sample. At the region close to the free surface, the dislocations, which have been produced during charging, store and transmit hydrogen, thus making the cracking along the slip band intersection more favorable. However, at the regions deep in the sample, plastic deformation becomes negligible. To nucleate a crack inside the grain, the dislocations have to be generated first, and hydrogen has to be transported to the slip band intersection. Therefore, grain boundaries representing the hydrogen trap sites in the absence of plastic strain become the preferred sites for crack initiation and growth [31,81]. Thus, the competition between hydrogen availability and transport determines the crack mode.

5. Conclusions

Hydrogen embrittlement susceptibility of the Nickel-based alloy Inconel 625 was investigated using a tensile test instrumented with the in-situ acoustic emission (AE) monitoring technique aiming at unveiling fine temporal details of the evolution of the dislocation ensembles and hydrogen-assisted microcracking in differently charged samples. Using the spectral analysis of AE signals coupled with the non-supervised clustering procedure, the contribution of the dislocation slip and microcracks into the deformation and fracture processes has been separated and followed individually as strain hardening proceeds. Advanced characterization tools were used to study the charging-induced deformation and hydrogen-assisted cracking. The major findings can be summarized as follows.

- Electrochemical hydrogen charging-induced deformation was quantified using the XRD technique. Hydrogen supersaturation and sluggish diffusion generate internal stresses, which, if exceed the critical resolved shear stress for dislocation initiation, is the root cause of the slip lines observed on the free surface of charged samples.
- The hydrogen-enhanced slip behavior is evident from the AE analysis. The higher AE power in the hydrogen-charged samples is related to the increased dislocation activity. Using the phenomenological relation between the AE power and the slip behavior, the relative mobile dislocation density is estimated, and it is found to increase with the hydrogen concentration. Concomitantly, the average dislocation velocity in the hydrogen-charged samples is reduced. This observation suggests that solute pinning of dislocations by hydrogen is the dominant mechanism increasing the lattice friction and resulting in hydrogen-related hardening.
- The hydrogen-assisted crack nucleation and propagation process can be reliably identified from the AE spectral-based cluster analysis. Three stages of the damage evolution process – incubation, “slow” accumulation of surface cracks and accelerated crack growth - are observed in the hydrogen-charged samples before macroscopic strain localization sets in. The kinetic details of each stage been unveiled and shown that the duration of each stage varies with the severity of charging. The AE power spectral density attributed to hydrogen cracks is featured by the dominant low-frequency components indicating that these cracks are of a ductile type.
- The statistical crack analysis of the surface morphology reveals the transition from the transgranular to the intergranular fracture type. The competition between these two modes is explained by the estimated hydrogen concentration profile depending on the loading conditions. At the shallow depth of 60 μm, the pre-damage induced during charging and hydrogen accumulation at the slip band intersections provides an easy path for the transgranular cracking along dislocation slip bands. In the bulk of the sample without any prior deformation, the additional energy is needed to generate a dislocation and promote hydrogen transport to the intersections. Since the grain boundaries are strong trap sites for hydrogen, it is easier to nucleate a crack along grain boundaries by decohesion rather than generating a transgranular crack.

CRediT authorship contribution statement

Chandrahaasan K. Soundararajan: Conceptualization, Methodology, Investigation, Writing – original draft, Writing – review & editing. **Aleksander Myhre:** Methodology, Writing – review & editing. **Aleksander Sendrowicz:** Methodology, Writing – review & editing. **Xu Lu:** Methodology, Writing – review & editing. **Alexey Vinogradov:** Supervision, Investigation, Writing – original draft, Writing – review & editing.

Declaration of competing interest

The authors declare that they have no known competing financial interests or personal relationships that could have appeared to influence the work reported in this paper.

Data availability

The data required to reproduce these findings cannot be shared at this time as this data also forms part of an ongoing study.

Acknowledgements

This work was supported by the Research Council of Norway and industries through the projects M-HEAT (294689). We are grateful to Dr. Dong Wang and Dr. Di Wan for providing valuable comments regarding the manuscript.

Appendix A. Supplementary data

Supplementary data to this article can be found online at https://doi.org/10.1016/j.msea.2023.144635.

References

[1] M.B. Djukic, G.M. Bakic, V. Sijacki Zeravcic, A. Sedmak, B. Rajicic, The synergistic action and interplay of hydrogen embrittlement mechanisms in steels and iron: localized plasticity and decohesion, Eng. Fract. Mech. 216 (2019), 106528, https://doi.org/10.1016/J.ENGFRACMECH.2019.106528.

[2] H.K. Birnbaum, P. Sofronis, Hydrogen-enhanced localized plasticity—a mechanism for hydrogen-related fracture, Mater. Sci. Eng. A 176 (1994) 191–202, https://doi.org/10.1016/0921-5093(94)90975-X.

[3] Z. Tarzimoghadam, D. Ponge, J. Klöwer, D. Raabe, Hydrogen-assisted failure in Ni-based superalloy 718 studied under in situ hydrogen charging: the role of localized deformation in crack propagation, Acta Mater. 128 (2017) 365–374, https://doi.org/10.1016/j.actamat.2017.02.059.

[4] X. Lu, D. Wang, D. Wan, Z.B.B. Zhang, N. Kheradmand, A. Barnoush, Effect of electrochemical charging on the hydrogen embrittlement susceptibility of alloy 718, Acta Mater. 179 (2019) 36–48, https://doi.org/10.1016/j.actamat.2019.08.020.

[5] D. Delafosse, Hydrogen effects on the plasticity of face centred cubic (fcc) crystals, in: Gaseous Hydrogen Embrittlement of Materials in Energy Technologies, Elsevier, 2012, pp. 247–285, https://doi.org/10.1533/9780857095374.2.247.

[6] R.A. Oriani, Whitney award lecture—1987: hydrogen—the versatile embrittler, Corrosion 43 (1987) 390–397, https://doi.org/10.5006/1.3583875.

[7] Y. Liang, P. Sofronis, Toward a phenomenological description of hydrogen-induced decohesion at particle/matrix interfaces, J. Mech. Phys. Solid. 51 (2003) 1509–1531, https://doi.org/10.1016/S0022-5096(03)00052-8.

[8] S.P. Lynch, Hydrogen embrittlement (HE) phenomena and mechanisms, in: Stress Corrosion Cracking, Elsevier, 2011, pp. 90–130, https://doi.org/10.1533/9780857093769.1.90.

[9] S.P. Lynch, A fractographic study of hydrogen-assisted cracking and liquid-metal embrittlement in nickel, J. Mater. Sci. 21 (2) (1986) 692–704, https://doi.org/10.1007/BF01145543, 21 (1986).

[10] S.P. Lynch, Environmentally assisted cracking: overview of evidence for an adsorption-induced localised-slip process, Acta Metall. 36 (1988) 2639–2661, https://doi.org/10.1016/0001-6160(88)90113-7.

[11] K. Takai, H. Shoda, H. Suzuki, M. Nagumo, Lattice defects dominating hydrogen-related failure of metals, Acta Mater. 56 (2008) 5158–5167, https://doi.org/10.1016/j.actamat.2008.06.031.

[12] S.K. Lawrence, Y. Yagodzinskyy, H. Hänninen, E. Korhonen, F. Tuomisto, Z. D. Harris, B.P. Somerday, Effects of grain size and deformation temperature on hydrogen-enhanced vacancy formation in Ni alloys, Acta Mater. 128 (2017) 218–226, https://doi.org/10.1016/j.actamat.2017.02.016.

[13] Y. Fukai, Y. Shizuku, Y. Kurokawa, Superabundant vacancy formation in Ni–H alloys, J. Alloys Compd. 329 (2001) 195–201, https://doi.org/10.1016/S0925-8388(01)01603-6.

[14] Y. Ding, H. Yu, M. Lin, K. Zhao, S. Xiao, A. Vinogradov, L. Qiao, M. Ortiz, J. He, Z. Zhang, Hydrogen-enhanced grain boundary vacancy stockpiling causes transgranular to intergranular fracture transition, Acta Mater. 239 (2022), 118279, https://doi.org/10.1016/J.ACTAMAT.2022.118279.

[15] L. Chiari, K. Kojima, Y. Endo, H. Teshigahara, M. Butterling, M.O. Liedke, E. Hirschmann, A.G. Attallah, A. Wagner, M. Fujinami, Formation and time dynamics of hydrogen-induced vacancies in nickel, Acta Mater. 219 (2021), 117264, https://doi.org/10.1016/J.ACTAMAT.2021.117264.

[16] Chandrahaasan K. Soundararajan, Dong Wang, Alexey Vinogradov, Effect of Hydrogen on Nanomechanical Properties of Inconel 625 Studied Using In-Situ Electrochemical Nanoindentation Technique (under review), (n.d.).

[17] A. Barnoush, H. Vehoff, Recent developments in the study of hydrogen embrittlement: hydrogen effect on dislocation nucleation, Acta Mater. 58 (2010) 5274–5285, https://doi.org/10.1016/j.actamat.2010.05.057.

[18] R. Kirchheim, Reducing grain boundary, dislocation line and vacancy formation energies by solute segregationII. Experimental evidence and consequences, Acta Mater. 55 (2007) 5139–5148, https://doi.org/10.1016/j.actamat.2007.05.033.

[19] H. Hagi, Y. Hayashi, hydride formation in the surface layer of nickel and nickel-iron alloys by cathodic polarization, Nippon Kinzoku Gakkai-Si 51 (1987) 797–803, https://doi.org/10.2320/JINSTMET1952.51.9_797.

[20] R. Juškenas, A. Selskis, V. Kadziauskiene, In situ X-ray diffraction investigation of nickel hydride formation during cathodic charging of Ni, Electrochim. Acta 43 (1998) 1903–1911, https://doi.org/10.1016/S0013-4686(97)00304-6.

[21] D. Wang, X. Lu, Y. Deng, D. Wan, Z. Li, A. Barnoush, Effect of hydrogen-induced surface steps on the nanomechanical behavior of a CoCrFeMnNi high-entropy alloy revealed by in-situ electrochemical nanoindentation, Intermetallics 114 (2019), 106605, https://doi.org/10.1016/j.intermet.2019.106605.

[22] A. Barnoush, H. Vehoff, Electrochemical nanoindentation: a new approach to probe hydrogen/deformation interaction, Scripta Mater. 55 (2006) 195–198, https://doi.org/10.1016/j.scriptamat.2006.03.041.

[23] P.J. Ferreira, I.M. Robertson, H.K. Birnbaum, Hydrogen effects on the character of dislocations in high-purity aluminum, Acta Mater. 47 (1999) 2991–2998, https://doi.org/10.1016/S1359-6454(99)00156-1.

[24] D. Wang, X. Lu, D. Wan, X. Guo, R. Johnsen, Effect of hydrogen on the embrittlement susceptibility of Fe–22Mn-0.6C TWIP steel revealed by in-situ tensile tests, Mater. Sci. Eng. 802 (2021), 140638, https://doi.org/10.1016/j.msea.2020.140638.

[25] D. Wan, Y. Deng, A. Barnoush, Hydrogen embrittlement effect observed by in-situ hydrogen plasma charging on a ferritic alloy, Scripta Mater. 151 (2018) 24–27, https://doi.org/10.1016/j.scriptamat.2018.03.038.

[26] E. Sirois, H.K. Birnbaum, Effects of hydrogen and carbon on thermally activated deformation in nickel, Acta Metall. Mater. 40 (1992) 1377–1385, https://doi.org/10.1016/0956-7151(92)90438-K.

[27] M. Iannuzzi, A. Barnoush, R. Johnsen, Materials and corrosion trends in offshore and subsea oil and gas production, Npj Mater. Degrad. 1 (2017) 1–11, https://doi.org/10.1038/s41529-017-0003-4.

[28] L.E. Shoemaker, Alloys 625 and 725: trends in properties and applications, in: Proceedings of the International Symposium on Superalloys and Various Derivatives, 2005, pp. 409–418, https://doi.org/10.7449/2005/superalloys_2005_409_418.

[29] J.J. Debarbadillo, S.K. Mannan, Alloy 718 for oilfield applications, JOM 64 (2012) 265–270, https://doi.org/10.1007/S11837-012-0238-Z.

[30] Z. Zhang, G. Obasi, R. Morana, M. Preuss, Hydrogen assisted crack initiation and propagation in a nickel-based superalloy, Acta Mater. 113 (2016) 272–283, https://doi.org/10.1016/j.actamat.2016.05.003.

[31] Z.D. Harris, S.K. Lawrence, D.L. Medlin, G. Guetard, J.T. Burns, B.P. Somerday, Elucidating the contribution of mobile hydrogen-deformation interactions to hydrogen-induced intergranular cracking in polycrystalline nickel, Acta Mater. 158 (2018) 180–192, https://doi.org/10.1016/j.actamat.2018.07.043.

[32] T. Hajilou, I. Taji, F. Christien, S. He, D. Scheiber, W. Ecker, R. Pippan, V. I. Razumovskiy, A. Barnoush, Hydrogen-enhanced intergranular failure of sulfur-doped nickel grain boundary: in situ electrochemical micro-cantilever bending vs. DFT, Mater. Sci. Eng. 794 (2020), 139967, https://doi.org/10.1016/j.msea.2020.139967.

[33] M. Koyama, H. Springer, S.v. Merzlikin, K. Tsuzaki, E. Akiyama, D. Raabe, Hydrogen embrittlement associated with strain localization in a precipitation-hardened Fe–Mn–Al–C light weight austenitic steel, Int. J. Hydrogen Energy 39 (2014) 4634–4646, https://doi.org/10.1016/J.IJHYDENE.2013.12.171.

[34] M.L.L. Martin, B.P.P. Somerday, R.O.O. Ritchie, P. Sofronis, I.M.M. Robertson, Hydrogen-induced intergranular failure in nickel revisited, Acta Mater. 60 (2012) 2739–2745, https://doi.org/10.1016/j.actamat.2012.01.040.

[35] M. Koyama, C.C. Tasan, E. Akiyama, K. Tsuzaki, D. Raabe, Hydrogen-assisted decohesion and localized plasticity in dual-phase steel, Acta Mater. 70 (2014) 174–187, https://doi.org/10.1016/j.actamat.2014.01.048.

[36] C.K. Soundararajan, H. Luo, D. Raabe, Z. Li, Hydrogen resistance of a 1 GPa strong equiatomic CoCrNi medium entropy alloy, Corrosion Sci. 167 (2020), 108510, https://doi.org/10.1016/j.corsci.2020.108510.

[37] C.R. Heiple, S.H. Carpenter, Acoustic emission produced by deformation of metals and alloys, J. Acoust. Emiss. 6 (1987) 177.

[38] E.D. Merson, P.N. Myagkikh, G.V. Klevtsov, D.L. Merson, A. Vinogradov, Effect of fracture mode on acoustic emission behavior in the hydrogen embrittled low-alloy steel, Eng. Fract. Mech. 210 (2019) 342–357, https://doi.org/10.1016/j.engfracmech.2018.05.026.

[39] E.D. Merson, P.N. Myagkikh, V.A. Poluyanov, D.L. Merson, A. Vinogradov, Features of the hydrogen-assisted cracking mechanism in the low-carbon steel at ex- and in-situ hydrogen charging, in: Procedia Structural Integrity, Elsevier B.V., 2018, pp. 1141–1147, https://doi.org/10.1016/j.prostr.2018.12.238.

[40] E.D. Merson, M.M. Krishtal, D.L. Merson, A.A. Eremichev, A. Vinogradov, Effect of strain rate on acoustic emission during hydrogen assisted cracking in high carbon steel, Mater. Sci. Eng. 550 (2012) 408–417, https://doi.org/10.1016/j.msea.2012.04.094.

[41] D.D. Dedhia, W.E. Wood, Application of acoustic emission analysis to hydrogen-assisted cracking, Mater. Sci. Eng. 49 (1981) 263–273, https://doi.org/10.1016/0025-5416(81)90121-X.

[42] H.L. Dunegan, D.O. Harris, C.A. Tatro, Fracture analysis by use of acoustic emission, Eng. Fract. Mech. 1 (1968), https://doi.org/10.1016/0013-7944(68)90018-0.

[43] A.K. Bhattacharya, N. Parida, P.C. Gope, Monitoring hydrogen embrittlement cracking using acoustic emission technique, J. Mater. Sci. 27 (1992) 1421–1427, https://doi.org/10.1007/BF00542897.

[44] D. Martelo, D. Sampath, A. Monici, R. Morana, R. Akid, Correlative analysis of digital imaging, acoustic emission, and fracture surface topography on hydrogen assisted cracking in Ni-alloy 625+, Eng. Fract. Mech. 221 (2019), 106678 https://doi.org/10.1016/j.engfracmech.2019.106678.

[45] E. Pomponi, A. Vinogradov, A real-time approach to acoustic emission clustering, Mech. Syst. Signal Process. 40 (2013) 791–804, https://doi.org/10.1016/j.ymssp.2013.03.017.

[46] A.Y. Vinogradov, Principles of statistical and spectral analysis of acoustic emission and their application to plastic deformation of metallic glasses, J. Acoust. Emiss. 16 (1998) S158–S169.

[47] A. Vinogradov, I.S. Yasnikov, Y. Estrin, Stochastic dislocation kinetics and fractal structures in deforming metals probed by acoustic emission and surface topography measurements, J. Appl. Phys. 115 (2014), 233506, https://doi.org/10.1063/1.4884682.

[48] A. Vinogradov, V. Patlan, S. Hashimoto, Spectral analysis of acoustic emission during cyclic deformation of copper single crystals, Philos. Mag. A 81 (2001) 1427–1446, https://doi.org/10.1080/01418610108214356.

[49] A. Vinogradov, M. Nadtochiy, S. Hashimoto, S. Miura, Correlation between spectral parameters of acoustic emission during plastic deformation of Cu and Cu&ndash, Al Single and Polycrystals, Materials Transactions, JIM. 36 (1995) 426–431, https://doi.org/10.2320/matertrans1989.36.426.

[50] X. Lu, D. Wang, R. Johnsen, Hydrogen diffusion and trapping in nickel-based alloy 625: an electrochemical permeation study, Electrochim. Acta 421 (2022), 140477, https://doi.org/10.1016/j.electacta.2022.140477.

[51] X. Lu, T. Depover, R. Johnsen, Evaluation of hydrogen diffusion and trapping in nickel Alloy 625 by thermal desorption spectroscopy, Int. J. Hydrogen Energy (2022), https://doi.org/10.1016/J.IJHYDENE.2022.07.094.

[52] T. Ungár, Dislocation densities, arrangements and character from X-ray diffraction experiments, Mater. Sci. Eng. A 309–310 (2001) 14–22, https://doi.org/10.1016/S0921-5093(00)01685-3.

[53] A. Lazarev, A. Vinogradov, About plastic instabilities in iron and power spectrum of acoustic emission, J. Acoust. Emiss. 27 (2009) 27. https://www.ndt.net/?id=10861. (Accessed 12 May 2022). accessed.

[54] A. Sendrowicz, A.O. Myhre, A.V. Danyuk, A. Vinogradov, Dislocation kinetics explains energy partitioning during strain hardening: model and experimental validation by infrared thermography and acoustic emission, Mater. Sci. Eng. A (2022), 143969, https://doi.org/10.1016/J.MSEA.2022.143969.

[55] D.L. Holt, Dislocation cell formation in metals, J. Appl. Phys. 41 (1970) 3197–3201, https://doi.org/10.1063/1.1659399.

[56] Y. Bergström, A dislocation model for the stress-strain behaviour of polycrystalline α-Fe with special emphasis on the variation of the densities of mobile and immobile dislocations, Mater. Sci. Eng. 5 (1970) 193–200, https://doi.org/10.1016/0025-5416(70)90081-9.

[57] A. Sendrowicz, A.O. Myhre, S.W. Wierdak, A. Vinogradov, Challenges and accomplishments in mechanical testing instrumented by in situ techniques: infrared thermography, digital image correlation, and acoustic emission, Appl. Sci. 11 (2021) 6718, https://doi.org/10.3390/app11156718.

[58] A. Vinogradov, I.S. Yasnikov, D.L. Merson, Phenomenological approach towards modelling the acoustic emission due to plastic deformation in metals, Scripta Mater. 170 (2019) 172–176, https://doi.org/10.1016/j.scriptamat.2019.06.011.

[59] A. Vinogradov, A. Lazarev, M. Linderov, A. Weidner, H. Biermann, Kinetics of deformation processes in high-alloyed cast transformation-induced plasticity/twinning-induced plasticity steels determined by acoustic emission and scanning electron microscopy: influence of austenite stability on deformation mechanisms, Acta Mater. 61 (2013) 2434–2449, https://doi.org/10.1016/j.actamat.2013.01.016.

[60] M. Linderov, C. Segel, A. Weidner, H. Biermann, A. Vinogradov, Deformation mechanisms in austenitic TRIP/TWIP steels at room and elevated temperature investigated by acoustic emission and scanning electron microscopy, Mater. Sci. Eng. A 597 (2014) 183–193, https://doi.org/10.1016/j.msea.2013.12.094.

[61] A.V. Danyuk, D.L. Merson, I.S. Yasnikov, E.A. Agletdinov, M.A. Afanasiev, A. Vinogradov, The effect of stacking fault energy on acoustic emission in pure metals with face-centered crystal lattice, Lett. Mater. 7 (2017) 437–441, https://doi.org/10.22226/2410-3535-2017-4-437-441.

[62] T. Tabata, H.K. Birnbaum, Direct observations of the effect of hydrogen on the behavior of dislocations in iron, Scripta Metall. 17 (1983) 947–950, https://doi.org/10.1016/0036-9748(83)90268-5.

[63] J. Eastman, F. Heubaum, T. Matsumoto, H.K. Birnbaum, The effect of hydrogen on the solid solution strengthening and softening of nickel, Acta Metall. 30 (1982) 1579–1586, https://doi.org/10.1016/0001-6160(82)90178-X.

[64] C.B. Scruby, H.N.G. Wadley, J.J. Hill, Dynamic elastic displacements at the surface of an elastic half-space due to defect sources, J. Phys. D Appl. Phys. 16 (1983) 1069–1083, https://doi.org/10.1088/0022-3727/16/6/015.

[65] S. Martin, A. Weidner, C. Ullrich, C. Schimpf, M. Motylenko, R. Lehnert, H. Biermann, D. Rafaja, A. Vinogradov, Y. Estrin, Deformation behaviour of TWIP steels: constitutive modelling informed by local and integral experimental methods used in concert, Mater. Char. 184 (2022), 111667, https://doi.org/10.1016/j.matchar.2021.111667.

[66] A. Vinogradov, E. Vasilev, M. Linderov, D. Merson, In situ observations of the kinetics of twinning–detwinning and dislocation slip in magnesium, Mater. Sci. Eng. A 676 (2016) 351–360, https://doi.org/10.1016/J.MSEA.2016.09.004.

[67] A. Vinogradov, D. Orlov, A. Danyuk, Y. Estrin, Effect of grain size on the mechanisms of plastic deformation in wrought Mg–Zn–Zr alloy revealed by acoustic emission measurements, Acta Mater. 61 (2013) 2044–2056, https://doi.org/10.1016/J.ACTAMAT.2012.12.024.

[68] A. Vinogradov, M. Heczko, V. Mazánová, M. Linderov, T. Kruml, Kinetics of cyclically-induced mechanical twinning in γ-TiAl unveiled by a combination of acoustic emission, neutron diffraction and electron microscopy, Acta Mater. 212 (2021), 116921, https://doi.org/10.1016/J.ACTAMAT.2021.116921.

[69] M. Seita, J.P. Hanson, S. Gradečak, M.J. Demkowicz, The dual role of coherent twin boundaries in hydrogen embrittlement, Nat. Commun. 6 (2015) 6164, https://doi.org/10.1038/ncomms7164.

[70] J. Crank, The Mathematics of Diffusion, second ed., 1979. https://books.google.com/books?hl=en&lr=&id=eHANhZwVouYC&oi=fnd&pg=PA1&ots=fA23tUijL0&sig=7j_iJbkf9CgqhWcvYj8h8z8pKPY. (Accessed 5 January 2023). accessed.

[71] T. Boniszewski, G.C. Smith, The influence of hydrogen on the plastic deformation ductility, and fracture of nickel in tension, Acta Metall. 11 (1963) 165–178, https://doi.org/10.1016/0001-6160(63)90209-8.

[72] D.G. Ulmer, C.J. Altstetter, Phase relations in the hydrogen-austenite system, Acta Metall. Mater. 41 (1993) 2235–2241, https://doi.org/10.1016/0956-7151(93)90393-7.

[73] N. Narita, C.J. Altstetter, H.K. Birnbaum, Hydrogen-related phase transformations in austenitic stainless steels, Metall. Trans. A 13 (1982) 1355–1365, https://doi.org/10.1007/BF02642872.

[74] U.F. Kocks, H. Mecking, Physics and phenomenology of strain hardening: the FCC case, Prog. Mater. Sci. 48 (2003) 171–273, https://doi.org/10.1016/S0079-6425(02)00003-8.

[75] Y. Zhu, Z. Li, M. Huang, Solute hydrogen effects on plastic deformation mechanisms of α-Fe with twist grain boundary, Int. J. Hydrogen Energy 43 (2018) 10481–10495, https://doi.org/10.1016/J.IJHYDENE.2018.04.133.

[76] J. Song, W.A. Curtin, Mechanisms of hydrogen-enhanced localized plasticity: an atomistic study using α-Fe as a model system, Acta Mater. 68 (2014) 61–69, https://doi.org/10.1016/J.ACTAMAT.2014.01.008.

[77] A.H. Cottrell, Theory of dislocations, Prog. Met. Phys. 4 (1953) 205–264, https://doi.org/10.1016/0502-8205(53)90018-5.

[78] A.H. Cottrell, D.L. Dexter, Dislocations and plastic flow in crystals, Am. J. Phys. 22 (1954) 242–243, https://doi.org/10.1119/1.1933704.

[79] S. Asgari, E. El-Danaf, S.R. Kalidindi, R.D. Doherty, Strain hardening regimes and microstructural evolution during large strain compression of low stacking fault energy fee alloys that form deformation twins, Metall. Mater. Trans. A Phys. Metall. Mater. Sci. 28 (1997) 1781–1795, https://doi.org/10.1007/s11661-997-0109-3.

[80] J.B. Singh, Mech. Behavi. Alloy 625 (2022) 111–174, https://doi.org/10.1007/978-981-19-1562-8_4.

[81] X. Lu, A. Díaz, J. Ma, D. Wang, J. He, Z. Zhang, R. Johnsen, The effect of plastic deformation on hydrogen diffusion in nickel Alloy 625, Scripta Mater. 226 (2023), 115210, https://doi.org/10.1016/J.SCRIPTAMAT.2022.115210.

Hydrogen-induced degradation behavior of nickel alloy studied using acoustic emission technique

Chandrahaasan K. Soundararajan[a*], Aleksander Myhre[a,1], Aleksander Sendrowicz [a,2], Xu Lu[a], Alexey Vinogradov [a,b,3*]

[a] *Department of Mechanical and Industrial Engineering, Norwegian University of Science and Technology, No-7491, Trondheim, Norway.*

[b] *Magnesium Research Center (MRC), Kumamoto University, 2-39-1 Kurokami, Chuo-ku, Kumamoto 860-8555, Japan.*

Figure 1: The XRD pattern the hydrogen charged sample (-1 mA/cm^2 – 24 hrs.). From XRD data, neither peak shift nor broadening observed. In addition, the microstructure shows no evidence of charging induced slip.

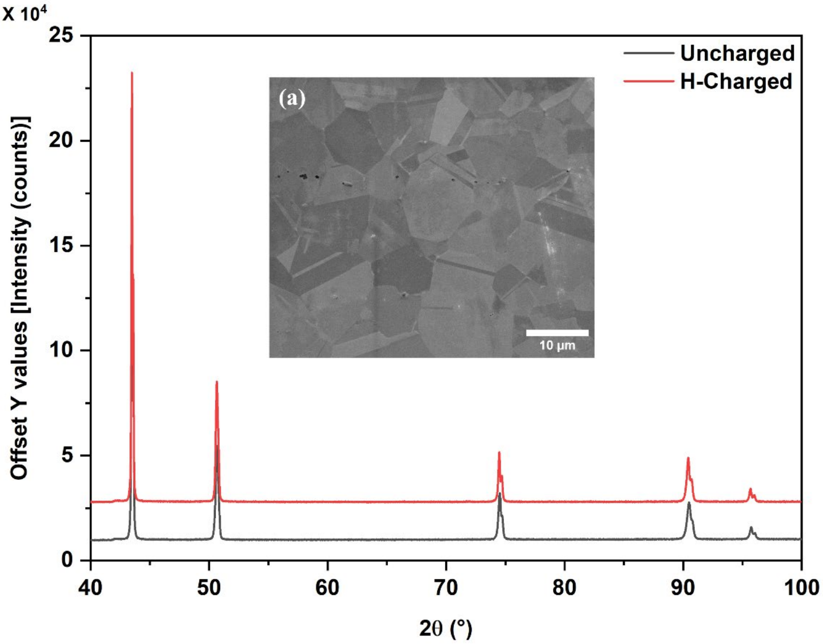

Figure 1: The XRD pattern for the hydrogen charged sample (-1 mA/cm^2). The patterns recorded before charging (Black), right after charging (Red). The inset (a) shows the microstructure right after charging.

---

[1] Currently at DNV AS, Høvik 1363, Norway

[2] Currently at Kilter AS, Viken 1405, Norway

[3] Currently at Kumamoto University, Kumamoto 860-8555, Japan

Figure 2: Fracture surface of -5 mA/cm^2 sample. Extensive slip lines are observed at the fracture surface close to the surface also at a depth of 50 µm from the surface.

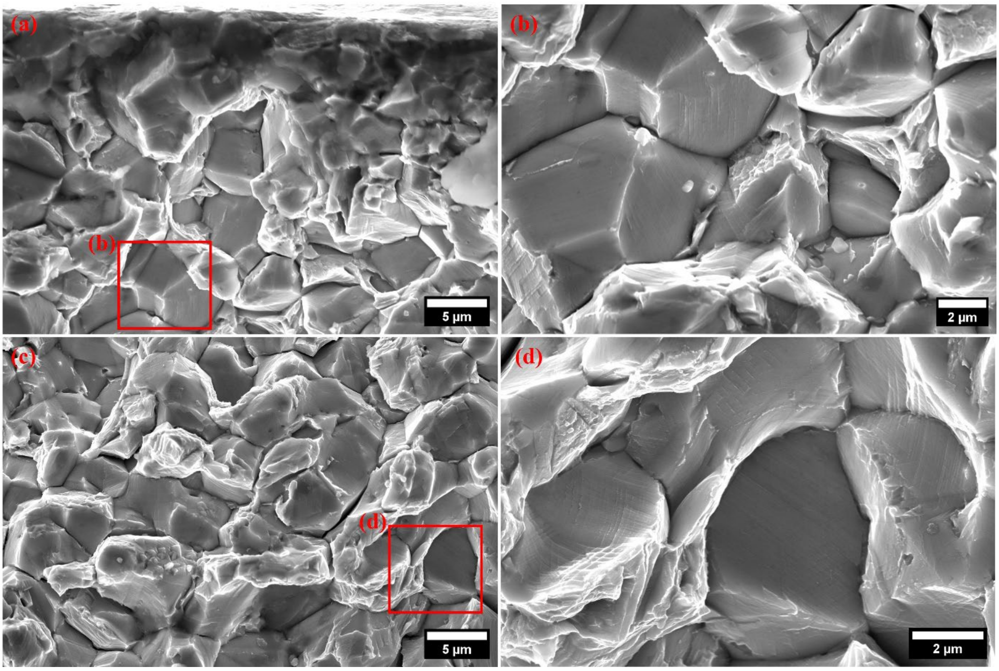

Figure 2: Fracture surface of -5 mA/cm2 sample. (a-b) Image captured close to the surface of the sample. (c-d) image captured at the depth of 50 µm from the surface of the sample.

Figure 3: Normalized PSD for hydrogen-charged sample (-5 mA/cm^2 – 24 hrs.). The crack power spectra show dominant low frequency components.

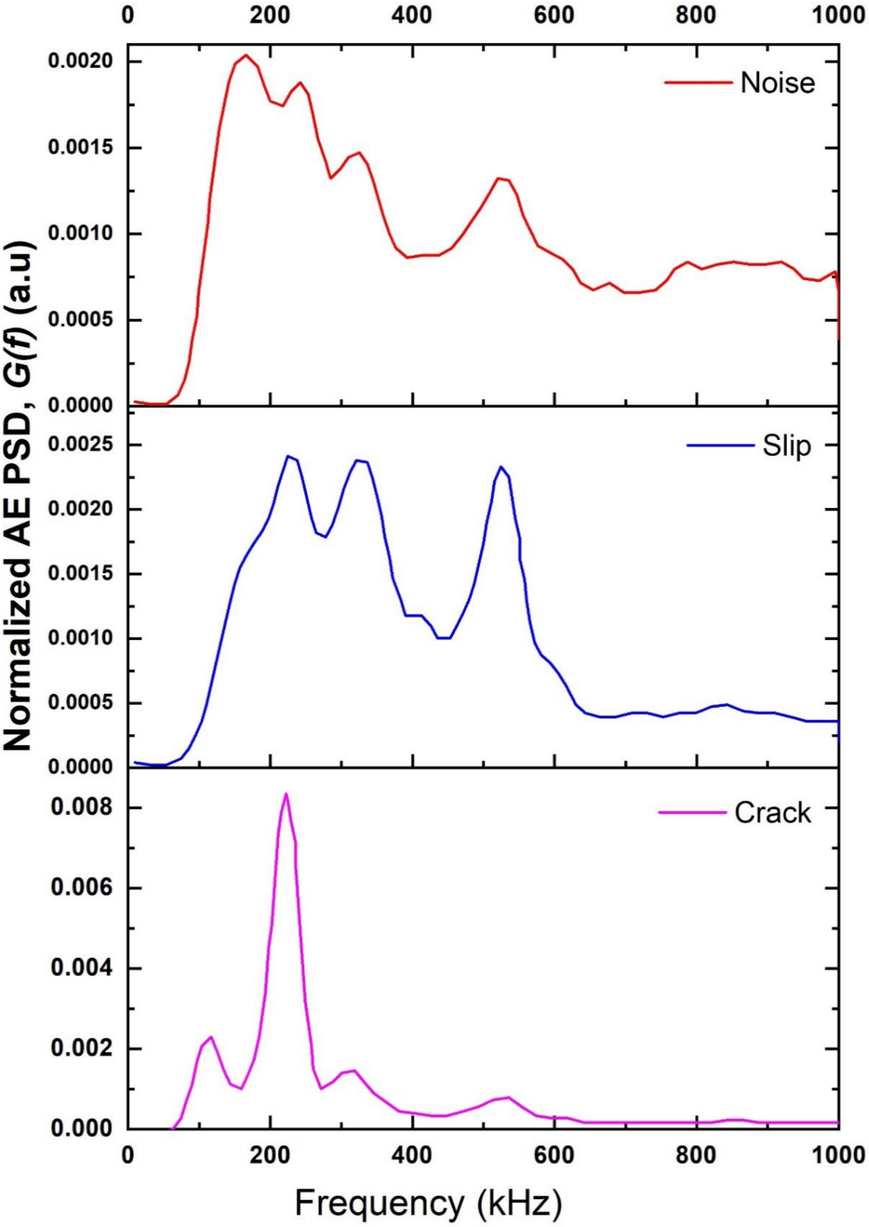

Figure 3: Normalized PSD for hydrogen-charged sample (-5 mA/cm2).

Figure 4: Cross-sectional microstructure of hydrogen-charged sample (-5 mA/cm^2 – 24 hrs) after interrupted tensile test. The figure suggest a depth dependent clear crack transition from transgranular to intergranular type.

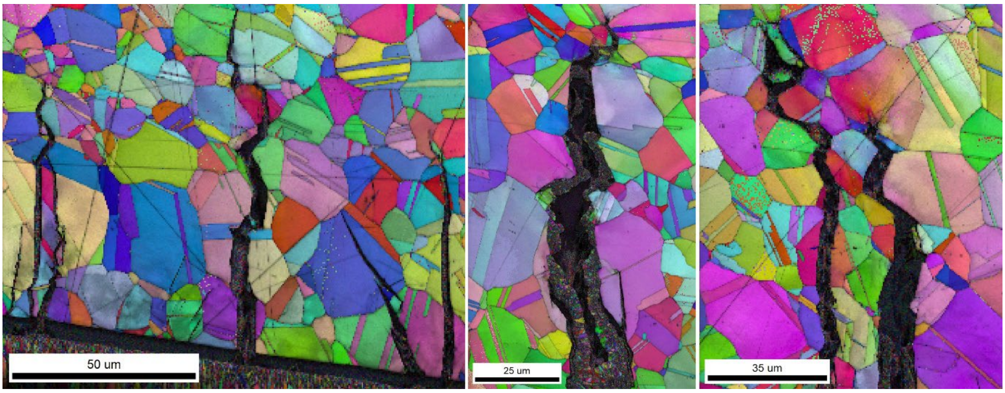

Figure 4: Cross-sectional microstructure of hydrogen-charged sample (-5 mA/cm^2 – 24 hrs.) after interrupted tensile test.

Article II

Effect of hydrogen on nanomechanical properties of Inconel 625 studied using in-situ electrochemical nanoindentation technique

CK Soundararajan, D Wang, A Vinogradov

Journal of Alloys and Compounds, 169742 (2023).

Journal of Alloys and Compounds 948 (2023) 169742

Contents lists available at ScienceDirect

Journal of Alloys and Compounds

journal homepage: www.elsevier.com/locate/jalcom

Research Article

Effect of hydrogen on nanomechanical properties of Inconel 625 studied using in-situ electrochemical nanoindentation technique

Chandrahaasan K. Soundararajan [a,*], Dong Wang [a], Alexey Vinogradov [a,b]

[a] Department of Mechanical and Industrial Engineering, Norwegian University of Science and Technology, No-7491 Trondheim, Norway
[b] Magnesium Research Center (MRC), Kumamoto University, 2-39-1 Kurokami, Chuo-ku, Kumamoto 860-8555, Japan

ARTICLE INFO

Article history:
Received 28 October 2022
Received in revised form 4 March 2023
Accepted 19 March 2023
Available online 22 March 2023

Keywords:
Hydrogen embrittlement
Electrochemical nanoindentation
Dislocations
Nickel-based alloys
Vacancy

ABSTRACT

In-situ electrochemical nanoindentation (ECNI) experiment is performed to probe the nanomechanical properties of Inconel 625 alloy under a hydrogen environment. The hydrogen effect on various stages of the load-displacement (LD) plot is quantified. The pop-in load, which indicates the onset of a homogenous dislocation nucleation event, is reduced with hydrogen charging, which augers well with the 'Defactant' concept. The hydrogen solute hinders dislocation glide during pop-in (reduced pop-in width), and the resultant glide resistance force is found to be linearly dependent on dissolved hydrogen concentration. We have also quantified the hydrogen-reduced activation barrier for the secondary source by examining the secondary elastic hardening stage from LD data. Hydrogen charging-induced slip line formation and nanohardness variation at different polarizations are explained using a simple diffusion-desorption model. Furthermore, the electron channeling contrast imaging technique is used to study the dislocation patterns around the indents in air and in the hydrogen environment to shed light on the difference in plastic behavior.

© 2023 The Author(s). Published by Elsevier B.V. This is an open access article under the CC BY license (http://creativecommons.org/licenses/by/4.0/).

1. Introduction

Nickel-based alloys are often the preferred materials of choice in oil and gas industries owing to their mechanical strength and corrosion resistance properties [1]. However, they are susceptible to hydrogen embrittlement (HE) in hydrogen-evolving environments, for example, during cathodic protection in seawater conditions. The HE in structural material has been a topic of interest for scientific and industrial communities for about a century, as hydrogen-induced damage can be catastrophic and fatal. Over the years, multiple mechanisms have been proposed to explain the embrittlement behavior, either acting individually or in various combinations: hydrogen-enhanced localized plasticity [2,3], hydrogen-enhanced decohesion [4,5], hydrogen-enhanced strain-induced vacancy formation [6,7], and the 'Defactant' mechanism [8,9].

The fundamental bottleneck, which limits our understanding of the problem, is the substantial number of intrinsic (microstructural constituents) and extrinsic variables (stress state, environment) involved. For instance, the HE behavior of the material is often reported by performing macroscale tensile testing of precharged samples. The inherent fast diffusing nature of hydrogen combined with a strong concentration gradient during pre-charging poses several problems in quantifying the hydrogen effect on the dislocation behavior and the mechanical properties. Unlike other interstitial or substitutional alloying elements, hydrogen interacts with dislocations in a rather complex way. The development of miniaturized material testing setups in a controlled hydrogen environment paved the way for a better understanding of hydrogen-dislocation interactions [3,10–13]. One such leap forward in technology has been the development of the in-situ electrochemical nanoindentation technique (ECNI) [14,15].

The nanoindentation (NI) technique has enjoyed increasing recognition for studying the local dislocation dynamics over the years [16–21]. By probing the minimal material volume, microstructure-specific mechanical properties and the strengthening mechanism at the nanoscale can be inferred. The load-displacement (LD) data from NI experiment helps to relate the local mechanical properties with dislocation activities. When the sharp tip is engaged on defect-free volume, it exhibits 'pop-in' - a strain burst event, which signifies a transition from the elastic to elastoplastic behavior. The shear stress at this junction reaches a theoretical strength of the material and results in a dislocation avalanche generated underneath the indenter. The dislocation velocity is estimated to be close to that of sound at this stage [17,22,23]. The sharp rise in the load during the post-pop-in stage is associated with the behavior of the indenter catching up with the material that ran away during the displacement

---

[*] Corresponding author.
E-mail address: chandrahaasan.k.soundararajan@ntnu.no (C.K. Soundararajan).

https://doi.org/10.1016/j.jallcom.2023.169742
0925-8388/© 2023 The Author(s). Published by Elsevier B.V. This is an open access article under the CC BY license (http://creativecommons.org/licenses/by/4.0/).

excursion. This secondary elastic hardening is related to the energy required to glide the store dislocations and activate the secondary sources to proceed into a continuum plasticity regime.

In-situ ECNI experiments on pure Ni and its alloy variants have been reported earlier, wherein hydrogen reduced the pop-in load and increased the hardness. These observations were related to the reduced activation energy barrier for dislocation nucleation; concurrently, hydrogen hinders the dislocation motion by the solute drag effect. The microstructural evolution during the discrete event (pop-in stage) and at the continuous hardening stage (plastic regime) are discussed quite extensively in the abundant literature [24–26]. However, the hydrogen effect on the transition stage, i.e., the secondary elastic hardening stage, has not been reported so far, to the best of our knowledge.

In this work, we have employed the in-situ ECNI technique to study the HE behavior of the Inconel 625 alloy. The individual stages of LD data during NI were compared for uncharged and hydrogen-charged samples. Furthermore, the hydrogen concentration-dependent nanomechanical response is discussed in detail.

2. Methodology

2.1. Sample preparation and microstructure characterization

The discs of 12 mm in diameter were cut from the as-received Inconel 625 alloy by the electrical discharge machine. The chemical composition is shown in Table 1. The fabricated coupons were ground and polished until 200 nm colloidal silica to get a deformation-free surface. The microstructure characterization was performed by means of electron backscattered diffraction (EBSD) and electron channeling contrast imaging (ECCI) using the Quanta 650 FEG microscope (Thermo Fisher Inc.). The EBSD patterns were acquired by the NORDIF camera at an acceleration voltage of 20 kV and a working distance of ~16 mm, and the subsequent indexing and analysis were done using the TSL OIM software. The ECCI measurements were performed at the same acceleration voltage and a working distance of ~7 mm.

2.2. In-situ electrochemical nanoindentation

Indentations were performed using the TI 950 Triboindenter under the load-controlled mode. The maximum load was set as 2000 μ*N*, and the loading and unloading rate was 8000 μ*N/s*, with additional 0.25 s at 10 % of peak load during unloading for the thermal drift correction. In-situ hydrogen charging was performed using a custom-designed three-electrode electrochemical cell; a platinum plate was used as a counter electrode (anode), the test specimen functioned as a cathode, and Hg/Hg_2SO_4 served as a reference electrode. A detailed description of the experimental setup can be found elsewhere [14,15]. The electrolyte used in this work contained a glycerol and borax mixture, and charging was done at room temperature. Three different cathodic charging potentials (−1200 *mV*, −1400 *mV* and −1700 *mV*) and one anodic potential (0 *mV*) were selected from the polarization curve represented in Fig. 1.

The sequence of the indentation experiment was as follows: the sample was first tested in air followed by a sequence of − 1200 *mV* and − 1400 *mV* cathodic charging and 0 *mV* anodic discharging; then the potential was changed to − 1700 *mV* and finally to 0 *mV*. Before the ECNI test at each cathodic potential, the sample was charged for 2 *hours* to allow sufficient hydrogen to be absorbed into the sample, and the duration of anodic discharging was set to 1 *hour* to study the time effect on the nanomechanical properties. At least 50 indentations were performed in each condition to ensure the reproducibility of the results. During the in-situ ECNI test, scanning probe microscopy (SPM) images were obtained after each charging/discharging process to track the changes in surface topography.

Table 1
Chemical composition of Inconel 625.

Element	Ni	Cr	Mo	Fe	Nb	Al	P
wt%	62.8	21.3	8.3	3.7	3.25	0.22	< 0.005
Element	C	Ti	Mn	Si	Cu	Co	S
wt%	0.018	0.05	0.07	0.08	0.02	0.18	0.0003

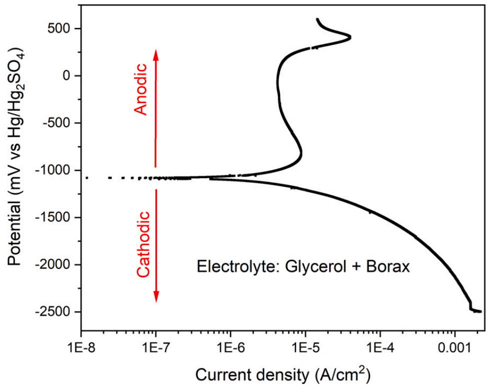

Fig. 1. Polarization plot for the current work.

2.3. Thermal desorption analysis and XRD measurement

The total hydrogen content is estimated using the Bruker G4 Phoenix DH hydrogen analyzer. The hydrogen content in Table 2 is estimated by following the same sequence/charging history as that of the indentation experiment. The grazing incidence X-ray diffraction (GIXRD, D8 DaVinci with LynxEye™ Superspeed detector) was performed to characterize electrochemical charging-induced near-surface damage. The GIXRD was operated by using Cu Kα radiation (40 kV) at the 1° incident angle at the step size of 0.02° and the counting time of 3 *s* per step.

3. Results and discussion

3.1. Microstructure

The grain size of the as-received Inconel 625 alloy was 10 μ*m*. Multiple annealing twins are present in the microstructure. Detailed microstructural characterization of the same material has been reported in the earlier work focused on the hydrogen diffusion processes [27,28]. Navigating to the grain with indents and performing adequate indentation in air as well as at different polarization conditions to obtain statistically relevant data points is a challenging task. Thus, several series of indentations were performed on randomly chosen grains, and the results were compared. The orientation independence of the pop-in behavior has been reported for various alloy classes [24,29,30]. Fig. 2a shows the IPF map of the indents performed under different polarization sequences, and the representative LD data for each condition is presented in Fig. 2c. Around 50 indents, which cover 5 grains on average, were performed for each condition. Furthermore, the indents close to (< 1 μ*m* range) grain boundaries and twin boundaries are eliminated during data processing to minimize the possible influence of grain boundaries on the dislocation nucleation process.

Table 2
Total hydrogen content for different charging conditions.

Sample ID	Charging potential and duration	Total hydrogen content ($wt.\ ppm$)
H1	-1200 mV/ 2 h	0.18 ± 0.03
H2	-1200 mV/ 2 h (+) − 1400 mV/ 2 h	0.36 ± 0.02
A2	-1200 mV/ 2 h (+) − 1400 mV/ 2 h (+) 0 mV/ 1 h	0.2 ± 0.05
H3	-1200 mV/ 2 h (+) − 1400 mV/ 2 h (+) 0 mV/ 1 h (+) − 1700 mV/ 2 h	1.16 ± 0.02
A2	-1200 mV/ 2 h (+) − 1400 mV/ 2 h (+) 0 mV/ 1 h (+) − 1700 mV/ 2 h (+) 0 mV/ 1 h	0.11

3.2. Nanomechanical properties

Fig. 2b shows the typical LD plot during NI. Five loading stages can be easily distinguished: (1) primary elastic region; (2) incipient plastic region; (3) secondary elastic region; (4) elasto-plastic region; and (5) unloading region. From each of these stages, different properties can be derived. In the following sections, we shall quantify the hydrogen influence on the nanomechanical properties and the corresponding microstructural changes occurring during the indentation process.

3.2.1. Hydrogen-induced surface slip steps

The sample surface is critical during nanomechanical testing. Using scanning probe microscopy (SPM), the surface was continuously monitored during cathodic charging. Fig. 3a-d shows the sample surface after each cathodic polarization sequence. During charging at the low cathodic potentials (−1200 mV and −1400 mV), the surface remains intact; the root mean square roughness value change is lesser than 4 %. The extensive slip lines can be, however, observed at the high cathodic potential of − 1700 mV (Fig. 3g). The total hydrogen content obtained from the TDS technique (Table 2) was used to quantify the stress generated during charging. The internal stress ($\sigma_{\rm int}$) generated due to dissolved hydrogen solute is estimated using the following simplified relation [31,32]:

$$\sigma_{\rm int} = B\frac{\Delta V}{V_0} = B\frac{H_a}{M_a}\frac{\Delta \nu}{\Omega} = 180 \times 0.28 \times \frac{H_a}{M_a} \tag{1}$$

where $B = 180 GPa$ is the bulk modulus of the material, the ratio ($\frac{\Delta\nu}{\Omega} = 0.28$) is the volumetric strain due to a single hydrogen solute atom in the nickel lattice [33] and the atomic ratio between hydrogen and metal atom $\left(\frac{H_a}{M_a}\right)$ is expressed as:

$$\frac{H_a}{M_a} = \frac{C_s \times \frac{N_A}{M_H}}{(10^6 - C_s) \times \frac{N_A}{M_A}} \tag{2}$$

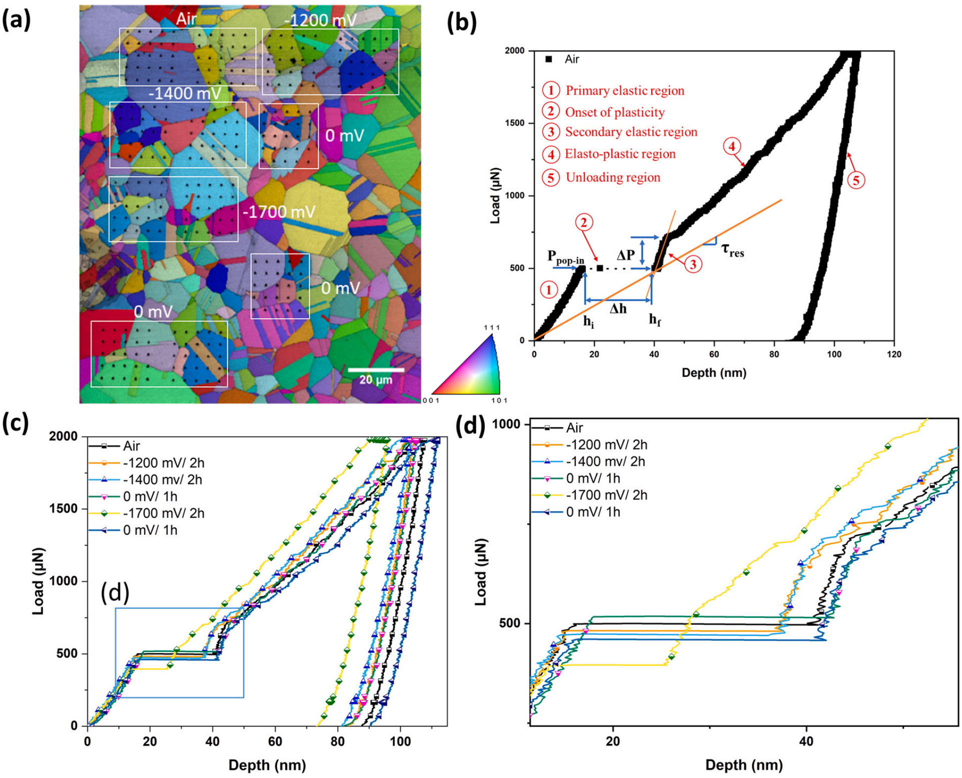

Fig. 2. (a) The inverse pole figure map overlayed with the image quality map with indents performed under different polarization conditions. (b) Typical load-displacement graph showing the definitions of different stages and parameters used in this work. (c) Representative load-displacement data for each polarization condition. (d) Enlarged image in (c) shows the pop-in stage.

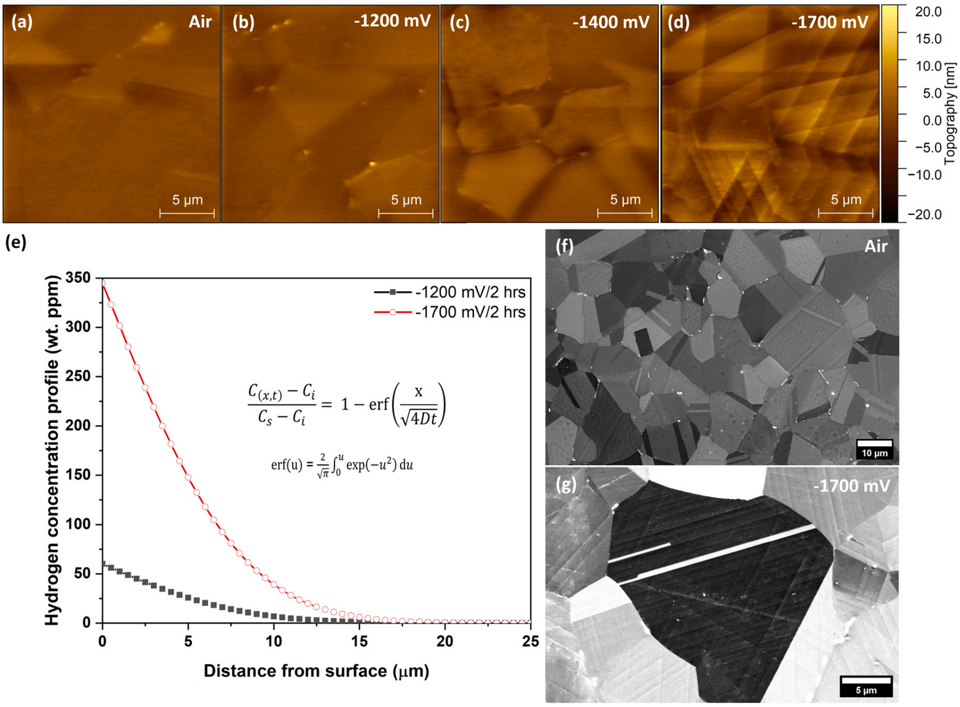

Fig. 3. (a-d) Surface topography after different charging conditions. (a) Uncharged, (b) − 1200 mV, (c) − 1400 mV, (d) − 1700 mV. (e) Thin plate diffusion model for two different charging conditions. BSE images of (f) uncharged microstructure, (g) after charging at − 1700 mV for 2 h.

where N_A is Avogadro's constant, M_H and M_A denote the number of hydrogen and metal atoms, respectively, C_s is the surface concentration of hydrogen, which, according to [34] $C_s = \frac{\omega C_M}{4}\sqrt{\frac{\pi}{Dt}}$. Here ω is the thickness of the specimen, C_M is the total hydrogen concentration, t is the charging time, and D is the diffusion coefficient, which is chosen as 2.77×10^{-15} m^2/s for the present study following the previous work [27].

The internal stress calculated using the above expression for − 1200 mV is 175 MPa and for − 1700 mV is 1015 MPa. Moreover, the yield strength of the material is 450 MPa, lower than the hydrogen-induced internal stress for − 1700 mV condition. To evaluate the internal stress, we assume that the lattice expansion is caused by the isotropic internal stress due to abundant dissolved hydrogen. Moreover, the estimation of the internal stress is based on Hooke's law and can only be regarded as a crude 1st order approximation. Though the stress value estimated in this way is not precise, it qualitatively explains why plastic deformation occurs in the surface region, as is experimentally observed in the form of slip steps at the free surface.

The hydrogen distribution in the sample $C_{(x,t)}$ can be calculated from Fick's law using a thin plate model as:

$$\frac{C_{(x,t)} - C_0}{C_s - C_0} = 1 - erf\left(\frac{x}{\sqrt{4Dt}}\right) 0 < x < l \tag{3}$$

$$\mathrm{erf}(u) = \frac{2}{\pi}\int_0^u \exp(-u^2)du \tag{4}$$

where C_0 is the initial hydrogen concentration and erf(u) denotes the error function. The inherent slow diffusivity and high hydrogen solubility suggest that there is a steep concentration gradient prevailing in the sample close to the free surface (Fig. 3e). Supersaturation of hydrogen at the surface swells the lattice resulting in the stress gradient [32]. Upon reaching the critical resolved shear stress, the dislocations are generated to accommodate the strain. Furthermore, hydrogen presence could accelerate the generation process by reducing the dislocation line energy as follows from the `Defactant` model framework [9], resulting in the slip steps during charging at the high cathodic potential.

3.2.2. *Primary elastic region*

The reduced elastic modulus (E_r) of the material is estimated by fitting the elastic part of the LD plot with the Hertzian relation as shown below [35]:

$$P = \frac{4}{3}E_r\sqrt{R}h^3 \tag{5}$$

where P is the applied load, h is the indentation depth, and R is the radius of the Berkovich tip curvature; for the present experiment, R = 1 µm. The reduced modulus (E_r) is expressed as:

$$\frac{1}{E_r} = \frac{1 - \nu_1^2}{E_1} + \frac{1 - \nu_2^2}{E_2} \tag{6}$$

with ν - the Poisson's ratio, and the subscript indexes 1 and 2 correspond to the sample and diamond tip, respectively. By substituting the know values (E_2 = 1140 GPa, $\nu_2 = 0.07$ *and* $\nu_1 = 0.3$) into Eq.(6), the modulus of the material (E_1) is obtained. Fig. 4 summarizes the average modulus value for each charging condition. One can see that the elastic modulus exhibits an ascending trend with hydrogen concentration. However, the experimental measurement error renders it challenging to quantify the influence of hydrogen. Moreover, the hydrogen effect on the modulus is still under debate. Nanoindentation of precharged and aged Ni-201 alloy indicates the decrease in the reduced modulus value ascribed to vacancy enhancement during charging [36]. On the other hand, the ECNI study

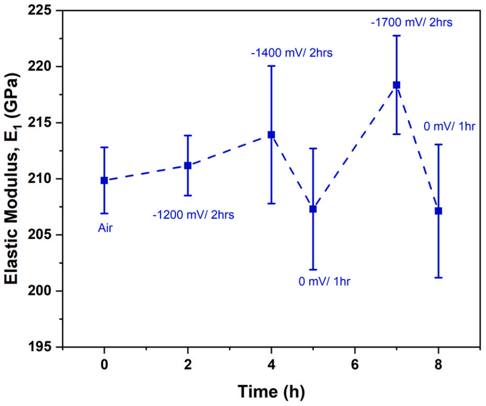

Fig. 4. Elastic modulus of the material (E_1) at different charging conditions.

performed on a wide compositional range of Ni-Cr alloys shows no change in the modulus value due to hydrogen [37]. The modulus of the material assessed by NI is sensitive to the surface roughness since the elastic depth being probed is approximately 15 nm [32,38]. The formation of slip lines (Fig. 3d) under the high cathodic charging potential ($-1700\,mV$) could influence the measured modulus value, giving rise to an evidently large deviation observed for charging at − 1700 mV followed by the subsequent holding at 0 mV potential.

3.2.3. Hydrogen-assisted pop-in behavior

For a well-annealed ductile material, the pop-in load indicates the onset of homogenous dislocation nucleation. The BSE image of the as-received sample in Fig. 3f shows the low dislocation density inside the grains. For the present work, only the results of indentation performed inside the grain are included for data processing. Therefore, it is plausible that dislocation nucleation is associated with the homogeneous model. The pop-in phenomenon occurs when the stress beneath the indenter ($\tau_{\max}$) reaches the theoretical shear strength of the material. From elastic continuum mechanics, this strength is estimated as [39]:

$$\tau_{\max} = 0.31\left(\frac{6E_r^2}{\pi^3R^2}P_{pop-in}\right)^{1/3} \tag{7}$$

where P_{pop-in} is the pop-in load. The average pop-in load for different polarization conditions is given in Fig. 5a. In addition, variation of $\tau_{\max}$ with hydrogen content is shown in Fig. 5b. From the viewpoint of classical dislocation theory [39], the activation energy required to nucleate dislocation is given by:

$$\Delta G = 2\pi r\ W + \pi r^2\ \gamma - \pi r^2 b\tau_{\max(pop-in)} \tag{8}$$

where W is the line energy of the dislocation loop, γ is the stacking fault energy (SFE), b is the magnitude of the Burgers vector, and r is the dislocation loop radius. The line energy of dislocation (W) is given by:

$$W = \frac{2-\nu}{1-\nu}\frac{Gb^2r}{4}\left(\ln\frac{4r}{\rho}-2\right) \tag{9}$$

where ν is the Poisson's ratio, G is the shear modulus of the material, and ρ is the dislocation core radius. According to the 'Defactant' model, hydrogen segregation around the dislocation core increases its radius, thereby reducing both the dislocation line energy and the stacking fault energy value [8,14,40,41]. Furthermore, several studies have reported that hydrogen reduces the shear modulus, which is equivalent to the reduction in the chemical bond strength as assumed in the HEDE model [25,42]. Thus, it is easier to form the dislocation loop under a hydrogen environment, and the effect is more pronounced with the increase in dissolved hydrogen. At low cathodic potentials (-1200 mV and -1400 mV), the reduction of $\tau_{\max}$ is less than 1 %, whereas for − 1700 mV it is 6.5 %. In the present work, hydrogen reduced the pop-in load during cathodic polarization and its recovery during anodic polarization agrees with the 'Defactant' concept. Thus it can be concluded that the reduction in pop-in load during charging at low cathodic potential (-1200 mV and -1400 mV), where uniform surface integrity was maintained, is due to hydrogen-enhanced homogenous dislocation nucleation through the reduction of dislocation line energy and stacking fault energy.

We should reiterate here that in the case of − 1700 mV charging conditions, extensive surface slip steps are observed (Fig. 3d). Therefore, the observed pop-in behavior is suggestive of a heterogenous dislocation nucleation event. In the present work, hydrogen charging at the high cathodic potential results in lattice distortion at the near-surface region in the form of dislocations and vacancies; here, the pop-in event begins at lower stress by activating the pre-existing dislocations instead of generating new source [43,44]. Another possibility for reducing the pop-in load can be reasoned with hydrogen-enhanced vacancy-mediated heterogeneous dislocation nucleation [45], wherein agglomeration and collapse of vacancies into the plates on densely packed planes aid the heterogeneous dislocation nucleation process. Further, the interaction between

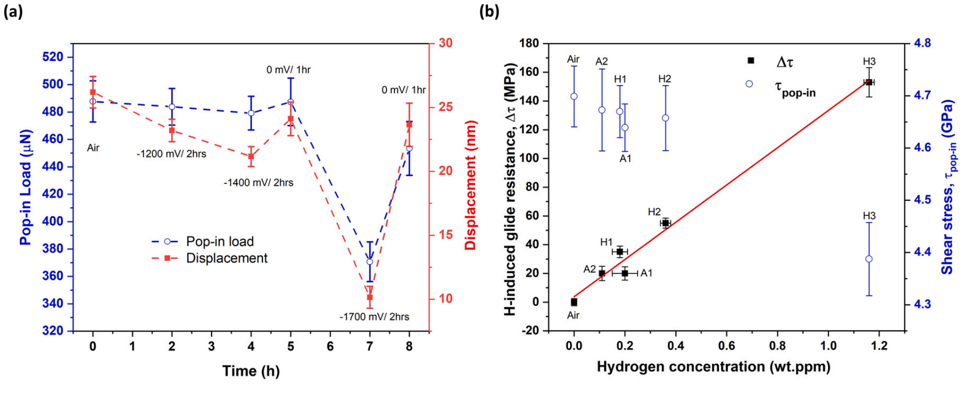

Fig. 5. (a) Mean pop-in load and displacement for indents performed at different conditions. (b) Hydrogen concentration-dependent glide resistance stress and homogenous dislocation nucleation stress.

hydrogen atoms and vacancies would increase equilibrium vacancy concentration by reducing their formation energy. Thus, the hydrogen-enhanced vacancies and vacancy clusters can reduce the required stress for the onset of plastic deformation [46]. The pop-in behavior is highly sensitive to the surface quality. Thus, it can be concluded that for a defect-free surface, the pop-in is facilitated through the hydrogen-enhanced homogeneous dislocation nucleation. In contrast, in other cases, the pop-in happens by activating the pre-existing defects.

In contrast to the pop-in load, a more pronounced reduction in the pop-in width with hydrogen was observed (12.5 %, 15 % and 59 % for −1200 mV, −1400 mV and −1700 mV, respectively). The plastic shear strain during indentation can be expressed as $\gamma_p = \frac{nb}{a} = \frac{\Delta h}{a}$, where n is the number of dislocation loops, Δh is the pop-in width, and a is the representative length [47]. Considering constant plastic strain during the pop-in event, the reduction in the pop-in width accompanies the reduced representative length. This also suggests that a substantial fraction of the kinetic energy of plastic work has dissipated, resulting in a smaller travel distance of the leading dislocation. The resistance force (stress) against dislocation glide can be estimated by [17]:

$$\tau_{res} = \frac{P_{pop-in}}{9\pi R h_f} \tag{10}$$

where h_f is the displacement at the end of the pop-in event (see Fig. 2b). The glide resistance stress due to a dissolved solute ($\Delta\tau$) can be estimated by:

$$\Delta\tau = \tau_{res}^{H} - \tau_{res}^{air} \tag{11}$$

The linear relationship between hydrogen concentration and the resistance to dislocation glide strongly suggests hydrogen-enhanced solution hardening (see Fig. 5b). This is consistent with the comprehensive energy model proposed by Wang et al. [48], wherein the hydrogen solute is shown to increase the lattice friction energy by the solute drag effect [49]. When diffusion of hydrogen solute could not keep up with the applied strain rate, hardening is observed. The hydrogen-induced solute drag effect is often reported during macroscale tensile testing at high strain rates [50–52] and in-situ nanoindentation experiments performed at varying strain rates [14,24,26,53].

3.2.4. Secondary elastic stage - post-pop-in

As has been discussed above, it is believed that during the pop-in event, the stress beneath the indenter reaches theoretical shear strength resulting in rapid dislocation multiplication. Few data points at the pop-in stage (Fig. 2b) suggest that the indenter could not keep up with the material. Dislocations at this junction are estimated to travel at high velocity resulting in a high strain rate locally until they are starved of the shear driving force and finally become immobilized. Right after the pop-in stage, the general plastic deformation dominates in the mechanical response with the increasing applied load (strain rate here corresponds to loading rate, which is much lower than in the pop-in stage). The general plastic deformation necessitates the activation of additional slip systems to accommodate the imposed plastic strain. The additional energy is required to overcome the back stress of stored dislocation loops from the prior excursion event, which manifests itself as a steep load increase and can be considered as the secondary elastic hardening stage. The duration of this stage, ΔP, can be interpreted as the force required to activate the secondary source (additional slip systems) [47]. Fig. 6 shows the reduction in ΔP with hydrogen concentration, suggesting that hydrogen reduces the initial activation barrier by making the stage shorter. According to the sequential planar slip model proposed by Cordill et al. [17], the shear stress (τ) required to activate a new source is given by $\tau = \tau_0 + \frac{T}{l_w b}$, where τ_0 is the intrinsic yield component, T is the dislocation line tension, l_w is the wall spacing. Hydrogen reducing the elastic stress field of dislocations according to the 'HELP' model would explain the reduced shear stress for secondary source activation. Our study suggests, however, that hydrogen exerts a dual effect: on the one hand, it hinders dislocation motion during the pop-in stage and facilitates slip activity by reducing the activation barrier for general plastic deformation to commence on the other. A similar result was reported by K. A. Nibur et al. on hydrogen-charged SS316 steel [53]. These authors have observed the reduced excursion depth in hydrogen-charged conditions, which was explained by the solute drag effect. In addition, the second dislocation excursion and extensive slip steps in hydrogen-charged samples were observed and correlated to the hydrogen-reduced critical resolved shear stress for secondary slip plane activation under the 'HELP' framework. For an in-depth understanding of underlying mechanisms, it is essential to characterize the dislocation evolution as a function of load, which is an ongoing work and will be reported elsewhere.

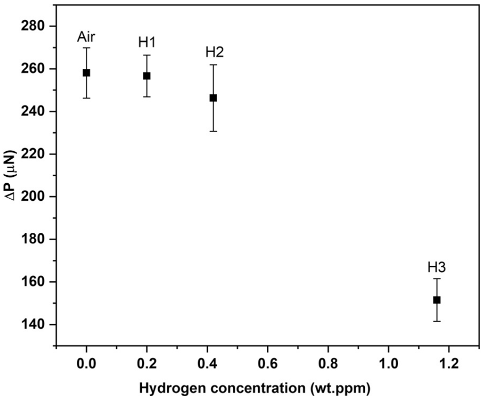

Fig. 6. Hydrogen concentration-dependent activation load to trigger the secondary source.

3.2.5. Hydrogen effect on elasto-plastic region

The elasto-plastic part of LD curve represents the continuous hardening process. From the Tabor relation, the elasto-plastic loading can be expressed as [54]:

$$P = CA_c\sigma \tag{12}$$

Here, $C = 3$ is the Tabor constant, A_c is the projected area that depends on the indentation depth and indenter shape, σ is the overall stress; for the present case, only the dislocation strengthening stress component σ_{dis} and the solid solution strengthening stress $\sigma_{ss} = 330MPa$ [24] are considered. Further σ_{dis} can be expressed as [55]:

$$\sigma_{dis} = M\alpha Gb\sqrt{\rho_{SSD} + \rho_{GND}} \tag{13}$$

where $M = 3.06$ is the Taylor factor, $\alpha = 0.5$ is an empirical factor, G is the shear modulus, ρ_{SSD} and ρ_{GND} are statistically dislocation density and geometrically necessary dislocation density, respectively. For a well-annealed ductile material, ρ_{SSD} is of the order of 10^{12} m^{-2} [55], the same value is used in the present study. The ρ_{GND} value can be estimated according to the Nix-Gao model [56] as:

$$\rho_{GND} = \frac{3}{2}\frac{1}{f^3}\frac{\tan^2\theta}{bh} \tag{14}$$

where f is the ratio between the radius of the plastic zone r_{pz} and contact area a_c, and θ is the angle between the sample surface and

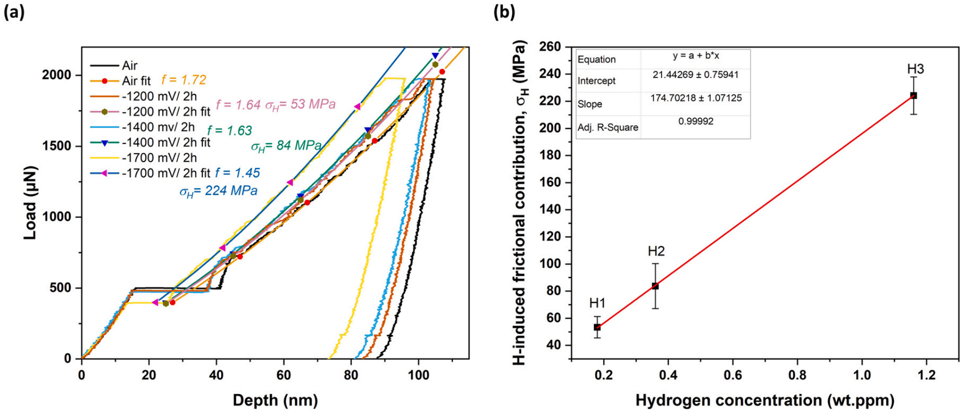

Fig. 7. Representative L–D curves of the sample under different testing conditions; the elastoplastic part is fitted by the Nix–Gao model based on Tabor's relation. (b) Linear dependence of the frictional stress is plotted as a function of hydrogen concentration.

the Berkovich indenter (24.63°). The plastic zone radius (r_{pz}) is calculated by the Lawn model [57] as:

$$r_{pz} = \varphi\left(\frac{E}{G}\right)^{1/n}\tan^{1/3}\theta h_r \tag{15}$$

where φ is the geometrical constant (3.64 for Berkovich tip), E and G are elastic and shear modulus of the material, respectively, h_r is the residual indentation depth. The contact area a_c is computed from the size of the imprints from ECC images (Fig. 8a-c). The elasto-plastic load relation in Eq. (12) can be rewritten by combining Eq. (13) & (14):

$$P = CM\alpha GbA_c\sqrt{\rho_{SSD} + \frac{3}{2}\frac{1}{f^3}\frac{\tan^2\theta}{bh}} + C(\sigma_{ss} + \sigma_H)A_c \tag{16}$$

Here σ_H is additional solid solution strengthening contribution provided by hydrogen, for uncharged sample (air), this term can be neglected. By fitting Eq. (16) to LD data, the hydrogen-induced frictional contribution (σ_H) is obtained for each charging potentials.

Fig. 7a shows the fit data and the f value for each charging conditions. The reduction in the f value indicates the shrinkage of the plastic zone. Moreover, the linear dependence of the frictional stress with the solute concentration suggests that the dislocation motion is hydrogen-impeded due to the solute drag effect [49].

3.2.6. Hydrogen influence on hardness

The hardness of the material is estimated using the Oliver-Pharr method by fitting the unloading curve of the LD plot [58]. The mean hardness value for each polarization condition is summarized in Fig. 8d. The average hardness value for the uncharged (air) sequence is 4.67 *GPa*. During hydrogen charging, the progressive increase in the hardness is observed compared to the results in air (7 % increase for −1200 *mV* and 14 % for −1400 *mV*).

The ECC images in Fig. 8a-c show the dislocation patterns around the indents for air, − 1200 *mV* and − 1400 *mV*, respectively. The dislocations appear as white lines or dots on the dark background. The plastic zone size (r_c) which signifies extensive dislocations around the indents marked by the yellow circle. The dislocations that reside far away from the indents are excluded as they were shown to influence plasticity in a weak manner [59]. The hydrogen-enhanced hardening behavior can be observed from ECC images as the reduced indent area (r_c). The 10.3 % reduction in r_c value for − 1200 *mV* and 13 % for − 1400 *mV* conditions, agrees well with the observed hardness increase. The increased lattice friction due to dissolved hydrogen atoms acting as obstacles to dislocation motion results in increased hardness [38,49].

After one hour of discharging at 0 *mV* anodic potential (from −1400 *mV*), the hardness reduced from 5.33 *GPa* to 4.95 *GPa* (7 %). However, the difference in hardness between the anodic and the air sequence is 6 %, suggesting residual hydrogen presence. The non-recovery in hardness can be explained by a simple diffusion-desorption model based on Eq.(3). Considering a thin plate model for hydrogen diffusion, the concentration profile after two hours of charging can be expressed as:

$$\frac{C_{(x,7200)}}{C_s} = 1 - erf\left(\frac{x}{\sqrt{4Dt}}\right) 0 < x < l \tag{17}$$

In the case of hydrogen desorption, the following relation is considered. Since the initial hydrogen distribution is non-uniform, a non-steady state equation which accounts for constant surface concentration and initial distribution *f(x)* (Eq. (18)) is considered for anodic discharging. It was tactically assumed that the surface concentration reaches zero at the start of anodic polarization:

$$c(x,t) = c_1 + (c_2 - c_1)\frac{x}{l} + \frac{2}{\pi}\sum_1^\infty \frac{c_2\cos n\pi - c_1}{n}\sin\left(\frac{n\pi x}{l}\right)\exp\left(-\frac{Dn^2\pi^2 t}{l^2}\right) + \frac{2}{l}\sum_1^\infty \sin\frac{n\pi x}{l}\exp\left(-\frac{Dn^2\pi^2 t}{l^2}\right)\int_0^1 f'(x)\sin\frac{n\pi x'}{l}dx' \tag{18}$$

with the boundary conditions:

$$c = c_1,\ x = 0,\ t \geq 0 \tag{19}$$

$$c = c_2,\ x = l,\ t \geq 0 \tag{20}$$

The plot in Fig. 8e shows the estimated hydrogen concentration profile in the sample after four hours of charging and one hour of discharging. The computed from Eq. (15) plastic zone, which impacts the hardness value for the present work, is of 875 *nm*. The hydrogen concentration at 875 *nm* depth after two hours of charging is 92.3 %, while after one hour of discharging, it is about 10.5 %. Thus, the residual hydrogen present after the sequence of four hours of charging and one hour of discharging is about 11.3 %, which is consistent with the observed non-recovery of hardness after the anodic sequence of 0 *mV*.

When the potential is changed to − 1700 *mV*, the hardness increases by about 20 %. During the subsequent anodic polarization,

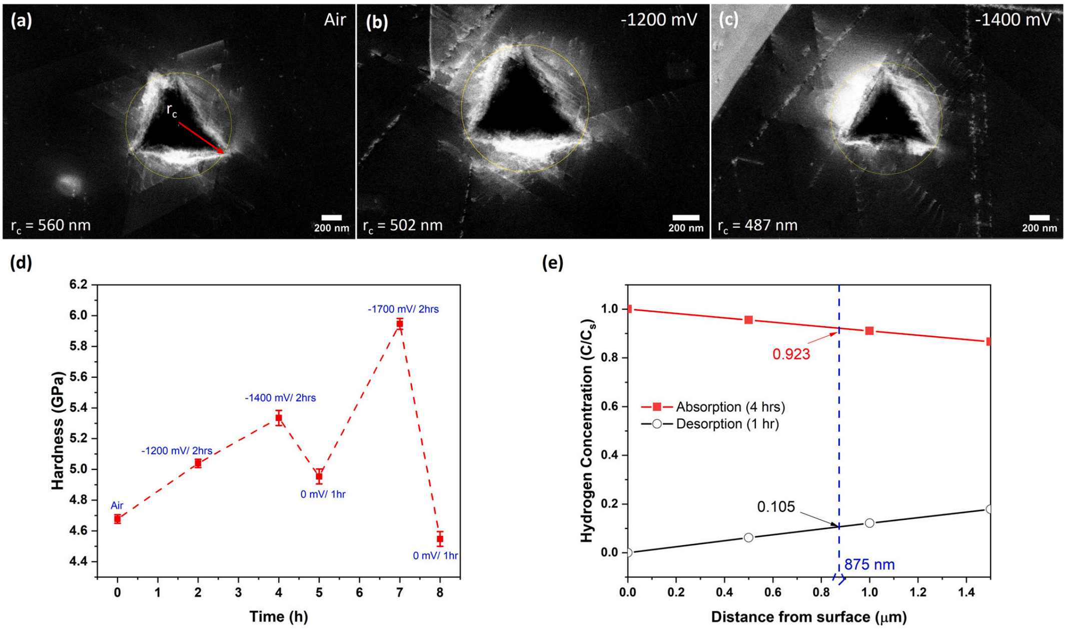

Fig. 8. (a-c) ECCI patterns depicting dislocation patterns around indents: (a) uncharged, (b) − 1200 mV, (c) − 1400 mV. (d) shows the hardness variation at different charging conditions, and (e) represents the absorption-desorption profile for the present case.

the hardness reduced from 5.94 GPa to 4.54 GPa (23 % reduction). Interestingly, the hardness of the 0 *mV* anodic sequence is much lower than that of air (2.3 % reduction). The total hydrogen content measured after two hours of charging at − 1700 *mV* followed by one hour at 0 *mV* anodic polarization is 0.11 *wt. ppm* (10 % residual hydrogen present). The observed reduction could be due to the formation and stabilization of vacancies by hydrogen.

The inherent slow diffusivity and high solubility of hydrogen in nickel suggest the steep concentration gradient prevailing during electrochemical charging (Fig. 3e). This, in turn, generated hydrogen-induced non-uniform defect distribution. To characterize the near-surface damages, we have employed the GIXRD technique; for the current experiment, the X-ray penetration depth is estimated as 0.5 μ*m*. Fig. 9 shows the GIXRD pattern for uncharged (air) and hydrogen-charged samples (−2000 *mV* for 12 h). The shift in the peak position of the hydrogen-charged sample is thought to reflect the lattice distortion due to the abundant creation of vacancies. The decrease in the lattice parameter to the value lower than that of the matrix due to abundant vacancies has been reported in earlier works [7,51,60]. During charging at the high cathodic potential, extensive slip lines form (see Fig. 3d), which inadvertently generates vacancies. Hydrogen tends to stabilize the vacancy clusters under the 'Defactant' concept, thus making the matrix softer [8,61].

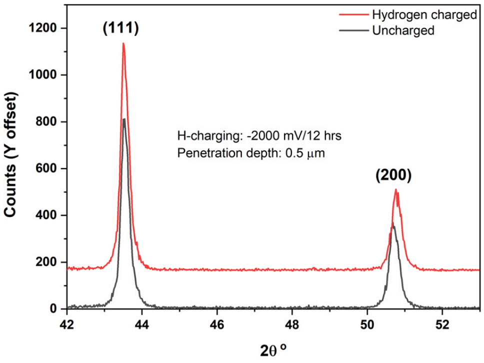

Fig. 9. Grazing incidence XRD pattern measured for the uncharged sample and hydrogen-charged sample.

4. Conclusions

In this work, the hydrogen-influenced nanomechanical properties of Inconel 625 were investigated using the in-situ ECNI technique. The individual stages of the load-displacement curves were compared, and the main findings are summarized below:

- The slip line formation at the high cathodic potential is due to sluggish diffusion and supersaturation of hydrogen at the surface. The internal stress caused by dissolved hydrogen exceeds the yield strength triggering dislocations escaping at the surface.
- No discernable influence of hydrogen on the elastic modulus is observed as the measured values fluctuate within the standard error range as that of air. The significant deviation in the case of − 1700 *mV* and subsequent 0 *mV* potential is associated with the surface deformation witnessed by the surface slip steps.
- Hydrogen reduces the pop-in load in harmony with the 'Defactant' mechanism. The resistance force to dislocation motion during pop-in due to dissolved hydrogen shows a linear relationship, suggesting the appreciable solid solution hardening effect of hydrogen.
- The duration of the secondary elastic post-pop-in stage (ΔP) can be interpreted as the force required to activate the secondary source. Hydrogen reduces the line energy of the dislocations according to the 'HELP' model and, subsequently, facilitates the secondary source activation.

- Using the Nix–Gao model based on Tabor's relation-based, the hydrogen contribution is estimated to the lattice frictional stress during the continuous hardening regime. The linear dependence of the hydrogen-induced frictional stress with solute concentration suggests that the dislocation motion is impeded by hydrogen atoms to the solute drag effect.
- The non-recovery of hardness after the first anodic sequence is due to residual hydrogen, which is explained by the simple diffusion-desorption model. The decrease in hardness, much lower than that in air during the second anodic sequence, is attributed to non-equilibrium vacancies generated during charging and the subsequent stabilization by hydrogen, thereby making the matrix softer.

CRediT authorship contribution statement

Chandrahaasan K. Soundararajan: Conceptualization, Methodology, Investigation, Writing – original draft, Writing – review & editing. **Dong Wang**: Methodology, Writing – review & editing. **Alexey Vinogradov**: Supervision, Writing – review & editing.

Data availability

The data required to reproduce these findings cannot be shared at this time as this data also forms part of an ongoing study.

Declaration of Competing Interest

The authors declare that they have no known competing financial interests or personal relationships that could have appeared to influence the work reported in this paper.

Acknowledgements

This work was supported by the Research Council of Norway and industrial partners through the M-HEAT Project (294689).

References

[1] M. Iannuzzi, A. Barnoush, R. Johnsen, Materials and corrosion trends in offshore and subsea oil and gas production, Npj Mater. Degrad. 1 (2017) 1–11, https://doi.org/10.1038/s41529-017-0003-4
[2] H.K. Birnbaum, P. Sofronis, Hydrogen-enhanced localized plasticity—a mechanism for hydrogen-related fracture, Mater. Sci. Eng. A 176 (1994) 191–202, https://doi.org/10.1016/0921-5093(94)90975-X
[3] I.M. Robertson, P. Sofronis, A. Nagao, M.L. Martin, S. Wang, D.W. Gross, K.E. Nygren, Hydrogen embrittlement understood, Metall. Mater. Trans. B 46 (2015) 1085–1103, https://doi.org/10.1007/s11663-015-0325-y
[4] R.A. Oriani, Whitney award lecture—1987: hydrogen—the versatile embrittler, Corrosion 43 (1987) 390–397, https://doi.org/10.5006/1.3583875
[5] R.A. Oriani, P.H. Josephic, Equilibrium aspects of hydrogen-induced cracking of steels, Acta Metall. 22 (1974) 1065–1074, https://doi.org/10.1016/0001-6160(74)90061-3
[6] K. Takai, H. Shoda, H. Suzuki, M. Nagumo, Lattice defects dominating hydrogen-related failure of metals, Acta Mater. 56 (2008) 5158–5167, https://doi.org/10.1016/j.actamat.2008.06.031
[7] Y. Fukai, Y. Shizuku, Y. Kurokawa, Superabundant vacancy formation in Ni–H alloys, J. Alloy. Compd. 329 (2001) 195–201, https://doi.org/10.1016/S0925-8388(01)01603-6
[8] R. Kirchheim, Revisiting hydrogen embrittlement models and hydrogen-induced homogeneous nucleation of dislocations, Scr. Mater. 62 (2010) 67–70, https://doi.org/10.1016/j.scriptamat.2009.09.037
[9] R. Kirchheim, A. Pundt, Hydrogen in Metals, fifth ed., Elsevier, 2014, https://doi.org/10.1016/B978-0-444-53770-6.00025-3
[10] P.J. Ferreira, I.M. Robertson, H.K. Birnbaum, Hydrogen effects on the interaction between dislocations, Acta Mater. 46 (1998) 1749–1757, https://doi.org/10.1016/S1359-6454(97)00349-2
[11] A. Barnoush, J. Dake, N. Kheradmand, H. Vehoff, Examination of hydrogen embrittlement in FeAl by means of in situ electrochemical micropillar compression and nanoindentation techniques, Intermetallics (2010) 1385–1389, https://doi.org/10.1016/j.intermet.2010.01.001
[12] T. Hajilou, Y. Deng, B.R. Rogne, N. Kheradmand, A. Barnoush, In situ electrochemical microcantilever bending test: a new insight into hydrogen enhanced cracking, Scr. Mater. 132 (2017) 17–21, https://doi.org/10.1016/j.scriptamat.2017.01.019
[13] J. Kim, C.C. Tasan, Microstructural and micro-mechanical characterization during hydrogen charging: an in situ scanning electron microscopy study, Int J. Hydrog. Energy 44 (2019) 6333–6343, https://doi.org/10.1016/j.ijhydene.2018.10.128
[14] A. Barnoush, Hydrogen Embrittlement, Revisited by in Situ Electrochemical Nanoindentation, (2007) 288.
[15] A. Barnoush, H. Vehoff, Electrochemical nanoindentation: a new approach to probe hydrogen/deformation interaction, Scr. Mater. 55 (2006) 195–198, https://doi.org/10.1016/j.scriptamat.2006.03.041
[16] W.W. Gerberich, J.C. Nelson, E.T. Lilleodden, P. Anderson, J.T. Wyrobek, Indentation induced dislocation nucleation: the initial yield point, Acta Mater. 44 (1996) 3585–3598, https://doi.org/10.1016/1359-6454(96)00010-9
[17] M.J. Cordill, N.R. Moody, W.W. Gerberich, The role of dislocation walls for nanoindentation to shallow depths, Int J. Plast. 25 (2009) 281–301, https://doi.org/10.1016/j.ijplas.2008.02.003
[18] D.F. Bahr, G. Vasquez, Effect of solid solution impurities on dislocation nucleation during nanoindentation, J. Mater. Res. 20 (2005) 1947–1951, https://doi.org/10.1557/JMR.2005.0244
[19] A. Barnoush, Correlation between dislocation density and nanomechanical response during nanoindentation, Acta Mater. 60 (2012) 1268–1277, https://doi.org/10.1016/j.actamat.2011.11.034
[20] C. Shin, S. Shim, Dislocation mechanisms of radius effect on displacement bursts during spherical nanoindentations, J. Mater. Res 27 (2012) 2161–2166, https://doi.org/10.1557/jmr.2012.183/figures/5
[21] L. Zhang, T. Ohmura, Plasticity Initiation and Evolution during Nanoindentation of an Iron-3% Silicon Crystal, (2014). doi: 10.1103/PhysRevLett.112.145504.
[22] T. Ohmura, M. Wakeda, Pop-in phenomenon as a fundamental plasticity probed by nanoindentation technique, Materials 14 (2021) 1879, https://doi.org/10.3390/ma14081879
[23] W.G. Johnston, J.J. Gilman, Dislocation velocities, dislocation densities, and plastic flow in lithium fluoride crystals, J. Appl. Phys. 30 (1959) 129–144, https://doi.org/10.1063/1.1735121
[24] X. Lu, Y. Ma, D. Peng, R. Johnsen, D. Wang, In situ nanomechanical characterization of hydrogen effects on nickel-based alloy 725 under different metallurgical conditions, J. Mater. Sci. Technol. (2022), https://doi.org/10.1016/J.JMST.2022.07.006
[25] S.K. Lawrence, B.P. Somerday, M.D. Ingraham, D.F. Bahr, Probing the effect of hydrogen on elastic properties and plastic deformation in nickel using nanoindentation and ultrasonic methods, JOM 70 (2018) 1068–1073, https://doi.org/10.1007/s11837-018-2850-z
[26] G. Hachet, A. Oudriss, A. Barnoush, T. Hajilou, D. Wang, A. Metsue, X. Feaugas, Antagonist softening and hardening effects of hydrogen investigated using nanoindentation on cyclically pre-strained nickel single crystal, Mater. Sci. Eng. A 803 (2021) 140480, https://doi.org/10.1016/J.MSEA.2020.140480
[27] X. Lu, D. Wang, R. Johnsen, Hydrogen diffusion and trapping in nickel-based alloy 625: an electrochemical permeation study, Electrochim. Acta 421 (2022) 140477, https://doi.org/10.1016/j.electacta.2022.140477
[28] X. Lu, T. Depover, R. Johnsen, Evaluation of hydrogen diffusion and trapping in nickel Alloy 625 by thermal desorption spectroscopy, Int. J. Hydrog. Energy (2022), https://doi.org/10.1016/J.IJHYDENE.2022.07.094
[29] D. Wang, A.B. Hagen, D. Wan, X. Lu, R. Johnsen, Probing hydrogen effect on nanomechanical properties of X65 pipeline steel using in-situ electrochemical nanoindentation, Mater. Sci. Eng. A 824 (2021) 141819, https://doi.org/10.1016/j.msea.2021.141819
[30] F. Pöhl, Pop-in behavior and elastic-to-plastic transition of polycrystalline pure iron during sharp nanoindentation, Sci. Rep. 9 (1) (2019) 1–12 https://doi.org/10.1038/s41598-019-51644-5.
[31] X. Lu, D. Wang, D. Wan, Z.B.B. Zhang, N. Kheradmand, A. Barnoush, Effect of electrochemical charging on the hydrogen embrittlement susceptibility of alloy 718, Acta Mater. 179 (2019) 36–48, https://doi.org/10.1016/j.actamat.2019.08.020
[32] D. Wang, X. Lu, Y. Deng, D. Wan, Z. Li, A. Barnoush, Effect of hydrogen-induced surface steps on the nanomechanical behavior of a CoCrFeMnNi high-entropy alloy revealed by in-situ electrochemical nanoindentation, Intermetallics 114 (2019) 106605, https://doi.org/10.1016/j.intermet.2019.106605
[33] H.J. Bauer, G. Berninger, G. Zimmermann, Nachweis interstitieller Wasserstoffeinlagerung in NiCu-Legierungen auf magnetischem und röntgenographischem Wege, Z. Fur Naturforsch. Sect. A J. Phys. Sci. 23 (1968) 2023–2029, https://doi.org/10.1515/ZNA-1968-1220
[34] A.E. Pontini, J.D. Hermida, X-Ray diffraction measurement of the stacking fault energy reduction induced by hydrogen in an AISI 304 steel, Scr. Mater. 37 (1997) 1831–1837, https://doi.org/10.1016/S1359-6462(97)00332-1
[35] K. Johnson, K. Johnson, Contact Mechanics, 1987. https://books.google.com/books?hl=en&lr=&id=Do6WQlUwbpkC&oi=fnd&pg=PR9&ots=grifmyj97X&sig=kZehZTKCh4P_3duAxdcTlzWqhm4. (Accessed 18 August 2022).
[36] S.K. Lawrence, B.P. Somerday, R.A. Karnesky, Elastic property dependence on mobile and trapped hydrogen in Ni-201, JOM 69 (2017) 45–50, https://doi.org/10.1007/S11837-016-2157-X
[37] K. Tomatsu, K. Miyata, T. Omura, Electrochemical nanoindentation study on influence of hydrogen on local mechanical properties of Fcc metals at slow strain rate, ISIJ Int. 56 (2016) 418–423, https://doi.org/10.2355/isijinternational.ISIJINT-2015-289
[38] D. Wang, X. Lu, Y. Deng, X. Guo, A. Barnoush, Effect of hydrogen on nanomechanical properties in Fe-22Mn-0.6C TWIP steel revealed by in-situ electrochemical nanoindentation, Acta Mater. 166 (2019) 618–629, https://doi.org/10.1016/J.ACTAMAT.2018.12.055
[39] J. Hirth, J. Lothe, Theory of Dislocations, (1982).

[40] A. Barnoush, M. Asgari, R. Johnsen, Resolving the hydrogen effect on dislocation nucleation and mobility by electrochemical nanoindentation, Scr. Mater. 66 (2012) 414–417, https://doi.org/10.1016/j.scriptamat.2011.12.004

[41] M. Wen, S. Fukuyama, K. Yokogawa, Atomistic simulations of hydrogen effect on dissociation of screw dislocations in nickel, Scr. Mater. 52 (2005) 959–962, https://doi.org/10.1016/j.scriptamat.2005.01.044

[42] C. Müller, M. Zamanzade, C. Motz, The impact of hydrogen on mechanical properties; a new in situ nanoindentation testing method, Micromachines 2019 10 (10) (2019) 114, https://doi.org/10.3390/MI10020114

[43] D. Shan, L. Yuan, B. Guo, Multiscale simulation of surface step effects on nanoindentation, Mater. Sci. Eng. A 412 (2005) 264–270, https://doi.org/10.1016/J.MSEA.2005.08.198

[44] Z. Wang, H. Bei, E.P. George, G.M. Pharr, Influences of surface preparation on nanoindentation pop-in in single-crystal Mo, Scr. Mater. 65 (2011) 469–472, https://doi.org/10.1016/J.SCRIPTAMAT.2011.05.030

[45] G. Yang, Y. Zhao, D.H. Lee, J.M. Park, M.Y. Seok, J.Y. Suh, U. Ramamurty, J. il Jang, Influence of hydrogen on incipient plasticity in CoCrFeMnNi high-entropy alloy, Scr. Mater. 161 (2019) 23–27, https://doi.org/10.1016/J.SCRIPTAMAT.2018.10.010

[46] I. Salehinia, D.F. Bahr, The impact of a variety of point defects on the inception of plastic deformation in dislocation-free metals, Scr. Mater. 66 (2012) 339–342, https://doi.org/10.1016/J.SCRIPTAMAT.2011.11.028

[47] N. Adachi, T. Suzuki, T. Ohmura, Y. Todaka, Analytical approach for pop-in and post-pop-in deformation behavior during nanoindentation: effect of solute Si in interstitial free steel, J. Mater. Res 36 (2021) 2571–2581, https://doi.org/10.1557/S43578-021-00136-2/FIGURES/9

[48] D. Wang, X. Lu, M. Lin, D. Wan, Z. Li, J. He, R. Johnsen, Understanding the hydrogen effect on pop-in behavior of an equiatomic high-entropy alloy during in-situ nanoindentation, J. Mater. Sci. Technol. 98 (2022) 118–122, https://doi.org/10.1016/j.jmst.2021.04.060

[49] J. Song, W.A. Curtin, Mechanisms of hydrogen-enhanced localized plasticity: an atomistic study using α-Fe as a model system, Acta Mater. 68 (2014) 61–69, https://doi.org/10.1016/J.ACTAMAT.2014.01.008

[50] T. Boniszewski, G.C. Smith, The influence of hydrogen on the plastic deformation ductility, and fracture of nickel in tension, Acta Metall. 11 (1963) 165–178, https://doi.org/10.1016/0001-6160(63)90209-8

[51] S.K. Lawrence, Y. Yagodzinskyy, H. Hänninen, E. Korhonen, F. Tuomisto, Z.D. Harris, B.P. Somerday, Effects of grain size and deformation temperature on hydrogen-enhanced vacancy formation in Ni alloys, Acta Mater. 128 (2017) 218–226, https://doi.org/10.1016/j.actamat.2017.02.016

[52] D.G. Ulmer, C.J. Altstetter, Hydrogen-induced strain localization and failure of austenitic stainless steels at high hydrogen concentrations, Acta Metall. Et. Mater. 39 (1991) 1237–1248, https://doi.org/10.1016/0956-7151(91)90211-I

[53] K. NIBUR, D. BAHR, B. SOMERDAY, Hydrogen effects on dislocation activity in austenitic stainless steel, Acta Mater. 54 (2006) 2677–2684, https://doi.org/10.1016/j.actamat.2006.02.007

[54] D. Tabor, The Hardness of Metals, Oxford University Press, 2000.

[55] G. Gottstein, Physical Foundations of Materials Science, Springer, Berlin Heidelberg, 2004, https://doi.org/10.1007/978-3-662-09291-0

[56] W.D. Nix, H. Gao, Indentation size effects in crystalline materials: a law for strain gradient plasticity, J. Mech. Phys. Solids 46 (1998) 411–425, https://doi.org/10.1016/S0022-5096(97)00086-0

[57] B.R. LAWN, A.G. EVANS, D.B. MARSHALL, Elastic/plastic indentation damage in ceramics: the median/radial crack system, J. Am. Ceram. Soc. 63 (1980) 574–581, https://doi.org/10.1111/J.1151-2916.1980.TB10768.X

[58] G.P.W.C. Oliver, An improved technique for determining hardness and elastic modulus using load and displacement sensing indentation experiments, J. Mater. Res 7 (1992) 1564–1583.

[59] K. Durst, B. Backes, O. Franke, M. Göken, Indentation size effect in metallic materials: modeling strength from pop-in to macroscopic hardness using geometrically necessary dislocations, Acta Mater. 54 (2006) 2547–2555, https://doi.org/10.1016/j.actamat.2006.01.036

[60] L. Chiari, K. Kojima, Y. Endo, H. Teshigahara, M. Butterling, M.O. Liedke, E. Hirschmann, A.G. Attallah, A. Wagner, M. Fujinami, Formation and time dynamics of hydrogen-induced vacancies in nickel, Acta Mater. 219 (2021) 117264, https://doi.org/10.1016/J.ACTAMAT.2021.117264

[61] R. Kirchheim, Reducing grain boundary, dislocation line and vacancy formation energies by solute segregationII. Experimental evidence and consequences, Acta Mater. 55 (2007) 5139–5148, https://doi.org/10.1016/j.actamat.2007.05.033

Article III

Distinct evidence of hydrogen-enhanced defects formation on pre-strained nickel alloy 625 during in-situ electrochemical nanoindentation test

CK Soundararajan, X Lu, D Wang, A Vinogradov

Submitted for peer review.

Distinct evidence of hydrogen-enhanced defects formation on pre-strained nickel alloy 625 during in-situ electrochemical nanoindentation test

Chandrahaasan K. Soundararajan [a,*], Xu Lu [a], Dong Wang [a], Alexey Vinogradov [a,b]

[a] *Department of Mechanical and Industrial Engineering, Norwegian University of Science and Technology, No-7491, Trondheim, Norway*

[b] *Magnesium Research Center (MRC), Kumamoto University, 2-39-1 Kurokami, Chuo-ku, Kumamoto 860-8555, Japan.*

Corresponding author: Chandrahaasan K. Soundararajan: *chandrahaasan.k.soundararajan@ntnu.no*

Abstract

In the present work, in-situ electrochemical nanoindentation was utilized to probe the hydrogen effect on nanomechanical properties of tensile pre-strained nickel alloy (0%, 5% and 20%). The study reveals hydrogen-induced hardening during cathodic polarization due to hydrogen incorporation and softening behavior during anodic polarization due to the irreversible microstructure modification induced in the presence of hydrogen solutes. Their respective contribution was quantified by fitting the elastoplastic part of load-displacement data. In addition, the differences in their plastic behaviors were investigated in detail by examining the dislocation structure underneath the indents. The study aims to shed light on hydrogen interaction with pre-existing defects.

Keywords: In-situ nanoindentation; hydrogen; pre-strain nickel alloy, hardening and softening, dislocations.

This paper is awaiting publication and is not included in NTNU Open

ISBN 978-82-326-7572-2 (printed ver.)
ISBN 978-82-326-7571-5 (electronic ver.)
ISSN 1503-8181 (printed ver.)
ISSN 2703-8084 (online ver.)

NTNU
Norwegian University of
Science and Technology